

Université de Montréal

Analyse des paramètres atmosphériques
des étoiles naines blanches dans le voisinage solaire

par

Noemi Giammichele

Département de physique

Faculté des arts et des sciences

Mémoire présenté à la Faculté des études supérieures
en vue de l'obtention du grade de
Maître ès sciences (M.Sc.)
en physique

Décembre, 2010

©Noemi Giammichele, 2010

Université de Montréal
Faculté des études supérieures

Ce mémoire intitulé:

Analyse des paramètres atmosphériques
des étoiles naines blanches dans le voisinage solaire

présenté par:

Noemi Giammichele

a été évalué par un jury composé des personnes suivantes:

Gilles Fontaine, président-rapporteur
Pierre Bergeron, directeur de recherche
René Doyon, membre du jury

Mémoire accepté le: _____

Sommaire

Ce mémoire présente une analyse homogène et rigoureuse de l'échantillon d'étoiles naines blanches situées à moins de 20 pc du Soleil. L'objectif principal de cette étude est d'obtenir un modèle statistiquement viable de l'échantillon le plus représentatif de la population des naines blanches. À partir de l'échantillon défini par Holberg et al. (2008), il a fallu dans un premier temps réunir le plus d'information possible sur toutes les candidates locales sous la forme de spectres visibles et de données photométriques. En utilisant les modèles d'atmosphère de naines blanches les plus récents de Tremblay & Bergeron (2009), ainsi que différentes techniques d'analyse, il a été permis d'obtenir, de façon homogène, les paramètres atmosphériques (T_{eff} et $\log g$) des naines blanches de cet échantillon. La technique spectroscopique, c.-à-d. la mesure de T_{eff} et $\log g$ par l'ajustement des raies spectrales, fut appliquée à toutes les étoiles de notre échantillon pour lesquelles un spectre visible présentant des raies assez fortes était disponible. Pour les étoiles avec des données photométriques, la distribution d'énergie combinée à la parallaxe trigonométrique, lorsque mesurée, permettent de déterminer les paramètres atmosphériques ainsi que la composition chimique de l'étoile. Un catalogue révisé des naines blanches dans le voisinage solaire est présenté qui inclut tous les paramètres atmosphériques nouvellement déterminés. L'analyse globale qui en découle est ensuite exposée, incluant une étude de la distribution de la composition chimique des naines blanches locales, de la distribution de masse et de la fonction luminosité.

Mots clés: étoiles : paramètres fondamentaux - naines blanches - voisinage solaire - analyse statistique - distribution de masse - fonction luminosité - techniques: photométrique et spectroscopique

Abstract

We present improved atmospheric parameters of nearby white dwarfs lying within 20 pc of the Sun. The aim of the current study is to obtain the best statistical model of the least-biased sample of the white dwarf population. A homogeneous analysis of the local population is performed combining detailed spectroscopic and photometric analyses based on improved model atmosphere calculations for various spectral types including DA, DB, DQ, and DZ stars. The spectroscopic technique is applied to all stars in our sample for which optical spectra are available. Photometric energy distributions, when available, are also combined to trigonometric parallax measurements to derive effective temperatures, stellar radii, as well as atmospheric compositions. A revised catalog of white dwarfs in the solar neighborhood is presented. We provide for the first time a comprehensive analysis of the mass distribution and the chemical distribution of white dwarf stars in a volume-limited sample.

Subject headings: stars : fundamental parameters - white dwarfs - solar neighborhood - Statistical analysis - techniques: photometric and spectroscopic

Table des matières

Sommaire	i
Abstract	ii
Table des matières	iii
Liste des figures	v
Liste des tableaux	viii
Remerciements	ix
1 Introduction	1
2 Atmospheric Parameters of Nearby White Dwarfs	6
2.1 Abstract	7
2.2 Introduction	7
2.3 Definition of the Local Sample	10
2.4 Observations	11
2.4.1 Spectroscopic Observations	11
2.4.2 Photometric Observations	14
2.4.3 Trigonometric Parallax Measurements	15
2.5 Atmospheric parameter determinations	16
2.5.1 Theoretical Framework	16
2.5.2 Photometric Technique	17

2.5.3 Photometric Analyses of DQ and DZ White Dwarfs	20
2.5.4 Spectroscopic Technique	21
2.5.5 Adopted Atmospheric Parameters	24
2.6 Results	25
2.6.1 Distances	25
2.6.2 Mass Distributions	25
2.6.3 White Dwarf Luminosity Function	31
2.7 Summary and Conclusion	33
2.8 References	35
2.9 Tables	39
2.10 Figures	56
3 Conclusion	112
Bibliographie	114

Table des figures

2.1 (a) Optical spectra of DA and DAZ white dwarfs	57
2.1 (b) - continued.	58
2.1 (c) - continued.	59
2.2 Optical spectra of cool DA white dwarfs	60
2.3 (a) Optical spectra of halpha from DA and DAZ white dwarfs	61
2.3 (b) - continued.	62
2.3 (c) - continued.	63
2.3 (d) - continued.	64
2.4 (a) Optical spectra of DC White dwarfs	65
2.4 (b) - continued.	66
2.4 (c) - continued.	67
2.5 (a) Optical spectra of DQ White dwarfs	68
2.5 (b) - continued.	69
2.6 Optical spectra of DZ White dwarfs	70
2.7 ($V - I$, $V - K$) two-color diagram	71
2.8 M_V vs. ($V - I$) color-magnitude diagram	72
2.9 (a) Fits to the energy distributions	73
2.9 (b) - continued.	74
2.9 (c) - continued.	75
2.9 (d) - continued.	76
2.9 (e) - continued.	77

2.9 (f) - continued.	78
2.9 (g) - continued.	79
2.9 (h) - continued.	80
2.9 (i) - continued.	81
2.9 (j) - continued.	82
2.9 (k) - continued.	83
2.9 (l) - continued.	84
2.9 (m) - continued.	85
2.9 (n) - continued.	86
2.9 (o) - continued.	87
2.9 (p) - continued.	88
2.9 (q) - continued.	89
2.10 (a) Fits to the energy distributions	90
2.10 (b) - continued.	91
2.10 (c) - continued.	92
2.10 (d) - continued.	93
2.10 (e) - continued.	94
2.10 (f) - continued.	95
2.11 (a) Fits to the energy distributions of DQ stars	96
2.11 (b) - continued.	97
2.11 (c) - continued.	98
2.12 (a) Fits to the energy distributions of DZ stars	99
2.12 (b) - continued.	100
2.13 (a) - Fits to the optical spectra of the DA stars	101
2.13 (b) - continued.	102
2.13 (c) - continued.	103
2.13 (d) - continued.	104
2.14 log g correction : fit through SDSS stars.	105
2.15 log g correction : application to the SDSS sample.	106

2.16 log g correction : spectroscopic vs. photometric masses.	107
2.17 Mass distribution vs. effective temperature.	108
2.18 Histogram of the ratio of helium- to hydrogen-rich WDs.	109
2.19 Mass distributions	110
2.20 Luminosity function.	111

Liste des tableaux

2.1	OBSERVATIONAL RESULTS	40
2.1	continued.	41
2.1	continued.	42
2.1	continued.	43
2.1	continued.	44
2.1	continued.	45
2.2	RESULTS FROM PHOTOMETRIC FITS	46
2.2	continued.	47
2.2	continued.	48
2.3	RESULTS FROM SPECTROSCOPIC FITS	49
2.3	continued.	50
2.4	ADOPTED ATMOSPHERIC PARAMETERS OF NEARBY CANDIDATES .	51
2.4	continued.	52
2.4	continued.	53
2.4	continued.	54
2.4	continued.	55

Remerciements

Je tiens en premier lieu à remercier mon directeur de recherche Pierre Bergeron pour m'avoir accueillie dans son groupe et m'avoir fourni un sujet de recherche dans un domaine passionnant. J'aimerais également le remercier pour le temps et les efforts qu'il a fournis pour mon apprentissage et la réalisation de ma maîtrise.

Je tiens par la suite à remercier "les gars" du groupe : Alexandros, Patrick et Pier-Emmanuel (en ordre alphabétique, bien sûr!), pour avoir répondu à toutes mes questions, pallier à tous mes problèmes dans ma recherche, pour l'aide constante à la programmation en fortran, et pour les nombreuses sorties au pub et au Bar Lounge. Je ne peux aller plus loin sans remercier ma co-chambreuse Marie-Michèle, pour sa joie de vivre et son soutien moral quotidien, et surtout pour qui Saskatchewan et Espagne est toujours une bonne blague.

Un remerciement particulier à Luc Turbide pour m'avoir sortie du pétrin de nombreuses fois lors des différentes rébellions de mon compte astro ou de mon ordinateur.

Un remerciement vraiment spécial aux "filles du bureau" : Amélie (oui, tu y as une place honorifique), Cassandra, Marie-Ève, Marilyn et Sandie. C'est un environnement de travail des plus agréables, dans lequel c'est un plaisir de travailler et de faire des pauses "salon de thé" aux heures les plus incongrues de la journée (selon les voisins).

Je ne pourrais conclure ces remerciements sans parler du support exceptionnel de ma famille et belle-famille qui me soutient au quotidien (et lors de mes nuits au télescope!), et m'entoure chaleureusement. Merci à Ben, Véro (et Marilou), Louis-Étienne, Mikhail et Nadim pour toutes ces soirées endiablées qui m'ont permis de bien décompresser. Antoine, merci de m'avoir appris que "seule une personne médiocre peut atteindre le summum de ses capacités", et que "brebis enragée est pire que loup", avec ça je ne peux que réussir dans la vie.

Chapitre 1

Introduction

Les naines blanches représentent le dernier stade évolutif de près de 97 % des étoiles de la séquence principale, incluant notre Soleil. En effet, une naine blanche résulte de l'effondrement gravitationnel du cœur d'une étoile géante rouge. Ce cœur restant, dégénéré, qui a épuisé son carburant nucléaire, se refroidit inexorablement pendant des milliards d'années. Leur faible brillance et le fait que celle-ci ne cesse de diminuer, rendent les naines blanches des cibles très difficilement détectables du point de vue observationnel. Le fait même de leur existence n'a été découvert qu'au milieu du XIX^e siècle, et il a fallu attendre le début du XX^e siècle pour pouvoir décrire théoriquement ces objets à l'aide, en grande partie, des nouveaux développements dans le domaine de la mécanique quantique.

Malgré cela, il est d'un intérêt majeur de comprendre dans ses moindres détails la population de naines blanches car ces étoiles forment une classe unique de la population stellaire globale, et sont de ce fait un marqueur important de l'évolution de la Galaxie. La distribution de masse, la densité spatiale et la composition chimique, entre autres, sont des indices importants permettant de mieux retracer et contraindre ces chemins évolutifs. La fonction de luminosité des naines blanches, qui est une mesure de la densité spatiale en fonction de la luminosité intrinsèque, est un outil des plus précieux pour estimer l'âge du disque Galactique. Mais afin de pouvoir extraire des informations pertinentes de ces diagnostics, l'échantillon d'étoiles utilisé se doit d'être le plus complet possible pour être statistiquement viable.

La population des naines blanches est composée majoritairement d'étoiles de faible lumi-

nosité qui sont difficiles à étudier dès que l'on s'éloigne un tant soit peu du Soleil. Il n'existe pas de grands relevés exclusifs aux naines blanches, à proprement parler. La détection de naines blanches est souvent réalisée par le biais de relevés limités par la magnitude ou par le mouvement propre. Les relevés caractérisés par les grands mouvements propres, tels que les relevés du NLTT (New Luyten Two-Tenths), du LSPM (Lépine-Shara Promper Motion) et du SuperCOSMOS-RECONS (Research Consortium on Nearby Stars), se basent sur le déplacement relatif de certaines étoiles par rapport aux étoiles distantes (et immobiles en apparence), à deux époques distinctes. En couplant ces mouvements propres à des indices de couleur, on peut ainsi distinguer les naines blanches d'autres populations stellaires. Malgré le fait que cette technique soit couramment utilisée dans un grand nombre de relevés, il reste que les inconvénients sont majeurs. Les relevés à grand mouvement propre sont grandement biaisés par la cinématique des étoiles. De plus, les régions densément peuplées, tel que le plan galactique, sont généralement évitées, dû aux limites de la méthode de détection.

Des contributions majeures sur la connaissance actuelle de la population des naines blanches ont été également réalisées à l'aide de relevés mesurant l'excès de rayonnement ultraviolet (UV), une technique majoritairement employée parmi les relevés photométriques permettant l'identification de candidates naines blanches chaudes. Les études basées sur les relevés à excès dans l'UV permettent de construire la partie chaude de la fonction luminosité, comme celles récemment déterminées à partir des relevés Palomar Green (PG; Liebert et al. 2005) et Kiso (Limoges & Bergeron 2010). L'identification de candidates naines blanches par l'excès d'UV comporte par contre des restrictions importantes, en ne ciblant uniquement que les objets les plus bleus, et par le fait même des objets chauds. Il est difficile de générer un échantillon complet à l'aide de cette méthode, et il ne nous est pas permis d'obtenir de l'information sur la partie froide de la fonction luminosité.

Les relevés basés sur le mouvement propre et la colorimétrie mentionnés précédemment ne s'entrecoupent pas, et sont par le fait même incomplets. La seule possibilité d'obtenir un échantillon statistiquement représentatif est d'utiliser un échantillon complet limité par le volume, centré autour du Soleil. Un tel échantillon permet d'obtenir un modèle statistiquement précis tant que le compromis entre la complétude et la taille de l'échantillon est bien

respecté. On veut principalement éviter de se retrouver avec un échantillon entièrement connu mais ayant un nombre trop limité d'étoiles. Avec un échantillon complet, il est ainsi possible d'extrapoler notre connaissance de la population locale à celle des naines blanches dans leur ensemble, tels que la densité de masse ou la densité spatiale des naines blanches dans le disque galactique, ou même dans le halo.

De nombreuses études ayant pour cible la complétude et la caractérisation de l'échantillon de naines blanches dans le voisinage solaire ont été réalisées. La première étude entièrement dédiée à la définition d'un relevé complet de naines blanches proches a été réalisé par Holberg et al. (2002). La limite de distance de 20 pc a été choisie pour correspondre au volume défini par le relevé de NSTARS, une banque de données regroupant l'information disponible sur tous les objets présents aux alentours du Soleil. En se basant sur l'étude de Holberg et al. (2002), le volume défini par la limite arbitraire de 20 pc semble raisonnable en ce qui a trait à la complétude. La détermination de candidates probables est entièrement basée sur les magnitudes photométriques tirées du *Villanova White Dwarf Catalog*. Deux critères de sélection ont été utilisés afin de déterminer les naines blanches confinées à l'intérieur d'un volume de 20 pc de rayon. La priorité a été donnée aux objets ayant une parallaxe trigonométrique $\pi \geq 0.^{\circ}05$, les plaçant ainsi directement à l'intérieur de la limite voulue. Pour les étoiles n'ayant pas de parallaxes disponibles, le deuxième critère de sélection employé utilise des estimés de distance photométrique basé sur le calcul de $V - M_V \leq 1.505$. Une attention particulière a été portée sur la détection d'anomalies notoires parmi les étoiles sélectionnées, qui ont été retirées de l'échantillon. Comme Holberg et al. (2002) le mentionne, la qualité des données ainsi retracées est loin d'être uniforme, et présente surtout de grandes inhomogénéités. Afin d'être plus soucieux de la qualité des données, un ordre hiérarchique a été adopté, en priorisant les indices de couleurs Johnson $B - V$, Strömgren $b - y$ et multichannel $g - r$, autant que possible. L'effet direct de cette sélection mène à de grandes inhomogénéités dans le calcul des magnitudes absolues et, par propagation, sur l'estimation des distances. L'analyse réalisée avec cet échantillon nouvellement déterminé était entièrement concentrée sur le calcul de la densité spatiale locale et sur l'estimation de la complétude de cet échantillon. En se basant sur l'hypothèse d'un échantillon à 13 pc connu dans son intégralité, Holberg et al. (2002) estime alors

que l'échantillon local est complet à 65%. Mis à part les différents types spectraux, aucun détails concernant les paramètres atmosphériques des naines blanches dans le voisinage solaire ne sont présentés.

La recherche de naines blanches dans l'échantillon local de 109 candidates tiré de Holberg et al. (2002) s'est poursuivie par le travail de Vennes & Kawka (2003), Kawka et al. (2004) et Kawka & Vennes (2006), en utilisant le catalogue NLTT révisé de Salim & Gould (2003), un relevé basé sur le mouvement propre des étoiles. En combinant des diagrammes couleur-couleur à des diagrammes de mouvement propre réduit, ainsi qu'en effectuant un suivi spectroscopique des candidates naines blanches, il a été possible de faire une mise à jour de l'échantillon local de Holberg et al. (2002), plusieurs étoiles ayant été rajoutées et d'autres retirées de l'échantillon. Mentionnons, en particulier, la contribution importante de Kawka & Vennes (2006) à cette recherche, en identifiant spectroscopiquement 8 naines blanches se situant à moins de 20 pc du Soleil. Farihi et al. (2005), Subasavage et al. (2007) et Subasavage et al. (2008) ont également contribué à l'augmentation de l'échantillon local connu avec les découvertes de quelques autres candidates.

Holberg et al. (2008) et Sion et al. (2009) ont par la suite repris l'étude des naines blanches dans le voisinage solaire de Holberg et al. (2002) en rassemblant les découvertes récentes mentionnées ci-dessus, pour former un nouvel échantillon de 132 étoiles. Ce faisant, les candidates locales ayant de nouveaux estimés de distance à plus de 20 pc ont été éliminées de l'échantillon. Les paramètres atmosphériques des naines blanches de l'échantillon local ont été compilés par Holberg et al. (2008) à partir de nombreuses sources différentes. À l'aide de ces données, la masse moyenne de l'échantillon ainsi qu'une nouvelle estimation de la densité spatiale ont pu être calculées en utilisant une variété d'estimations de distance, combinant parallaxes trigonométriques, analyses spectroscopiques et photométriques. De son côté, l'étude de Sion et al. (2009) est entièrement axée sur les propriétés cinématiques ainsi que la distribution des différents types spectraux des naines blanches à moins de 20 pc du Soleil.

Ce manque de cohérence entre les différents modèles d'atmosphère et les techniques d'analyse représente le talon d'Achille des études de l'échantillon local réalisées jusqu'à présent. Les analyses qui en ont découlé sont donc teintées d'incertitudes, et les propriétés de l'échantillon

local qui en ont émané sont peu fiables. La quête d'un échantillon complet de naines blanches dans le voisinage solaire est encore une préoccupation actuelle (voir les travaux de Limoges et al. 2010, entre autres), alors que jusqu'à aujourd'hui, toute analyse complète à partir d'un même ensemble de données fut laissée de côté. Il est donc tout à fait approprié de reconsidérer la population locale d'étoiles naines blanches en procédant à une analyse rigoureuse, réalisée de manière homogène, de chaque étoile de cet échantillon.

Le chapitre 3 présente, sous la forme d'une publication qui sera éventuellement soumise à l'*Astrophysical Journal*, l'intégralité de l'étude réalisée sur l'échantillon des naines blanches dans le voisinage solaire. On présente dans un premier temps la sélection de l'échantillon local ainsi que les données spectroscopiques et photométriques utilisées, suivi d'une description détaillée des modèles d'atmosphère et des techniques d'analyse employées dans notre étude. L'analyse globale réalisée à partir des paramètres atmosphériques nouvellement déterminés est ensuite exposée, incluant une étude de la distribution de la composition chimique, de la distribution de masse et de la fonction luminosité des naines blanches dans le voisinage solaire.

Chapitre 2

Know Your Neighborhood: A Detailed Model Atmosphere Analysis of Nearby White Dwarfs

N. Giannicchele¹, P. Bergeron¹, & P. Dufour¹

To be submitted to *The Astrophysical Journal*

December 2010

1. Département de Physique, Université de Montréal, C.P. 6128, Succ. Centre-Ville, Montréal, Québec H3C 3J7, Canada.

2.1 Abstract

We present improved atmospheric parameters of nearby white dwarfs lying within 20 pc of the Sun. The aim of the current study is to obtain the best statistical model of the least-biased sample of the white dwarf population. A homogeneous analysis of the local population is performed combining detailed spectroscopic and photometric analyses based on improved model atmosphere calculations for various spectral types including DA, DB, DQ, and DZ stars. The spectroscopic technique is applied to all stars in our sample for which optical spectra are available. Photometric energy distributions, when available, are also combined to trigonometric parallax measurements to derive effective temperatures, stellar radii, as well as atmospheric compositions. A revised catalog of white dwarfs in the solar neighborhood is presented. We provide for the first time a comprehensive analysis of the mass distribution and the chemical distribution of white dwarf stars in a volume-limited sample.

2.2 Introduction

It is of major interest to fully understand the white dwarf population as it is a significant part of the global stellar population and a major indicator of the evolutionary history of the Galaxy. Mass distribution, space density, and chemical composition are most valuable pieces of information to better constrain their evolutionary history. The luminosity function of the white dwarf population, defined as the number of white dwarfs as a function of their intrinsic luminosity, can be a precious tool to narrow down the age of the Galactic disk. But in order to take the greatest advantage of these indications, the white dwarf population sampled must be as close as possible to a statistical completion.

The white dwarf population is composed mainly of low-luminosity stars that are rather difficult to study as we get further away from the Sun. Candidates are mainly discovered from either proper-motion-limited or magnitude-limited surveys. Proper-motion surveys are characterized by the finding of high-proper motion stars through a comparison of identical fields observed at two different epochs. By further combining these proper motions with color indices, white dwarfs can be successfully distinguished from other objects. Despite its wide use

in the building of major surveys, important flaws remain. Proper-motion surveys naturally present a high kinematic bias. Moreover, high density regions, such as the galactic plane, are usually avoided.

Major contributions to the knowledge of the white dwarf population were made through ultraviolet excess surveys, a technique primarily used among photometric surveys to identify hot white dwarf candidates. Studies based on ultraviolet excess surveys lead to the building of the bright end of luminosity function, like those recently derived from the Palomar Green (PG; Liebert et al. 2005) and the Kiso surveys (Limoges & Bergeron 2010). However, the restriction to the detection of only bluer and thus hotter objects represents a major bias in the case of ultraviolet excess surveys. Therefore, building a complete sample is highly compromised and does not allow us to obtain essential information on the faint end of the luminosity function.

Proper-motion-limited and magnitude-limited surveys are not cross-correlated and are both incomplete. The one possibility to get a less biased sample is to use a complete volume-limited sample, centered around the Sun. Such a sample can provide an accurate statistical model as long as the right balance of high completeness and small number statistics is achieved. A precise picture of the local sample can reliably be extended to the rest of the Galaxy to get important details on the white dwarf population, such as the mass density and the space density of white dwarfs within the galactic disk.

Numerous studies were performed aiming to complete and to characterize the sample of nearby white dwarfs. The first study dedicated to building a complete census of the local sample of white dwarfs was performed by Holberg et al. (2002). The distance of 20 pc was chosen to correspond to the volume of the NSTARS database, a program aimed at compiling information on possibly all stellar sources near the Sun, and at better understanding the local stellar population. As Holberg et al. (2002) further discussed in their work, the volume then defined by the 20 pc limit was assumed to be reasonably complete. The determination of the possible candidates was entirely based on photometric magnitudes collected from the Villanova White Dwarf Catalog. Two main selection criteria were used to determine white dwarfs within 20 pc. First, the WD catalog was searched for objects with trigonometric parallaxes $\pi \geq 0.^{\circ}05$. For stars with no available parallaxes, the cut was made with photometrically de-

terminated distances based on $V - M_V \leq 1.505$. Careful attention was paid to remove manually obvious known anomalies. As Holberg et al. (2002) reported, data retrieved in this manner were far from uniform in quality and not homogeneous in any way. A priority scheme was adopted to cope with the different data sources, giving a higher priority to Johnson $B - V$, Strömgren $b - y$, and multichannel $g - r$ color indices, when possible. The direct effect of this selection led to major inhomogeneities in the calculations of absolute visual magnitudes and resulting distances. The analysis made afterwards based on this local sample was uniquely drawn towards the calculation of the local space density and the estimation of the completeness of the sample. Based on the assumption that the 13 pc sample is entirely known, Holberg et al. (2002) estimated the 20 pc sample to be 65% complete. Few details showing the atmospheric properties of the white dwarfs in the solar neighborhood were presented at that time.

The quest for completeness of the local sample of white dwarfs based on the 109 candidates determined by Holberg et al. (2002) was pursued by the contributions of Vennes & Kawka (2003), Kawka et al. (2004), and Kawka & Vennes (2006) who surveyed the revised NLTT catalog of Salim & Gould (2003). By using color-color and reduced proper motion diagrams, as well as a spectroscopic follow-up of white dwarf candidates, several stars were added to the original local sample, while some others were removed. In particular, Kawka & Vennes (2006) extended the search for possible candidates by spectroscopically identifying 8 new white dwarfs lying within 20 pc. Other contributions from Farihi et al. (2005), Subasavage et al. (2007), and Subasavage et al. (2008) are also worth mentioning in the finding of new local candidates.

Holberg et al. (2008) and Sion et al. (2009) reanalyzed the white dwarfs in the solar neighborhood by updating the local sample of Holberg et al. (2002) with the recent discoveries mentioned above, to form a sample composed of 132 stars. Holberg et al. (2008) gathered atmospheric parameters of the local sample candidates, collected from numerous sources, to calculate the mean mass of the sample, and used a variety of spectroscopic, photometric, and trigonometric distances to better estimate the local space density. Sion et al. (2009) strictly focused on the kinematical properties and the distribution of spectroscopic subtypes of the

white dwarf population within 20 pc.

The lack of consistency from the different model atmospheres and methods used makes previous analyses of the ensemble properties of the local white dwarf sample quite uncertain, and may lead to erroneous estimates. Obviously, the quest for the local sample completeness is still a central preoccupation, while proper analysis of such a sample has been left aside, as up to now, there is no detailed study regrouping all available data. Given these restrictions, it is appropriate to revisit the nearby white dwarf population by performing a rigorous analysis, in an homogeneous fashion, of every star in the sample.

In this paper, we present improved atmospheric parameters of all possible nearby white dwarfs lying within 20 pc of the Sun. A homogeneous and complete analysis of the local population is performed combining detailed spectroscopic and photometric analyses based on improved model atmosphere calculations for various spectral types including DA, DC, DQ, and DZ stars. Our photometric and spectroscopic observations are presented in Section 2.4, while the theoretical framework and fitting techniques are exposed in Section 2.5. The global properties of our sample, including the mass distribution and luminosity function are examined in Section 2.6. Our conclusions follow in Section 2.7.

2.3 Definition of the Local Sample

Our sample is composed of spectroscopically identified white dwarfs that lie in the solar neighborhood, within the approximate 20 pc defined limit. It is mostly drawn from the complete list presented in Sion et al. (2009), an updated version of the local population defined by Holberg et al. (2002, 2008). As mentioned earlier, significant additions to this initial sample have been made by Kawka et al. (2004), Kawka & Vennes (2006), and Subasavage et al. (2007, 2008), with some contributions from other studies (see references in Sion et al. 2009). We increased the sample size by taking into account all possible white dwarfs that could lie within the error limit inside the 20 pc region, which means including all objects presented in Table 5 of Holberg et al. (2008). We include here the peculiar DQ star LHS 2229 (1008+290) since a new trigonometric parallax made available to us by H. C. Harris. (2010, private communication) places the star inside the 20 pc region. Also, we include the DC star LHS 1247

(0123–262) since its distance, estimated from the photometric observations of Bergeron, Ruiz, & Leggett (1997, hereafter BRL97), places this candidate inside our region of interest, within the uncertainties. Finally, an initial sample of 167 white dwarf stars has been retained for this analysis. The complete list of objects is presented in Table 2.1 where we give for each star the WD number from the Villanova White Dwarf Catalog as well as an alternate name; whenever possible we used the LHS or the Giclas names unless the object is better known under another name in the literature. The additional entries for each object are described in the next section.

2.4 Observations

2.4.1 Spectroscopic Observations

One of the original goals of this project was to characterize the best we could the white dwarf population in the solar neighborhood, which implies at first to provide a spectroscopic snapshot of this population in the form of an atlas similar to that published by Wesemael et al. (1993). Spectroscopic observations at high signal-to-noise ratio were thus secured for 136 objects in our sample. Most of the blue spectra ($\lambda \sim 3700 - 5200 \text{ \AA}$) for the DA white dwarfs were already available to us from of our numerous studies of these stars (see, e.g., Liebert et al. 2005), while several spectra covering the region near H α , required to constrain the atmospheric composition of the coolest degenerates, were taken from the studies of BRL97 and Bergeron, Leggett, & Ruiz (2001, hereafter BLR01).

New optical spectra for 23 objects in our sample were acquired for the specific purpose of this project during several observing runs at the Steward Observatory 2.3 m telescope equipped with the Boller & Chivens spectrograph and a Loral CCD detector. The 4."5 slit together with the 600 l mm^{-1} grating in first order provided a spectral coverage from about 3200 to 5300 \AA at an intermediate resolution of $\sim 6 \text{ \AA FWHM}$. Spectra were also obtained with the Kitt Peak National Observatory 2.1 m and 4 m telescopes equipped with the RC and Goldcam spectrographs, respectively. Both used a 2."0 slit with a resolution of $\sim 6 \text{ \AA FWHM}$, but different gratings of 316 l mm^{-1} and 500 l mm^{-1} , respectively. Further details

on the observing and reduction procedure can be found in Saffer et al. (1994).

The spectral types of each white dwarf in our nearby sample are reported in Table 2.1. Otherwise noted in the last column, all spectral types have been confirmed from our own spectroscopic observations. In summary, this sample breaks down into the following spectral types: 111 DA, 26 DC, 19 DQ, 10 DZ and 1 DBQA. Strangely enough, there is not a single warm ($T_{\text{eff}} > 13,000$ K) DB star in this nearby sample. According to our ongoing spectroscopic analysis of relatively bright DB stars (Bergeron et al. 2010), the closest DB stars lies at ~ 30 pc.

Figure 2.1(a-c) presents the DA and DAZ spectra in our sample in order of decreasing effective temperatures (determined below using the spectroscopic technique, see Section 2.5.4). The DAZ stars are easily recognized by the presence of the Ca II H and K lines, the most notable DAZ star in this sample being GD 362 (1729+371) whose spectrum also shows spectral lines from Ca I, Mg I, and Fe I (Gianninas et al. 2004). The spectrum of LHS 1660 (0419–487) is also contaminated by the presence of an M dwarf companion. GR 431 (0939+071), also known as PG 0939+072, is a problematic object. Classified DC7 in the PG catalog, it was not included in the spectroscopic analysis of DA white dwarfs in the PG survey of Liebert et al. (2005), despite the fact that it had been reclassified as DA2 in Holberg et al. (2002). However, it appeared again as DC7 in Table 4 of Holberg et al. (2008), a list of *possible* white dwarfs within 20 pc. Our spectrum, presented in Figure 2.1(c), shows that GR 431 is not a white dwarf. Our spectroscopic fit for this star yields $T_{\text{eff}} \sim 6800$ K and $\log g = 6.9$, too low for a white dwarf; this star is therefore excluded from our analysis.

The blue spectra for the DA and DAZ stars too cool to be analyzed using line profile fitting techniques are displayed in Figure 2.2. In some cases, these objects are completely featureless in the spectral region shown here, which implies that only H α can be detected spectroscopically.

The DA stars in our sample for which spectra at H α are also available are presented in Figure 2.3(a-d) as a function of decreasing equivalent widths. The Zeeman triplet in the magnetic white dwarf LHS 1734 (0503–174) is clearly visible. The presence of H α in the coolest white dwarfs is crucial to better constrain the atmospheric parameters using the photometric

method described in Section 2.5.2. The coolest DA stars in which H α can be detected in our sample have photometric temperatures around $T_{\text{eff}} \sim 5000$ K.

Our set of DC white dwarfs, with featureless spectra, as well as the spectrum for LDS 678A (1917–077), the only DBQA star, are displayed in Figure 2.4(a) in order of right ascension. For clarity the spectra have been normalized to a continuum set to unity. Subsets of DC stars with only blue and red spectral coverage are also displayed in Figure 2.4(b-c). Spectroscopic data of some DQ stars in our sample are displayed in Figure 2.5(a). Because of the spectral classification scheme devised by McCook & Sion (1999), DQ white dwarfs may have carbon features detectable only in the ultraviolet, hence some spectra shown here appear featureless in the optical; note the presence of the CH band in the spectrum of G99-37 (0548–001), one of the only two such stars known. Additional DQ stars are shown in Figure 2.5(b). At the top of the figure is shown a normal DQ star with very strong C₂ Swan bands. Note how these molecular bands in the other objects shown in this figure appear shifted and more symmetrical with respect to this normal DQ star, with the extreme case of LHS 2229 (1008+290) displayed at the bottom. This phenomenon has recently been explained by Kowalski (2010) as a result of pressure shifts of the carbon bands that occurs in cooler, helium-dominated atmospheres. The presence of a very strong magnetic field has also been reported in the bottom two objects (see, e.g., Schmidt et al. 1999). These stars are now being classified as DQpec.

Finally, our DZ spectra, showing the presence of metal lines, mainly the Ca II H & K doublet, are displayed in Figure 2.6. Both L745-46A (0738–172) and Ross 640 (1626+368) are actually DZA stars with very shallow H α absorption lines (shown in Fig. 2.3), resulting from the presence of a trace of hydrogen in a helium-dominated atmosphere.

It is interesting to note that the local population of white dwarfs includes some of the strangest stars we know, including those mentioned above which are unique objects, but also GW+70 8247 (1900+705), a heavily magnetic white dwarf; G47-18 (0856+331), a unique DQ star that shows both C₂ Swan bands and C I atomic lines; BPM 27606 (2154–512), one of the DQ stars with the strongest C₂ Swan bands; G240-72 (1748+708) whose spectrum is characterized by a deep yellow sag in the 4400–6300 Å region (see Fig. 2.5(a) and also Wesemael et al. 1993); LP 701-29 (2251–070), a heavily blanketed DZ star, the only known

case where Ca I $\lambda 4226$ appears stronger than the Ca II doublet. Definitely, we live in strange neighborhood.

2.4.2 Photometric Observations

Optical $BVRI$ and infrared JHK photometric data were retrieved for 82 cool white dwarfs in our sample, taken mainly from the detailed studies of BRL97 and BLR01. Complete details of the observing procedure and data reduction are provided in these references. For 26 additional cool degenerates remaining with no available data, optical V magnitudes were obtained from different sources, mainly from the online version of the Villanova White Dwarf Catalog, while infrared JHK_S photometry was extracted from the online version of the Two Micron All Sky Survey (2MASS) survey. The optical and infrared photometric data are reported in Table 2.1; references for the adopted photometry are provided in the last column. Typical photometric uncertainties are 3% at V , R , and I , and 5% elsewhere (BLR01). Uncertainties for the V magnitudes retrieved from the White Dwarf Catalog vary widely and we simply assume 5% for simplicity.

The $(V - I, V - K)$ two-color diagram is displayed in Figure 2.7 for 71 white dwarfs in our sample. DA and non-DA stars are represented by filled and open circles, respectively. Also shown are the predictions from pure hydrogen and pure helium cooling sequences at $\log g = 8.0$ using the photometric calibration of Holberg & Bergeron (2006). DA and non-DA stars form two distinct narrow sequences in this diagram, which follow closely the behavior of the model sequences. Worth mentioning here is a complete absence of non-DA stars in a particular range of $V - K$ colors between ~ 1.2 and 1.7 , which corresponds to the so-called non-DA gap first discussed by BRL97. There are also several outliers in this diagram, identified in the figure, all of the non-DA type: BPM 27606 (2154–512) is a DQ star with very strong C₂ Swan bands (see Figure 2.5) that affect the V magnitude; LHS 1126 (0038–226) shows a strong infrared flux deficiency which has been interpreted by Bergeron et al. (1994) in terms of the H₂-He collision-induced absorptions in a mixed H/He atmosphere; ER 8 (1310–472) is the coolest and oldest white dwarf identified in the analysis of BRL97, and it has a pure hydrogen atmospheric composition despite its non-DA nature; G195-19 (0912+536) is a ~ 100

MG magnetic white dwarf with some unidentified spectroscopic features (Schmidt & Smith 1994) that affect the I magnitude.

Data sets appropriate for a photometric or spectroscopic analysis could not be found for 3 remaining stars (0208–510, 0415–594, and 1132–325), the first two of which are Sirius-like systems. These objects had to be left aside in the present analysis.

2.4.3 Trigonometric Parallax Measurements

BRL97 found that even though the model energy distributions are somewhat sensitive to surface gravity, it is practically impossible to determine $\log g$ from the observed photometry alone. Only for stars with available trigonometric parallax measurements is it possible to determine the stellar radius, and thus the mass through the mass-radius relation. In our sample, 109 stars have trigonometric parallax measurements taken from the Yale parallax catalog (van Altena et al. 1994, hereafter YPC) and the Hipparcos parallax catalog (Perryman & ESA 1997), with the exception of LHS 1044 (0011–134; Bergeron et al. 1992b), vB 3 (0743–340; Ruiz et al. 1989), — LHS 1243, SCR 0753–2524, SCR 0821–6703, LEHPM 2–220, L104–2, L40–116 and SCR 2012–5956 (0121–429, 0751–252, 0821–669, 1009–184, 1223–659, 1315–781 and 2008–600; Subasavage et al. 2009)— , GD 362 (1729+371; Kilic et al. 2008), LEHPM 4466 (2211-392; Ducourant et al. 2007), and LHS 2229 (1008+290; H. C. Harris, private communication); these values and corresponding uncertainties are reported in Table 2.1.

The M_V versus $(V - I)$ color-magnitude diagram obtained using these trigonometric parallaxes is displayed in Figure 2.8 for 74 stars in our sample, with available V and I colors. Again, white dwarfs are distinguished in terms of their DA or non-DA spectral types, and the predictions from pure hydrogen and pure helium cooling sequences at $\log g = 8.0$ are superimposed on the observed data.

As mentioned by BLR01, DA and non-DA stars form well-defined narrow sequences in this diagram, although not as narrow as those observed in the previous figure, most likely because the trigonometric parallax measurements come from inhomogeneous parallax samples. In general, non-DA stars appear less luminous than DA stars, a result that can be explained

if non-DA stars are more massive, and thus possess smaller radii, than their DA counterpart. Also, all overluminous white dwarfs are of the DA spectral type. As discussed in BRL97, most, if not all, of these objects are unresolved binaries — e.g., L870-2 (0135–052) — and their luminosity is the contribution of two white dwarfs with probably normal masses.

2.5 Atmospheric parameter determinations

2.5.1 Theoretical Framework

Our synthetic spectra are built from the new LTE model atmosphere code described at length in Tremblay & Bergeron (2009) and references therein, which uses improved calculations for the Stark broadening of the hydrogen line profiles. The theoretical spectra are calculated within the occupation formalism of Hummer & Mihalas (1988), with the inclusion of nonideal perturbations from protons and electrons directly inside the unified theory of Stark broadening of Vidal et al. (1970). Models take into account convective energy transport and hydrogen molecular opacity up to an effective temperature at which non-local thermodynamic equilibrium (NLTE) effects are still negligible and the atmospheres are completely radiative ($T_{\text{eff}} = 40,000$ K). Above this temperature, the TLUSTY and SYNSPEC packages are used to deal with NLTE effects present in hotter stars. The resulting homogeneous model grid thus consistently includes NLTE effects, as well as convective energy transport following the revised $\text{ML2}/\alpha = 0.8$ prescription of the mixing-length theory (see Bergeron et al. 1995 and Tremblay & Bergeron 2009 for details). For helium-dominated stars, model atmospheres and synthetic spectra include the improved Stark profiles of neutral helium of Beauchamp et al. (1997). Additional models for DQ and DZ stars are described below.

Our model grid covers a range of effective temperature between $T_{\text{eff}} = 1500$ K and 45,000 K by steps of 500 K for $T_{\text{eff}} < 15,000$ K, 1000 K up to $T_{\text{eff}} = 18,000$ K, 2000 K up to $T_{\text{eff}} = 30,000$ K, and by steps of 5000 K above. The $\log g$ ranges from 6.5 to 9.5 by steps of 0.5 dex, with additional models at $\log g = 7.75$ and 8.25. Additional models, in particular for cool stars, have been calculated with mixed hydrogen and helium compositions of $\log (\text{H}/\text{He}) = -1.0$ to 3.0 (in steps of 0.5).

2.5.2 Photometric Technique

Atmospheric parameters, T_{eff} and $\log g$, and chemical compositions of cool white dwarfs can be measured accurately using the photometric technique developed by BRL97. We first convert optical $BVRI$ and infrared JHK (or JHK_S from 2MASS) photometric measurements into observed fluxes and compare the resulting energy distributions with those predicted from our model atmosphere calculations. To accomplish this task, we first transform every magnitude m into an average flux f_λ^m using the equation

$$m = -2.5 \log f_\lambda^m + c_m , \quad (2.1)$$

where

$$f_\lambda^m = \frac{\int_0^\infty f_\lambda S_m(\lambda) \lambda d\lambda}{\int_0^\infty S_m(\lambda) \lambda d\lambda} , \quad (2.2)$$

and where $S_m(\lambda)$ is the transmission function of the corresponding bandpass, f_λ is the monochromatic flux from the star received at Earth, and c_m is a constant to be determined. The transmission functions are taken from Landolt (1992a,b) for the $BVRI$ filters on the Johnson-Kron-Cousins CTIO photometric system, and from Bessell & Brett (1988) for the JHK filters on the Johnson-Glass system. Infrared magnitudes on the CIT system taken from BRL97 and BLR01 first need to be transformed on the Johnson-Glass system using the equations given by Leggett (1992). For JHK_S , we used the transmission functions from the 2MASS set defined by Cohen et al. (2003).

The constants c_m for each passband are determined using the improved calibration fluxes from Holberg & Bergeron (2006), defined with the Hubble Space Telescope (HST) absolute flux scale of Vega. The calculations yield $c_B = -20.45645$, $c_V = -21.06067$, $c_R = -21.64393$, $c_I = -22.38477$, $c_J = -23.75551$, $c_H = -24.84898$, and $c_K = -25.99941$. For the 2MASS set, we find instead $c_J = -23.76771$, $c_H = -24.86404$, and $c_{K_S} = -25.92455$.

For each star in Table 2.1, a minimum set of four average fluxes f_λ^m is obtained that can be compared with model fluxes. Since the observed fluxes correspond to averages over given bandpasses, the monochromatic fluxes from the model atmospheres need to be converted

into *average fluxes* as well, H_λ^m , by substituting f_λ in equation 2.2 for the monochromatic Eddington flux H_λ . We can then relate the average observed fluxes f_λ^m and the average model fluxes H_λ^m — which depend on T_{eff} , $\log g$, and He/H — by the equation

$$f_\lambda^m = 4\pi(R/D)^2 H_\lambda^m \quad (2.3)$$

where R/D defines the ratio of the radius of the star to its distance from Earth. We then minimize the χ^2 value defined in terms of the difference between observed and model fluxes over all bandpasses, properly weighted by the photometric uncertainties. Our minimization procedure relies on the nonlinear least-squares method of Levenberg-Marquardt (Press et al. 1986), which is based on a steepest decent method. Only T_{eff} and the solid angle $\pi(R/D)^2$ are considered free parameters, and the uncertainties of both parameters are obtained directly from the covariance matrix of the fit. For white dwarfs with no parallax measurement, we simply assume a value of $\log g = 8.0$.

Our results for the analysis of optical and JHK photometric data sets are presented in Figure 2.9(a-q), and in Figure 2.10(a-f) for the 2MASS JHK_S data sets. Observed fluxes in the left panels are represented by error bars, while model fluxes are shown as open or filled circles depending on the atmospheric composition. The atmospheric parameters of each solution are indicated in the panel. On the right panels are shown the spectroscopic observations near $\text{H}\alpha$ compared to the model atmosphere predictions *assuming the pure hydrogen solution*; these only serve as an internal check of our photometric solutions and are not used in the fitting procedure. For instance, cases where an $\text{H}\alpha$ absorption feature is predicted but is *not* observed clearly suggest that the pure helium solution is more appropriate. In cases where the star is too cool to show $\text{H}\alpha$ ($T_{\text{eff}} \lesssim 5000$ K), however, one has to rely on the predicted energy distributions to decide which atmospheric composition best fit the photometric data. Based on our inspection of these fits, we adopt the solutions shown in red in the left panels.

In general, the fits to the energy distributions, and the internal consistency with the absence or presence of $\text{H}\alpha$, are excellent. Several objects in Figure 2.9 are worth discussing, however. LHS 1008 (0000–345) belongs to this strange class of objects reported by BRL97 whose energy distributions are better fit with pure hydrogen models, yet their spectra are fea-

tureless near the $\text{H}\alpha$ region. There are three weakly magnetic white dwarfs shown here — LHS 1044 (0011–134), LHS 1734 (0503–174), and G99-47 (0553+053), all three of which exhibit the Zeeman triplet; the predicted $\text{H}\alpha$ profiles shown here do not include the magnetic field. For LHS 1126 (0038–226), a mixed abundance of $\text{He}/\text{H} \sim 100$ was required to reproduce the infrared flux deficiency, as discussed above. Some of the strongest DZ stars, vMa 2 (0046+051) for instance, show a small disagreement for the B bandpass where the Ca II H & K doublet depresses the observed flux significantly. Such DZ stars will be analyzed in greater detail in the next section. Some DA stars — L587-77A (0326–273) and L532-81 (0839–327) — show a strong discrepancy between the observed and predicted profiles; since they are also low surface gravity objects, these are most likely unresolved double degenerate systems composed of two DA stars. Note that the absorption feature seen in G47-18 (0856+331) is a neutral carbon line and not $\text{H}\alpha$. Also, the predicted $\text{H}\alpha$ profiles for L745-46A (0738–172) and Ross 640 (1626+368) both assume a pure hydrogen composition while these stars contain only a trace of hydrogen of the order of $\text{H}/\text{He} \sim 10^{-4} – 10^{-3}$. Our fit to LHS 1660 (0419–487) is obviously contaminated by the presence of the M dwarf companion (see spectrum in Fig. 2.1) and our photometric solution is thus unreliable. Similarly, the photometry for L481-60 (1544–377) is contaminated by the presence of a bright companion and cannot be trusted. These last two objects have good spectroscopic fits, however (see below). Finally, GD 184 (1529+141; also known as NLTT 40489), shown in Figure 2.10(e), was discovered by Kawka & Vennes (2006) who assigned a temperature of $T_{\text{eff}} = 5250$ K based on fits to the weak hydrogen lines. However, the energy distribution suggests a much higher temperature of $T_{\text{eff}} \sim 9100$ K, in sharp disagreement with the predicted $\text{H}\alpha$ absorption feature. This object is most certainly an unresolved degenerate binary composed of a DA and a DC white dwarf.

Table 2.2 summarizes the atmospheric parameters and adopted chemical compositions obtained from our photometric analysis. Also given for each star are the stellar mass and the photometric distance, the latter derived from the value of the fitted solid angle $\pi(R/D)^2$; white dwarfs with no parallax measurements, and for which a value of $\log g = 8.0$ was assumed, have corresponding $\log g$ and mass uncertainties of 0.00 in this table. The stellar mass and radius of each star are obtained from evolutionary models similar to those described in Fontaine et

al. (2001) but with C/O cores, $q(\text{He}) \equiv \log M_{\text{He}}/M_{\star} = 10^{-2}$ and $q(\text{H}) = 10^{-4}$, which are representative of hydrogen-atmosphere white dwarfs, and $q(\text{He}) = 10^{-2}$ and $q(\text{H}) = 10^{-10}$, which are representative of helium-atmosphere white dwarfs².

2.5.3 Photometric Analyses of DQ and DZ White Dwarfs

Even though the photometric fits to the DQ and DZ white dwarfs discussed in the previous section appear reasonable, they still require an improved treatment when analyzed with the photometric method since strong carbon or other metallic features may affect the flux in some photometric bands. Moreover, the presence of heavier elements in helium-rich models provides enough free electrons to affect the atmospheric structure significantly, and thus the predicted energy distributions. To circumvent these problems we rely on the LTE model atmosphere calculations developed by Dufour et al. (2005) and Dufour et al. (2007) for the study of DQ and DZ stars, respectively, based on a modified version of the code described at length in Bergeron et al. (1995). The main addition to the models is the inclusion of metals and molecules in the equation of state and opacity calculations.

The approach for analyzing the DQ stars in our sample is fully described in Dufour et al. (2007). The method used to fit the energy distributions is similar to the photometric technique described above with the exception that a third fitting parameter, the carbon abundance, is also taken into account. Spectroscopic observations are used to determine the carbon abundance by fitting the C₂ Swan bands at the values of T_{eff} and $\log g$ obtained from a first fit to the energy distribution with an arbitrary carbon abundance. This improved carbon abundance is then used to obtain new estimates of the atmospheric parameters from the energy distribution, and so forth. This iterative procedure is repeated until T_{eff} , $\log g$, and the carbon abundance converge to a consistent photometric and spectroscopic solution. We have to emphasize that, in the particular case of peculiar DQ stars (DQpec) whose absorption features have been successfully interpreted as pressure-shifted C₂ Swan bands by Kowalski (2010), we rely on the previous photometric analysis performed under the assumption of a pure helium composition since our models do not include these improved molecular opacity calculations

2. See <http://www.astro.umontreal.ca/~bergeron/CoolingModels/>

yet.

The fitting procedure for DZ stars is similar in every aspect to the method previously described for the DQ analysis, as outlined in Dufour et al. (2005). The only difference is that spectroscopic observations of the Ca II H & K doublet are used to determine the metal abundance. For the abundance of other heavier elements, not visible spectroscopically, we assume solar ratios for relative abundances with respect to calcium. Also, since invisible traces of hydrogen may affect the predicted metallic absorption features (see Dufour et al. 2005 for details), we study the influence of this additional parameter by using model grids calculated with hydrogen abundances of $\log (\text{H}/\text{He}) = -3, -4, \text{ and } -5, \text{ and } -30$.

We present the results for the DQ and DZ stars in our sample in Figures 2.11(a-c) and 2.12(a-b), respectively. As before, observed fluxes are represented by error bars, while model fluxes are shown as filled circles corresponding to the pure helium atmospheric composition. The atmospheric parameters of each fit are indicated in each panel. The spectroscopic observations used in the fitting procedure to determine the metal abundances are shown in the right panels.

2.5.4 Spectroscopic Technique

The atmospheric parameters of DA stars with well-defined Balmer lines ($T_{\text{eff}} \gtrsim 6000 \text{ K}$) can be determined precisely from the optical spectra using the so-called spectroscopic technique developed by Bergeron et al. (1992a). A similar approach can of course be used for (hot) DB stars, although none have been identified in our nearby sample. The technique relies on detailed fits to the observed normalized Balmer line profiles with model spectra, convolved with the appropriate Gaussian instrumental profile. We use the same Levenberg-Marquardt nonlinear least-squares fitting method described above. In this case the χ^2 minimization procedure uses all Balmer lines simultaneously to determine the atmospheric parameters T_{eff} and $\log g$. In the case of contamination by an unresolved main-sequence companion, usually an M dwarf, we simply exclude from the fit the absorption lines that are contaminated (usually H β but occasionally H γ as well). Figure 2.13(a-d) presents the entire set of our spectroscopic fits, while the spectroscopic values of T_{eff} and $\log g$ are reported in Table 2.3.

The spectroscopic fits are in general excellent. There is an obvious contamination at H β in LHS 1660 (0419–487) from the M dwarf companion, and this line has been omitted from our fit. Also, the blue wings of H ϵ in G74-7 (0208+396), G180-63 (1633+433), and GD 362 (1729+371), are affected by the blue component of the Ca II H & K doublet (the red component overlaps with H ϵ), but because of our efficient normalization procedure, this contamination does not affect the atmospheric parameter determination significantly, with the exception of GD 362 with its very strong calcium lines. Since GD 362 has actually a mixed hydrogen and helium atmosphere, which affects the $\log g$ value inferred from pure hydrogen models, we simply use below the atmospheric parameters determined by Tremblay et al. (2010) using more appropriate models for this star. We finally note that the discrepancy observed in the line cores of LP 907-37 (1350–090) is due to the presence of a relatively weak (~ 100 kG) magnetic field (Schmidt & Smith 1994).

Even though the spectroscopic technique is arguably the most accurate method for measuring the atmospheric parameters of DA stars, it has an important drawback at low effective temperatures ($T_{\text{eff}} \lesssim 13,000$ K) where spectroscopic values of $\log g$ are significantly larger than those of hotter DA stars. This so-called high- $\log g$ problem has been discussed at length in Tremblay et al. (2010) and references therein. A first solution proposed for this problem was a mild and systematic helium contamination from convective mixing that would confusingly mimic the high $\log g$ values inferred from the spectroscopic technique (Bergeron et al. 1990). However, this suggestion was refuted by Tremblay et al. (2010), and as up to now, there is no alternative explanation that has been proven satisfactory. Since spectroscopic distances³ are sensitive to $\log g$ values, it is important to obtain reliable measurements of surface gravities.

If we recall that the local population is mainly composed of cool stars, the high- $\log g$ problem becomes increasingly problematic for the ongoing analysis. Out of the 167 white dwarfs in our nearby sample, 51 DA stars with optical spectra available are in the 5000 – 13,000 K temperature range. Unfortunately, photometry is available for only 22 of these objects, and we must thus rely on spectroscopic estimates of $\log g$ to measure distances. Since spectroscopic temperatures are not believed to be affected significantly by the particular

3. Spectroscopic distances are obtained by combining V magnitudes with absolute visual magnitudes calculated from model atmospheres at the spectroscopic values of T_{eff} and $\log g$.

choice of $\log g$, we use here a procedure aimed at correcting independently all spectroscopic $\log g$ values for all DA stars below 13,000 K.

To do so, we apply an empirical correction based on a statistically large and representative sample of DA white dwarfs. The best characterization of the high- $\log g$ problem can be found in the recent analysis of Tremblay et al. (2011) for the DA stars identified in the Data Release 4 of the Sloan Digital Sky Survey. In particular, the mass distribution as a function of effective temperature shown in their Figure 18 (reproduced here in the top panel of Figure 2.15) shows a significant increase in the $\log g$ distribution at low temperatures, with a distinctive triangular shape (see Section 4.2 of Tremblay et al. 2011 for a more elaborate discussion). We next fit in the T_{eff} - $\log g$ diagram a third order polynomial through the SDSS data points at low temperatures using average bins of 500 K in temperature. The result of this fit is displayed in Figure 2.14. A low order polynomial was preferred in order to ensure a certain smoothness in our correction procedure, and to get rid of any possible large variations due to the inhomogeneous distribution of stars between consecutive bins. Careful attention was also given to remove all stars outside one standard deviation from the mean $\log g$ value in each bin. By doing so, we want to make sure that we eliminate any possible bias that could result from any excess of high- or low-mass stars in a given bin. Also shown in Figure 2.14 is the evolutionary track for a mass of $0.61 M_{\odot}$, taken from Fontaine et al. (2001), which corresponds to the mean mass of DA stars determined by Tremblay et al. (2011, see their Table 4). Finally, the correction we apply to our spectroscopic $\log g$ values below 13,000 K is simply given by the difference between the black and red curves in Figure 2.14 at a given temperature.

The spectroscopic $\log g$ values for the DA stars in the SDSS corrected in this fashion are displayed as a function of temperature in the bottom panel of Figure 2.15. The continuity of the $\log g$ distribution observed here through the entire temperature range suggests that our correction procedure appears reasonably sound. The corrected $\log g$ values for the cool DA stars in our local sample are reported in Table 2.3. Also given for each star are the corresponding stellar mass, absolute visual magnitude, and spectroscopic distance obtained from the distance modulus ($V - M_V = 5 \log D - 5$), where the V magnitudes are taken from

Table 2.1 and the M_V values are calculated from model atmospheres at the spectroscopic values of T_{eff} and (corrected) $\log g$. All these quantities rely on the same evolutionary models as before.

An external check of our correction procedure can be obtained by comparing the inferred masses for DA stars for which both photometric and spectroscopic estimates are available. This comparison is displayed in Figure 2.16 for spectroscopic masses derived for uncorrected as well as corrected $\log g$ values. We see that, overall, the photometric and corrected spectroscopic masses are in much better agreement, although in some cases the agreement is worse. There are also three objects at low photometric masses whose mass difference remains large. These are most likely unresolved double degenerates for which the inferred photometric masses are underestimated since the radius of these objects has been determined from the photometric technique under the assumption of a single star.

We finally point out that our $\log g$ correction procedure directly results in larger spectroscopic distances, and as such, the number of stars in our local sample, defined within a given volume of space, might eventually be reduced.

2.5.5 Adopted Atmospheric Parameters

The final parameters for all white dwarfs in our sample are selected using the following criteria. For stars with $T_{\text{eff}} > 13,000$ K, spectroscopic solutions were systematically privileged over photometric solutions, when available. To avoid the high- $\log g$ problem below $T_{\text{eff}} = 13,000$ K, photometric solutions were adopted, when available, and in the last resort, spectroscopic solutions corrected for $\log g$ were used. Since photometric analyses of stars with no trigonometric parallax measurements assume a value of $\log g = 8.0$, these are only taken into account in the calculation of the luminosity function presented below, but not in the analysis of the mass distributions. All suspected or confirmed double degenerate systems are considered as single objects in what follows.

Our final results are presented in Table 2.4 where we give for each object the effective temperature (T_{eff}), surface gravity ($\log g$), stellar mass (M/M_{\odot}), atmospheric composition (H- or He-dominated), luminosity (L/L_{\odot}), photometric or spectroscopic distances (D in parsecs),

white dwarf cooling time ($\log \tau$), and the method adopted to obtain these parameters.

2.6 Results

2.6.1 Distances

Based on the adopted photometric or spectroscopic distances presented in Table 2.4, we obtain a list of 133 objects for our final $D < 20$ pc sample, within the uncertainties. Before excluding from our sample any object beyond 20 pc, we make sure that the alternate distance estimate — either photometric or spectroscopic, when available — also places this object outside the 20 pc limit. A comparison of this final local sample with that defined by Sion et al. (2009) reveals that 9 white dwarfs have been removed from the sample (0108+277, 0457–004, 0749+426, 0806–661, 0955+247, 1124+595, 1653+385, 1655+215, and 2336–079), while 16 have been included (0101+048, 0236+259, 0243–026, 0419–487, 0532+414, 0810+489, 0856+331, 1008+290, 1208+576, 1242–105, 2039–202, 2039–682, 2126+734, 2248+293, 2347+292, and 2351–335). Note that the 3 white dwarfs without analyzable data (0208–510, 0415–594, and 1132–325) are not included in our analysis below but these are not necessarily excluded from the local sample. From this point on, when we refer to the local sample, we restrict ourselves to this list of 133 objects that have distance estimates inside the 20 pc region, within the quoted uncertainties.

2.6.2 Mass Distributions

The mass distribution as a function of effective temperature for each star in our sample is displayed in Figure 2.17. Atmospheric compositions and spectral types are indicated with different symbols. In particular, filled and open symbols represent hydrogen- and helium-rich compositions, respectively. For the hydrogen-rich stars, we also indicate which of the spectroscopic or photometric method has been used (helium-rich stars all rely on the photometric method since there are no hot DB stars in our sample). Also superposed in this figure are the theoretical isochrones for our C/O core evolutionary models with thick hydrogen layers, as well as the corresponding isochrones with the main sequence lifetime added to the white

dwarf cooling age (for $\tau \geq 2$ Gyr isochrones only); here we simply assume (Leggett et al. 1998) $t_{\text{MS}} = 10(M_{\text{MS}}/M_{\odot})^{-2.5}$ Gyr and $M_{\text{MS}}/M_{\odot} = 8 \ln[(M_{\text{WD}}/M_{\odot})/0.4]$. As can be seen from these results, white dwarfs with $M \lesssim 0.48 M_{\odot}$ cannot have C/O cores, and yet have been formed from single star evolution within the lifetime of the Galaxy. Some of these low-mass objects must either be unresolved double degenerates, or single white dwarfs with helium cores. In the former case, the stellar masses inferred from these figures are underestimated — especially if the unresolved components have comparable luminosities, and the corresponding cooling ages derived here become meaningless. The second possibility corresponds to single (or binary) helium-core degenerates whose core mass was truncated by Case B mass transfer before helium ignition was reached.

The objects displayed in red in Figure 2.17 are double degenerate binaries *confirmed* from radial velocity measurements: G1-45 (0101+048; Zuckerman et al. 2003), L870-2 (0135–052; Saffer et al. 1988), and L587-77A (0326–073; Zuckerman et al. 2003). The typical photometric masses inferred here for these systems are the order of $\sim 0.3 M_{\odot}$, a direct consequence of the fact that we assumed that these stars are single objects, and thus overestimated their stellar radius by a factor of $\sqrt{2}$ (see equation 2.3), if both components are identical. Had we assumed two stars instead of one, a simple calculation yields photometric masses of $\sim 0.58 M_{\odot}$, right in the bulk of normal white dwarfs. A good example of this calculation is for L870-2 (0135–052) with an extremely low photometric mass of $0.24 M_{\odot}$ (at $T_{\text{eff}} = 7260$ K). Assuming two identical DA stars yields instead $0.46 M_{\odot}$ for both components, in excellent agreement with the (corrected) spectroscopic mass of $0.48 M_{\odot}$ given in Table 3; the spectroscopic mass is not affected by the presence of two DA stars if they have comparable atmospheric parameters (see Fig. 1 of Liebert et al. (1991)). It turns out, indeed, that the two DA components in the L870-2 system are virtually identical (Bergeron et al. 1989). Hence, most, if not all low-mass stars observed in Figure 2.17 are probably unresolved double degenerates. However, a simple mass redetermination as prescribed above is not so simple. For instance, L532-81 (0839–327) with a spectroscopic mass of $0.43 M_{\odot}$ (at $T_{\text{eff}} = 8950$ K) is already in perfect agreement with its spectroscopic mass of $0.42 M_{\odot}$. In this particular case, assuming two DA stars would be the wrong thing to do, as this object appears to be a single DA star. We note, however, that

the photometric fit for this object, shown in Figure 2.9(h), reveals a significant discrepancy at H α , which can easily be explained if the companion star is a DC white dwarf. It is thus not a simple task to deconvolve the individual components of these unresolved binary systems, and their mass determinations should therefore be taken with caution.

Going back to Figure 2.17, we can see that, not unexpectedly, the local sample is predominantly composed of cool white dwarfs. The first striking feature we observe is the complete absence of white dwarfs with helium-rich atmospheres above $T_{\text{eff}} \sim 13,000$ K. To illustrate this more quantitatively, we show in the left panel of Figure 2.18 the total number of stars as a function of effective temperature per bin size of 2000 K, as well as the contribution of the hydrogen-rich atmosphere white dwarfs only. Also, in the right panel, we show the ratio of helium-atmosphere white dwarfs to the total number of stars. The number of helium-rich white dwarfs peaks between 6000 and 8000 K, but drops above and below this temperature range. Clearly, these results indicate that some physical mechanisms are transforming the surface composition of white dwarf stars as they cool off. The most obvious mechanism in this temperature range is convective mixing, where the thin convective hydrogen atmosphere is mixed with the deeper and more massive helium convection zone. Since the depth of the hydrogen convection zone increases at cooler temperatures, the temperature at which mixing occurs becomes a function of the mass of the hydrogen envelope; the thicker the hydrogen layer, the cooler the mixing temperature. If this interpretation is correct, our results suggest that convective mixing occurs for a significant fraction ($\sim 50\%$) of DA stars below $T_{\text{eff}} \sim 10,000$ K or so. This confirms the results obtained by Tremblay & Bergeron (2009) who performed a model atmosphere analysis of cool white dwarfs with 2MASS infrared photometry available, to show that the ratio of helium- to hydrogen-atmosphere white dwarfs increases gradually from a constant value of ~ 0.25 between $T_{\text{eff}} = 15,000$ K and 10,000 K to a value twice as large in the range $10,000 > T_{\text{eff}} > 8000$ K. Our results and those of Tremblay et al. imply that a significant fraction of DA stars, as much as 50% according to our analysis, may have hydrogen mass layers in the range $M_{\text{H}}/M_{\text{tot}} = 10^{-10}$ to 10^{-8} (see Tremblay & Bergeron 2009 for details).

The drop of helium-to-hydrogen atmosphere ratio below 6000 K is more complicated to

explain. This actually corresponds to the location of the non-DA gap between roughly 5000 K and 6000 K where virtually all white dwarfs are DA stars (see Fig. 2.17). Several exotic mechanisms have been proposed by BRL97 to explain this gap although none appears completely satisfactory, and we simply refer the reader to their discussion (see their Fig. 35 and Section 6.3.2). This is even complicated by the fact that helium-rich white dwarfs seem to reappear in large numbers below 5000 K.

We also notice in Figure 2.17 that there appears to be a deficiency of massive stars below $T_{\text{eff}} \sim 7000$ K with respect to what is observed at higher temperatures. Since these objects have not yet reached the stage of crystallization (which we see here as the rapid reduction of the cooling timescales at high mass), we should expect such massive white dwarfs to be present in larger numbers in the local sample. Another way of saying this, the oldest objects in Figure 2.17 have a total age of roughly 9.5 Gyr or so, while there are no massive white dwarfs older than 4.5 Gyr. One could argue that since these massive stars have smaller radii and are thus less luminous, perhaps they have simply gone undetected in proper motion surveys. However, the coolest massive white dwarf in Figure 2.17 is G108-26 (0644+025), and its luminosity ($\log L/L_{\odot} = -3.76$) is not particularly low compared to other objects in Table 2.4. A more plausible explanation is that all the massive white dwarfs observed here are the results of mergers. In this case their cooling ages cannot be interpreted directly from the isochrones shown here since these assume single star evolution; the cooling ages inferred here represent lower estimates at best. If this interpretation is correct, our results suggest that such mergers in the solar neighborhood may not have had the time to cool off to low temperatures ($T_{\text{eff}} \lesssim 7000$ K) within the age of the local galactic disk.

A similar situation can be observed at the low end of the mass distribution in Figure 2.17, where all low-mass white dwarfs are found only at low effective temperatures, $T_{\text{eff}} \lesssim 7000$ K, and most have hydrogen-rich atmospheres of the DA type. There are no low-mass white dwarfs found at higher temperatures, despite the fact these are abundant in spectroscopic analyses of DA stars discovered in UV-excess surveys, such as the PG survey (see, e.g., Fig. 12 of Liebert et al. 2005). First, even though these are relatively cool, their white dwarf cooling age is only of the order of 1 to 2 Gyr. Actually most of these objects are probably unresolved double

degenerates, as discussed above, and they are likely to be the result of common envelope evolution. As such, it is difficult to interpret their location in this diagram. And as discussed in BLR01, we are forced to conclude that this particular evolutionary channel does not produce helium-rich atmosphere white dwarfs, presumably because the objects which go through this close-binary phase end up with hydrogen layers too massive to allow the DA to DB conversion near $T_{\text{eff}} \sim 30,000$ K, or below.

The mass distribution of all white dwarfs in our sample, regardless of their effective temperature, is displayed in Figure 2.19. We also show here the separate contributions of hydrogen- and helium-rich stars. The mean mass of the local sample is $\langle M \rangle = 0.643 M_{\odot}$ with a standard deviation of $\sigma_M = 0.163 M_{\odot}$, while the corresponding values for the hydrogen-atmosphere white dwarfs are $\langle M \rangle = 0.633 M_{\odot}$ and $\sigma_M = 0.173 M_{\odot}$, and for the helium-atmosphere white dwarfs, $\langle M \rangle = 0.663 M_{\odot}$ and $\sigma_M = 0.140 M_{\odot}$. The larger dispersion of the hydrogen stars is a direct result of the presence of both low- and high-mass tails, which are clearly less pronounced in helium-rich atmosphere white dwarfs. A similar conclusion was also reached by BLR01. Actually, an examination of Figure 2.19 reveals that the median mass values and the overall shape of the peak distributions for both atmospheric compositions are remarkably similar. This result is in sharp contrast with the results obtained by Kepler et al. (2007) in their spectroscopic analyses of DA and DB stars identified in the Data Release 4 of the SDSS. Their results, restricted to effective temperatures above 16,000 K, yield $\langle M \rangle_{\text{DA}} \simeq 0.593 M_{\odot}$ and $\langle M \rangle_{\text{DB}} \simeq 0.683 M_{\odot}$, a significantly larger difference than that obtained here. Since Kepler et al. rely solely on the spectroscopic approach, there could be an indication that this method still needs further investigations. We note, however, that the mass distribution obtained by Beauchamp et al. (1996, see also Bergeron et al. 2010) for brighter DB stars, based also on the spectroscopic technique, is in much better agreement with that inferred for DA stars. So the problem may lie with the analysis of Kepler et al., or with the SDSS data, or both.

Now if we focus on the hydrogen-rich white dwarfs only, we can compare our mean mass with those inferred from other surveys. BLR01 found for their hydrogen-rich subsample $\langle M \rangle = 0.61 M_{\odot}$, a value noticeably lower (by $0.02 M_{\odot}$) than that obtained here. However a comparison of the mass distributions (see Fig. 22 of BLR01) reveals that the discrepancy

comes mainly from the low-mass tail, which is far less predominant in the local population.

We can also compare our results with spectroscopic analyses of hotter DA stars. For instance, Tremblay et al. (2011, see their Table 4) report a mean mass of $\langle M \rangle = 0.638 M_{\odot}$ for bright DA stars drawn from the Villanova White Dwarf catalog, in excellent agreement with the value obtained in our analysis. However, the mean mass quoted for the PG magnitude-limited survey, $\langle M \rangle = 0.629 M_{\odot}$, is somewhat lower. But this is actually what is *expected* from such magnitude-limited surveys since massive white dwarfs are intrinsically less luminous than their normal mass counterparts, and therefore their number will be significantly underestimated in a survey limited by the magnitude of the star. On the other hand, less massive white dwarfs, with their larger radii and higher luminosities, will be sampled at much larger distances in a magnitude-limited survey, and will thus be overrepresented.

Focusing again on the mass distribution of hydrogen-rich white dwarfs displayed in Figure 2.19, we can see a distinctive high-mass excess near $1 M_{\odot}$, which appears as a very sharp distribution on its own. Clearly, these cannot represent the descendants of single massive progenitors on the main sequence. Indeed, because of the initial–final mass function, the number of massive white dwarfs expected in such a small volume of space is probably close to zero. Hence the massive white dwarfs in our local sample must be interpreted as mergers. Worse than that, since we have indeed a volume-limited sample, we are forced to conclude that the fraction of mergers in the Galaxy must be enormous. According to our results, 7% of the hydrogen-rich white dwarfs in our sample are mergers. The fact that the mass distribution of these mergers is so narrow also suggests a common evolutionary scenario for these systems. Simplistically, if we interpret these $\sim 1 M_{\odot}$ white dwarfs as the result of the merging of two $\sim 0.5 M_{\odot}$ components, we could explain the apparent deficiency of hydrogen-rich white dwarfs in the $0.50 - 0.55 M_{\odot}$ mass range observed in Figure 2.19! After all, the local disk is old enough to have formed a sufficiently large number of white dwarfs in this particular mass range, and yet very few are present in our local sample.

2.6.3 White Dwarf Luminosity Function

The white dwarf luminosity function (WDLF) is, by definition, a measure of the space density of white dwarfs as a function of luminosity, expressed here as the number of stars per pc³ per unit of bolometric magnitude. In order to get an accurate picture of this function, the exercise has to be rigorously performed with a well-defined sample, and thus the most important requirement for a proper determination rests on the completeness of the sample. The most recent determination of the WDLF, covering the entire range of bolometric magnitudes ($7 \lesssim M_{\text{bol}} \lesssim 16$) was presented by Harris et al. (2006) using a magnitude-limited survey, namely the Sloan Digital Sky Survey. Several corrections for completeness and contamination had to be made, however, to counterbalance important selection effects present in the SDSS sample. This is of course the case with all magnitude-limited surveys (see, e.g., Liebert et al. 2005 for the PG survey and Limoges & Bergeron 2010 for the KUV survey), and not only the SDSS. Using a volume-limited survey avoids most of the problems inherent to these previous determinations, and provides a non-biased sample where completeness issues are better controlled. The most obvious drawback, unfortunately, is the small size of the sample, which may lead to significant statistical uncertainties. Hence a detailed comparison of both methods for determining the WDLF is much desired.

The WDLF calculated here is based on the derived bolometric magnitude of each white dwarf in our sample, obtained via the spectroscopic or photometric methods presented in Table 2.4 ($M_{\text{bol}} = -2.5 \log L/L_{\odot} + M_{\text{bol}}^{\odot}$ where $M_{\text{bol}}^{\odot} = 4.75$ is the bolometric magnitude of the Sun). A total of 133 nearby ($D < 20$ pc) white dwarfs are taken into account for the WDLF calculation; we also assume that our sample is complete, which is probably not the case (the $D < 20$ pc sample is only 80% complete according to Holberg et al. 2008). The luminosity function for the local sample is presented in Figure 2.20, and corresponds to the total number of stars (given in the figure) in each bin size of 1 bolometric magnitude, divided by the enclosed volume defined by the 20 pc limit. Our determination of the WDLF is also compared in this figure with that obtained by Harris et al. (2006) using the SDSS sample. As expected, the WDLF for the local sample is not as smooth as the SDSS luminosity function due to the smaller number of stars implied in our calculations. The overall trend, however,

is quite similar but with a clear tendency in our results to overestimate the space density at the bright end of the luminosity function ($M_{\text{bol}} \lesssim 12$), obviously due to the small number of white dwarfs in the brightest magnitude bins (only ~ 8 stars or less per bin). Thus, the comparison of the luminosity functions in this region is rather meaningless due to the absence of hot nearby white dwarfs in the local sample. These small number statistics will eventually be improved when the volume of the local sample is increased to larger distances, such as the effort of Limoges et al. (2010) to define a complete sample of white dwarf stars within a distance of 40 pc from the Sun.

The results at the fainter end of the luminosity function, where the number of stars in each magnitude bin of the local sample is more statistically significant, are in better agreement. We obtain a larger space density in our sample in these particular magnitude bins ($M_{\text{bol}} > 12$) than in the SDSS, and it is expected that our values are more realistic since the SDSS clearly underestimates the number of cool white dwarfs in their survey. Indeed, white dwarf stars identified in the SDSS are based on selections in color-color diagrams, and white dwarfs with effective temperatures below $T_{\text{eff}} \sim 8000$ K overlap with A and F main-sequence stars in such color diagrams, and cool white dwarfs are thus usually excluded from further selection.

Finally, by integrating the luminosity function over all magnitude bins, we can determine the total space density of white dwarfs, and their contribution to the mass budget of the local galactic disk. We obtain a total space density of 4.0×10^{-3} pc $^{-3}$ for a corresponding mass density of $2.5 \times 10^{-3} M_{\odot}$ pc $^{-3}$. If we compare our results to the values obtained by Holberg et al. (2008) *from the complete portion of the sample within 13 pc* — a space density of $4.8 \pm 0.5 \times 10^{-3}$ pc $^{-3}$ and a mass density of $3.2 \pm 0.3 \times 10^{-3} M_{\odot}$ pc $^{-3}$ — we can assess the completeness of our sample to be slightly higher than 80%, an estimate that compares well with that inferred by Holberg et al. (2008). This result is not surprising as the total number of objects in our local sample remains comparable to that used by Holberg et al. Note that these determinations are not affected by the fact that our sample underestimates the number of hot white dwarfs since the contribution of these stars to the space and mass densities is almost negligible (see Fig. 2.20).

2.7 Summary and Conclusion

A detailed photometric and spectroscopic analysis of the 164 white dwarfs nearby candidates was presented. Homogeneous determinations of the atmospheric parameters of the local population were performed based on state-of-the-art model atmospheres and improved photometric calibrations. We developed a method for correcting the $\log g$ values at low effective temperatures ($T_{\text{eff}} < 13,000$ K) where the so-called high- $\log g$ problem occurs, and which would have prevented us from obtaining reliable mass and distance estimates.

We found a mean mass of $0.643 M_{\odot}$ for the complete sample, with corresponding values of $0.633 M_{\odot}$ and $0.663 M_{\odot}$ for the hydrogen- and helium-atmosphere white dwarfs, respectively. Hence there is no indication for differences in the mean mass values between these two populations, although the mass distribution of hydrogen white dwarfs contains a significantly larger number of low- and high-mass stars. The mean mass for hydrogen-atmosphere white dwarfs is entirely consistent that obtained for bright DA stars in the Villanova White Dwarf Catalog, $0.638 M_{\odot}$ (see Table 4 of Tremblay et al. 2011). The large fraction of massive stars observed in the local sample has been interpreted as the result of mergers. The main argument for the merger hypothesis is that these massive white dwarfs cannot have evolved from massive main sequence progenitors since the Sun is not located in a region of active star formation where such massive progenitors could be found.

The local volume-limited sample represents a snapshot of what a representative sample of white dwarf looks like. The small spectral atlas displayed here reveals that peculiar white dwarfs are not rare objects, on the contrary. It is thus not surprising that large surveys such as the SDSS revealed even stranger objects. Interestingly enough, most of what we know about the mean properties of white dwarf stars comes from the spectroscopic analysis of hot ($T_{\text{eff}} \gtrsim 15,000$ K) DA stars with their comfortable radiative, pure hydrogen atmospheres. Our local sample contains only ~ 10 of these DA stars. A more typical white dwarf has instead a convective atmosphere, with quite often a helium-dominated atmosphere, with more than occasionally traces of heavier elements. These objects represent a challenge in terms of the modeling of their energy distribution.

The white dwarf luminosity function we derived here for the local sample follows the

exact same trend as that previously obtained in many studies, including the SDSS, except at higher luminosities where the local sample contains very few objects. This portion of the luminosity function will eventually be improved by surveys aimed at pushing the local sample to a distance of 40 pc (Limoges et al. 2010), an increase by a factor of 8 in terms of volume. But the total space density we derived here, 4.0×10^{-3} white dwarfs per cubic parsec, is not affected by this deficiency of hot stars in the local sample. Note that our space density is comparable to the value obtained by Leggett et al. (1998), $3.39 \times 10^{-3} \text{ pc}^{-3}$, based on the model atmosphere analysis of the 43 white dwarfs in the proper motion sample of Liebert et al. (1988). The value of the space density of white dwarfs in the galactic disk is not likely to change.

We wish to thank P.-E. Tremblay, A. Gianninas, and M.-M. Limoges for precious advices and collaboration. We also wish to thank the director and staff of Steward Observatory and NOAO for the use of their facilities. This work was supported in part by the NSERC Canada.

2.8 References

- Bauchamp, A., Wesemael, F., & Bergeron, P. 1997, ApJS, 108, 559
- Bauchamp, A., Wesemael, F., Bergeron, P., Liebert, J., & Saffer, R. A. 1996, Hydrogen Deficient Stars, 96, 295
- Bergeron, P., et al. 2010, in 17th European White Dwarf Workshop, American Institute of Physics Conference Series, eds. K. Werner & T. Rauch, 1273, 7
- Bergeron, P., Leggett, S. K., & Ruiz, M. T. 2001, ApJS, 133, 413 (BLR01)
- Bergeron, P., Ruiz, M. T., & Leggett, S. K. 1992, ApJ, 400, 315
- Bergeron, P., Ruiz, M. T., & Leggett, S. K. 1997, ApJS, 108, 339 (BRL97)
- Bergeron, P., Ruiz, M. T., Leggett, S. K., Saumon, D., & Wesemael, F. 1994, ApJ, 423, 456
- Bergeron, P., Saffer, R. A., & Liebert, J. 1992, ApJ, 394, 228
- Bergeron, P., Saumon, D., & Wesemael, F. 1995, ApJ, 443, 764
- Bergeron, P., Wesemael, F., Fontaine, G., & Liebert, J. 1990, ApJ, 351, L21
- Bergeron, P., Wesemael, F., Liebert, J. & Fontaine, G. 1989, ApJ, 345, L91
- Bessell, M. S., & Brett, J. M. 1988, PASP, 100, 1134
- Cohen, M., Wheaton, W. A., & Megeath, S. T. 2003, AJ, 126, 1090
- Dahn, C. C., et al., 1987, Pub. U. S. Naval Obs., Eight Parallax List.
- Ducourant, C., Teixeira, R., Hambly, N. C., Oppenheimer, B. R., Hawkins, M. R. S., Rappaport, M., Modolo, J., & Lecampion, J. F. 2007, A&A, 470, 387
- Dufour, P., Bergeron, P., & Fontaine, G. 2005, ApJ, 627, 404
- Dufour, P., et al. 2007, ApJ, 663, 1291
- Farihi, J., Becklin, E. E., & Zuckerman, B. 2005, ApJS, 161, 394
- Fontaine, G., Brassard, P., & Bergeron, P. 2001, PASP, 113, 409
- Gianninas, A., Bergeron, P., & Ruiz, M. T. 2010, xxx, xxx, xxx
- Gianninas, A., Dufour, P., & Bergeron, P. 2004, ApJ, 617, L57
- Giclas, H.L., Burnham, R., JR., Thomas, N.G., 1980, Lowell Obs. Bull. No. 166.

- Gliese, W., & Jahreiß, H. 1979, A&AS, 38, 423
- Greenstein, J. L. 1984, ApJ, 276, 602
- Harris, H. C., et al. 2006, AJ, 131, 571
- Holberg, J. B., & Bergeron, P. 2006, ApJ, 132, 1221
- Holberg, J. B., Oswalt, T. D., & Sion, E. M. 2002, ApJ, 571, 512
- Holberg, J. B., Sion, E. M., Oswalt, T., McCook, G. P., Foran, S., & Subasavage, J. P. 2008, AJ, 135, 1225
- Hintzen, P., & Jensen, E. 1979, PASP, 91, 492
- Hummer, D. G., & Mihalas, D. 1988, ApJ, 331, 794
- Kawka, A., & Vennes, S. 2006, ApJ, 643, 402
- Kawka, A., Vennes, S., & Thorstensen, J. R. 2004, AJ, 127, 1702
- Kepler, S. O., Kleinman, S. J., Nitta, A., Koester, D., Castanheira, B. G., Giovannini, O., Costa, A. F. M., & Althaus, L. 2007, MNRAS, 375, 1315
- Kilic, M., Thorstensen, J. R., & Koester, D. 2008, ApJ, 689, L45
- Kowalski, P. M. 2010, A&A, 519, L8
- Landolt, A. U. 1992a, AJ, 104, 340
- Landolt, A. U. 1992b, AJ, 104, 372
- Leggett, S. K. 1992, ApJS, 82, 351
- Leggett, S. K., Ruiz, M. T., & Bergeron, P. 1998, ApJ, 497, 294
- Liebert, J., Bergeron, P., & Holberg, J. B. 2005, ApJS, 156, 47
- Liebert, J., Bergeron, P., & Saffer, R. A. 1991, NATO ASIC Proc. 336: White Dwarfs, 409
- Liebert, J., Dahn, C. C., & Monet, D. G. 1988, ApJ, 332, 891
- Limoges, M.-M., & Bergeron, P. 2010, ApJ, 714, 1037
- Limoges, M.-M., Bergeron, P., & Lépine, S. 2010, American Institute of Physics Conference Series, 1273, 193
- McCook, G. P., & Sion, E. M. 1999, ApJS, 121, 1

- Perryman, M. A. C., & ESA 1997, ESA Special Publication, 1200,
- Press, W. H., Flannery, B. P., & Teukolsky, S. A. 1986, Cambridge: University Press, 1986
- Ruiz, M. T., Anguita, C., & Maza, J. 1989 in IAU Colloquium 114, White Dwarfs, ed. G. Wegner (New York: Springer), 122
- Saffer, R. A., Bergeron, P., Koester, D., & Liebert, J. 1994, ApJ, 432, 351
- Saffer, R. A., Liebert, J., & Olszewski, E. M. 1988, ApJ, 334, 947
- Salim, S., & Gould, A. 2003, ApJ, 582, 1011
- Schmidt, G. D., Liebert, J., Harris, H. C., Dahn, C. C., & Leggett, S. K. 1999, ApJ, 512, 916
- Schmidt, G. D., & Smith, P. S. 1994, ApJ, 423, L63
- Sion, E. M., Holberg, J. B., Oswalt, T. D., McCook, G. P., & Wasatonic, R. 2009, AJ, 138, 1681
- Subasavage, J. P., Henry, T. J., Bergeron, P., Dufour, P., & Hambly, N. C. 2008, AJ, 136, 899
- Subasavage, J. P., Henry, T. J., Bergeron, P., Dufour, P., Hambly, N. C., & Beaulieu, T. D. 2007, AJ, 134, 252
- Subasavage, J. P., Jao, W.-C., Henry, T. J., Bergeron, P., Dufour, P., Ianna, P. A., Costa, E., & Méndez, R. A. 2009, AJ, 137, 4547
- Tremblay, P.-E., & Bergeron, P. 2007, ApJ, 657, 10
- Tremblay, P.-E., & Bergeron, P. 2008, ApJ, 672, 1144
- Tremblay, P.-E., & Bergeron, P. 2009, ApJ, 696, 1755
- Tremblay, P.-E., Bergeron, P., & Gianninas, A. 2010, submitted to ApJ
- Tremblay, P.-E., Bergeron, P., Kalirai, J. S., & Gianninas, A. 2010, ApJ, 712, 1345
- van Altena, W. F., Lee, J. T., & Hoffleit, E. D. 1994, The General Catalogue of Trigonometric Parallaxes (New Haven: Yale University Observatory)
- Vennes, S., & Kawka, A. 2003, ApJ, 586, L95
- Vidal, C. R., Cooper, J., & Smith, E. W. 1970, J. Quant. Spec. Radiat. Transf., 10, 1011

- Wesemael, F., Greenstein, J. L., Liebert, J., Lamontagne, R., Fontaine, G., Bergeron, P., & Glaspey, J. W. 1993, PASP, 105, 761
- Wood, M. A. 1995, White Dwarfs, 443, 41
- Zuckerman, B., Koester, D., Reid, I. N., & Huumlnsch, M. 2003, ApJ, 596, 477

2.9 Tables

TABLE 2.1 – OBSERVATIONAL RESULTS

WD	Name	Spectral Type	π (mas)	σ_π (mas)	$B - V$	$V - R$	$V - I$	J	$H - H$	$H - K$	Notes
0000–345	LHS 1008	DC	75.7	9.0	15.02	+0.44	+0.30	+0.57	14.17	+0.15	+0.15
0008+423	GD 5	DA	1,2
0009+501	LHS 1038	DAH	90.6	3.7	14.36	+0.45	+0.28	+0.59	13.41	+0.15	+0.05
0011–134	LHS 1044	DAH	51.3	3.8	15.89	+0.63	+0.33	+0.67	14.85	+0.23	+0.10
0011–721	LP 50–73	DA	15.17	...	+0.30	+0.62	14.21	+0.24	+0.06
0038–226	LHS 1126	DQ	101.2	10.4	14.50	+0.70	+0.42	+0.79	13.32	-0.15	-0.24
0046+051	vMa 2	DZ	226.95	5.35	12.39	+0.52	+0.26	+0.49	11.69	+0.08	+0.09
0101+048	G1–45	DA	46.9	3.8	14.00	+0.26	+0.17	+0.34	13.51	+0.12	+0.01
0108+277	LP 294–61	DAZ	16.15	15.22	+0.18	+0.17
0115+159	LHS 1227	DQ	64.9	3.0	13.85	+0.10	+0.11	+0.20	13.72	+0.00	-0.02
0121–429	LHS 1243	DAH	54.61	0.96	14.83	13.86	+0.22	+0.11
0123–262	LHS 1247	DC	...	15.06	+0.33	+0.22	+0.44	14.50	+0.14	-0.02	3,5
0135–052	L870–2	DA	81.0	2.8	12.86	+0.33	+0.23	+0.48	12.12	+0.18	+0.02
0141–675	LHS 145	DA	1,2
0148+467	GD 279	DA	63.08	3.39
0148+641	G244–36	DA
0208+396	G74–7	DAZ	59.8	3.5	14.51	+0.33	+0.25	+0.47	13.80	+0.15	+0.02
0208–510	GJ 86 B	DA	91.63	0.56	1,2
0213+427	LHS 153	DA	50.2	4.1	16.22	+0.73	+0.45	+0.85	14.98	+0.25	+0.21
0230–144	LHS 1415	DA	64.0	3.9	15.77	+0.69	+0.43	+0.84	14.43	+0.26	+0.06
0233–242	LHS 1421	DC	15.74	14.45	+0.11	+0.22
0236+259	G36–29	DA	16.29	14.91	+0.31	+0.14
0243–026	LHS 1442	DA	47.1	5.0	15.54	+0.40	+0.26	+0.53	14.71	+0.22	-0.02
0245+541	LHS 1446	DAZ	96.6	3.1	15.36	+0.92	+0.52	+1.00	13.89	+0.23	+0.06
0255–705	LHS 1474	DA	1,2
0310–688	LB 3303	DA	98.50	1.24
0322–019	G77–50	DAZ	59.5	3.2	16.12	+0.82	+0.46	+0.88	14.63	+0.26	+0.09
0326–273	L587–77A	DA	57.6	13.6	14.00	13.27	+0.15	+0.04
0341+182	Wolf 219	DQ	52.6	3.0	15.19	+0.33	+0.28	+0.54	14.56	+0.21	-0.05
0344+014	LP 593–56	DC	...	16.52	15.00	+0.12	+0.17

TABLE 2.1 – continued.

WD	Name	Spectral Type	π (mas)	σ_π (mas)	V	B-V	V-R	V-I	J	J-H	H-K	Notes
0357+081	LHS 1617	DA	56.1	3.7	15.92	+0.70	+0.41	+0.83	14.59	+0.26	+0.07	1,2
0413-077	40 ERI B	DAP	198.24	0.67	13
0415-594	HD 27442B	DA	13,14
0419-487	LHS 1660	DA+DM	14.36	+0.50	+0.63	+1.92	1,2
0423+120	G83-10	DC	57.6	2.5	15.42	+0.48	+0.31	+0.62	14.52	+0.18	+0.07	
0426+588	Stein 2051B	DQ	181.36	3.67	12.43	+0.30	+0.26	+0.57	11.84	+0.11	+0.05	1,2
0433+270	G39-27	DA	56.02	1.21	15.81	+0.67	+0.41	+0.80	14.61	+0.29	+0.10	1,2
0435-088	L879-14	DQ	105.2	2.6	13.75	+0.33	+0.32	+0.57	13.00	+0.15	+0.06	1,2
0457-004	G84-26	DA	
0503-174	LHS 1734	DAH	45.6	4.0	16.01	+0.72	+0.44	+0.90	14.55	+0.22	+0.10	1,2
0532+414	GD 69	DA	14.56	+0.52	
0548-001	G99-37	DQP	90.3	2.8	14.47	+1.01	+0.50	+0.98	13.02	+0.12	+0.08	1,2
0552-041	LP 658-2	DZ	155.0	2.1	14.47	+0.62	+0.38	+0.75	12.96	+0.19	+0.11	1,2
0553+053	G99-47	DAP	125.0	3.6	14.16	+0.62	1,2
0642-166	Sirius B	DA	379.83	1.05	13
0644+025	G108-26	DA	54.2	5.5	15.71	+0.35	+0.23	+0.46	15.00	+0.15	-0.08	1,2
0644+375	G87-7	DA	64.91	2.93	
0655-390	L454-9	DA	15.11	...	+0.30	+0.63	14.15	+0.27	-0.01	3,6,14
0657+320	LHS 1889	DA	53.5	0.9	16.62	+1.02	+0.53	+1.01	14.99	+0.22	+0.08	1,2
0659-063	LHS 1892	DA	81.00	24.2	
0708-670	SCR 0708-6706	DC	16.22	...	+0.50	+1.01	14.71	+0.06	+0.19	3,6,14
0727+482A	G107-70A	DA	90.0	1.0	15.26	+0.98	+0.53	+1.02	13.66	+0.24	+0.09	1,2
0727+482B	G107-70B	DA	90.0	1.0	15.56	+0.98	+0.53	+1.02	13.96	+0.24	+0.09	1,2
0728+642	G234-4	DAP	16.38	14.81	+0.30	+0.13	3,7
0736+053	Procyon B	DQZ	285.93	0.88	10.94	+0.25	+0.15	+0.27	13
0738-172	L745-46A	DZA	112.4	2.7	13.06	+0.24	+0.18	+0.34	12.65	+0.04	+0.09	1,2
0743-340	vB 3	DC	65.79	0.56	16.60	+1.21	+0.64	+1.21	14.85	+0.14	+0.16	1,2,13
0747+073A	LHS 240	DC	54.7	0.7	16.63	+1.06	+0.58	+1.08	14.96	+0.23	+0.01	1,2
0747+073B	LHS 239	DC	54.7	0.7	16.96	+1.21	+0.65	+1.26	15.05	+0.15	+0.04	1,2
0749+426	LP 207-50	DC	17.45	15.72	-0.08	+0.97	3,4

TABLE 2.1 – continued.

WD	Name	Spectral Type	π (mas)	σ_π (mas)	V	B – V	V – R	V – I	J	J – H	H – K	Notes
0751–252	SCR 0753–2524	DA	55.05	0.8	16.27	...	+0.49	+0.96	14.75	+0.28	+0.17	3,6,14
0752–676	BPM 4729	DA	141.2	8.4	13.95	+0.65	+0.37	+0.75	12.79	+0.27	+0.09	1,2
0806–661	L97–3	DQ	13.71	+0.03	+0.07	+0.11	13.79	-0.06	-0.07	1,2
0810+489	G111–64	DC	15.74	14.32	+0.19	+0.07	3,4
0816–310	SCR 0818–3110	DZ	15.43	...	+0.22	+0.38	14.92	+0.19	-0.10	3,6,14
0821–669	SCR 0821–6703	DA	92.37	1.04	15.34	...	+0.52	+1.02	13.79	+0.22	+0.23	3,5
0827+328	LHS 2022	DA	44.9	3.8	15.73	+0.32	+0.22	+0.47	15.01	+0.16	+0.01	1,2
0839–327	L532–81	DA	112.7	9.7	11.90	+0.25	11.59	+0.04	+0.00	1,2
0840–136	LP 726–1	DZ	15.72	...	+0.36	+0.70	14.62	+0.21	-0.13	3,5
0843+358	GD 95	DZ	14.81	14.68	+0.05	+0.04	3,8
0856+331	G47–18	DQ	48.8	3.4	15.16	+0.03	+0.13	+0.19	15.12	+0.03	-0.02	1,2
0912+536	G195–19	DCP	97.3	1.9	13.84	+0.35	+0.20	+0.33	13.22	+0.07	+0.06	1,2
0939+071	GR 431	NWD	18
0946–534	G195–42	DQ	43.5	3.5	15.18	+0.17	+0.13	+0.28	14.90	+0.03	-0.01	1,2
0955+247	G49–33	DA	40.9	4.5	15.06	+0.24	+0.12	+0.32	14.66	+0.07	-0.06	1,2
1008+290	LHS 2229	DQpec	67.47	0.47	17.51	+0.70	...	+1.95	15.01	+0.30	+0.16	17
1009–184	LEHPM 2– 220	DZ	55.55	0.85	15.44	...	+0.26	+0.53	14.68	+0.17	+0.20	3,5,13,16
1019+637	LP 62–147	DA	61.2	3.6	14.70	+0.38	+0.25	+0.53	13.83	+0.20	-0.02	1,2
1033+714	LHS 285	DC	16.88	+1.08	+0.55	+1.08	1,2
1036–204	LP 790–29	DQP	16.28	+0.09	+0.71	+0.93	14.70	+0.42	+0.19	1,2
1043–188	LHS 290	DQ	56.9	6.5	15.52	+0.57	+0.49	...	14.62	+0.21	+0.05	1,2
1055–072	LHS 2333	DC	82.3	3.5	14.33	+0.30	+0.20	+0.42	13.81	+0.10	+0.02	1,2
1116–470	SCR 1118–4721	DC	15.52	...	+0.32	+0.66	14.45	+0.09	+0.02	3,6,14
1121+216	Ross 627	DA	74.4	2.8	14.21	+0.31	+0.20	+0.45	13.58	+0.18	+0.00	1,2
1124+595	SDSS	DA
1132–325	LHS 309	DC+KO5	13
1134+300	GD 140	DA	65.28	2.67
1142–645	LHS 43	DQ	216.40	2.11	11.49	+0.17	+0.16	+0.29	11.19	+0.07	+0.03	1,2
1202–232	LP 852–7	DAZ
1208+576	LHS 2522	DAZ	48.9	4.6	15.78	+0.57	+0.37	+0.74	14.64	+0.25	+0.07	1,2

TABLE 2.1 – continued.

WD	Name	Spectral Type	π (mas)	σ_π (mas)	V	B - V	V - R	V - I	J	J - H	H - K	Notes
1223-659	L104-2	DA	61.53	1.16	...	0.18	-0.02	-0.03	13.92	+0.02	-0.08	...
1236-495	LTT 4816	DA	61.0	9.4	13.80	0.66	0.38	0.76	14.56	+0.23	+0.08	1,2
1242-105	LP 736-4	DA	14.69	+0.23	+0.12	3,9
1257+037	LHS 2661	DA	60.3	3.8	15.84	0.66	0.38	0.76	14.56	+0.23	+0.08	1,2
1309+853	G 256-7	DAP	55.4	9.3	15.97	14.69	+0.23	+0.12	3,9
1310+583	PG	DA
1310-472	ER 8	DC	66.5	2.4	17.13	+1.39	+0.72	+1.41	15.21	+0.10	+0.08	1,2
1315-781	L40-116	DC	52.14	0.94	16.16	...	+0.43	+0.81	14.89	+0.22	+0.09	3,5
1327-083	Wolf 485A	DA	59.29	2.15
1334+039	Wolf 489	DA	121.4	3.4	14.63	+0.95	+0.51	+1.01	13.06	+0.26	+0.10	1,2
1339-340	PM 13391-3400	DA	16.43	...	+0.43	+0.87	15.00	+0.25	+0.10	3,5,16
1344+106	LHS 2800	DAZ	49.9	3.6	15.12	+0.38	+0.22	+0.48	14.38	+0.18	+0.01	1,2
1345+238	LP 380-5	DA	82.9	2.2	15.71	+1.15	+0.59	+1.13	13.92	+0.25	+0.08	1,2
1350-090	LP 907-37	DA
1425-811	L19-2	DAV
1444-174	LHS 378	DC	69.0	4.0	16.44	+1.03	+0.49	+1.01	14.94	+0.15	+0.11	1,2
1529+141	GD 184	DA	16.56	16.12	+0.20	-0.52	3,4,15
1538+333	GD 187	DA
1544-377	L481-60	DA	65.60	0.77	12.97	+0.18	+0.22	+0.60	14.77	+0.01	+0.01	1,2,13
1609+135	LHS 3163	DA	54.5	4.7	15.11	+0.20	+0.10	+0.24
1620-391	CD-38 10980	DA	77.73	0.31	13.58	+0.01	-0.01	1,3
1626+368	Ross 640	DZA	62.7	2.0	13.83	+0.19	+0.08	+0.17
1632+177	PG	DA
1633+433	G180-63	DAZ	66.2	3.0	14.84	+0.43	+0.27	+0.56	13.95	+0.19	+0.03	1,2
1633+572	G225-68	DQ	69.2	2.5	14.99	+0.50	+0.31	+0.61	14.03	+0.06	-0.02	1,2
1647+591	G226-29	DAV	91.13	2.23
1653+385	LP 276-33	DAZ	15.86	15.53	+0.18	+0.08	3,4
1655+215	LHS 3254	DA	43.0	3.1	14.13	+0.21	+0.10	+0.21	13.89	+0.09	-0.05	1,2
1657+321	LP 331-27	DA	16.92	16.46	-0.15	+0.88	3,4,15
1705+030	G139-13	DZ	57.0	5.4	15.20	+0.43	+0.24	+0.46	14.62	+0.12	+0.02	1,2

TABLE 2.1 – continued.

WD	Name	Spectral Type	π (mas)	σ_π (mas)	V	B - V	V - R	V - I	J	J - H	H - K	Notes
1729+371	GD 362	DABZ	19.9	1.3
1748+708	G240-72	DQP	164.7	2.4	14.13	+0.48	+0.53	+1.05	12.77	+0.07	+0.20	1,2
1756+143	LSR 1758+1417	DA	...	16.30	...	+0.18	+0.61	14.93	+0.27	+0.00	3,5,16	
1756+827	LHS 56	DA	63.9	2.9	14.34	+0.35	+0.22	+0.47	14.38	+0.28	+0.03	1,2
1814+134	LSR 1817+1328	DA	...	15.85	...	+0.51	+0.99	3,5,16
1820+609	G227-28	DA	78.2	4.1	15.69	+0.98	+0.54	+1.05	13.96	+0.23	+0.08	1,2
1829+547	G227-35	DQP	66.8	5.6	15.57	+0.49	+0.29	+0.60	14.76	+0.15	+0.11	1,2
1900+705	GW+70 8247	DAP	77.0	2.3	13.25	+0.06	+0.01	+0.02	1,2
1917+386	G125-3	DC	85.5	3.4	14.61	+0.45	+0.30	+0.57	13.77	+0.08	+0.10	1,2
1917-077	LDS 678A	DBQA	89.08	7.16	12.30	12.35	+0.00	-0.07	3,10
1919+145	GD 219	DA	50.5	5.5	12.98	+0.07	-0.07	-0.44	1,2
1935+276	G185-32	DA	55.70	2.9
1953-011	LHS 3501	DAP	87.8	2.9	13.69	+0.28	+0.19	+0.38	13.12	+0.10	+0.00	1,2
2002-110	LHS 483	DC	57.7	0.8	16.95	+1.16	+0.59	+1.09	15.32	+0.21	+0.02	1,2
2007-303	L565-18	DA	65.06	3.39
2008-600	SCR 2012-5956	DC	60.42	0.86	15.84	...	+0.44	+0.85	14.93	-0.31	-0.12	3,5,16
2032+248	G186-31	DA	68.22	1.35
2039-202	LTT 8189	DA
2039-682	LTT 8190	DA
2040-392	L495-82	DA
2047+372	G210-36	DA	15.63	+0.92	+0.52	+1.00	14.12	+0.29	+0.04	1,2
2048+263	G187-8	DA	49.8	3.4	15.42
2048-250	LP 872-20	DA	16.69	+1.20	+0.66	+1.32	14.82	+0.21	+0.07	1,2
2054-050	vB 11	DC	56.56	4.03	13.61	+0.21	+0.05	+0.14	13.52	-0.01	-0.05	1,2
2105-820	L24-52	DAP	58.6	8.8
2115-560	BPM 27273	DA
2117+539	G231-40	DA	50.70	7.4
2126+734	G261-43	DA
2138-332	L570-26	DZ	...	14.47	+0.17	+0.31	14.17	+0.09	+0.13	3,5,16
2140+207	LHS 3703	DQ	79.9	3.2	13.24	+0.13	+0.14	+0.26	12.95	+0.02	-0.02	1,2

TABLE 2.1 – continued.

WD	Name	Spectral Type	π (mas)	σ_π (mas)	V	B - V	V - R	V - I	J	J - H	H - K	Notes
2151-015	G93-53	DA
2154-512	BPM 27606	DQ	61.63	2.67	14.74	+0.19	+0.44	+0.61	13.47	+0.00	+0.18	1,2
2159-754	LHS 3752	DA
2211-392	LEHPM 4466	DA	53.5	2.6	15.92	+0.49	+0.33	+0.66	14.89	+0.25	+0.09	3,11,16
2215+368	LP 287-39	DC	16.99	15.41	+0.21	+0.23	3,4,15
2226-754	SSSPM J2231-7514	DC	16.57	...	+0.64	+1.24	14.66	+0.00	+0.22	3,5,16
2226-755	SSSPM J2231-7515	DC	16.88	...	+0.71	+1.37	14.86	+0.03	+0.10	3,5,16
2246+223	G67-23	DA	52.5	4.1	14.39	+0.17	+0.05	+0.14	14.28	-0.03	-0.06	1,2
2248+293	G128-7	DA	47.8	4.2	15.54	+0.66	+0.40	+0.79	14.24	+0.23	+0.07	1,2
2251-070	LP 701-29	DZ	123.7	4.3	15.71	+1.84	+0.61	+1.15	13.86	+0.23	+0.16	1,2
2322+137	LP 522-46	DA	15.81	14.51	+0.14	+0.01	3,4
2326+049	G29-38	DAZ	73.40	4.0
2336-079	GD 1212	DAZ
2341+322	G130-5	DA	56.80	1.8
2347+292	LHS 4019	DA	46.5	4.1	15.76	+0.59	+0.35	+0.72	14.59	+0.24	+0.11	1,2
2351-335	LHS 4040	DA
2359-434	LHS 1005	DAP	127.4	6.8

Note. – (1) $BVRI$ from Bergeron, Leggett, & Ruiz (2001); (2) JHK from Bergeron, Leggett, & Ruiz (2001); (3) JHK from 2MASS; (4) V from Kawka & Vennes (2006); (5) VRI from Subasavage et al. (2007); (6) VRI from Subasavage et al. (2008); (7) V from Gliese & Jahreiß (1979); (8) V from Giclas et al. (1980); (9) V from Hintzen & Jensen (1979); (10) V from Dahn et al. (1987); (11) $BVRI$ from Bergeron et al. (1995); (12) spectral type from Greenstein (1984); (13) Sirius-like star; (14) Not in Villanova White Dwarf Catalog; (15) Spectral type from Kawka & Vennes (2006); (16) Spectral type from Subasavage et al. (2007); (17) $BVIJHK$ and spectral type from Schmidt et al. (1999); (18) Classified as DC7 in the PG catalog.

TABLE 2.2 – RESULTS FROM PHOTOMETRIC FITS

WD	T_{eff} (K)	$\log g$	M/M_{\odot}	Comp.	$D(\text{pc})$
0000–345	6297 (137)	8.31 (0.17)	0.77 (0.11)	He	13.2 (1.6)
0009+501	6595 (146)	8.22 (0.06)	0.73 (0.04)	H	11.0 (0.5)
0011–134	6065 (122)	8.19 (0.11)	0.71 (0.07)	H	19.5 (1.5)
0011–721	6393 (169)	8.00 (0.00)	0.59 (0.00)	H	17.5 (0.7)
0038–226	5535 (100)	7.95 (0.17)	0.54 (0.10)	H+He	9.9 (1.0)
0046+051	6838 (200)	8.37 (0.03)	0.81 (0.02)	He	4.4 (0.1)
0101+048	8116 (193)	7.53 (0.14)	0.36 (0.05)	H	21.3 (1.7)
0108+277	6485 (179)	8.00 (0.00)	0.59 (0.00)	H	28.1 (1.2)
0115+159	9805 (350)	8.35 (0.06)	0.81 (0.04)	He	15.4 (0.7)
0121–429	6370 (171)	7.65 (0.03)	0.40 (0.01)	H	18.3 (0.3)
0123–262	7281 (191)	8.00 (0.00)	0.58 (0.00)	He	21.7 (0.8)
0135–052	7182 (162)	7.18 (0.06)	0.24 (0.01)	H	12.3 (0.4)
0208+396	7357 (173)	8.00 (0.09)	0.59 (0.05)	H	16.7 (1.0)
0213+427	5657 (167)	8.12 (0.12)	0.66 (0.08)	H	19.9 (1.6)
0230–144	5530 (129)	8.11 (0.09)	0.65 (0.06)	H	15.6 (1.0)
0233–242	5372 (107)	8.00 (0.00)	0.57 (0.00)	He	15.9 (0.6)
0236+259	5315 (130)	8.00 (0.00)	0.58 (0.00)	H	19.3 (0.9)
0243–026	6868 (158)	8.17 (0.15)	0.70 (0.10)	H	21.2 (2.3)
0245+541	5309 (128)	8.27 (0.05)	0.75 (0.03)	H	10.4 (0.3)
0322–019	5235 (130)	8.05 (0.08)	0.61 (0.05)	H	16.8 (0.9)
0326–273	7247 (200)	7.51 (0.40)	0.35 (0.15)	H	17.4 (4.3)
0341+182	6961 (171)	8.15 (0.08)	0.67 (0.05)	He	19.0 (1.1)
0344+014	5058 (92)	8.00 (0.00)	0.57 (0.00)	He	19.5 (0.7)
0357+081	5536 (129)	8.02 (0.10)	0.60 (0.06)	H	17.8 (1.2)
0419–487	3925 (303)	8.00 (0.00)	0.58 (0.00)	H	3.8 (0.5)
0423+120	6162 (127)	8.12 (0.07)	0.65 (0.04)	He	17.4 (0.8)
0426+588	7171 (181)	8.17 (0.03)	0.68 (0.02)	He	5.5 (0.1)
0433+270	5669 (107)	8.03 (0.03)	0.60 (0.02)	H	17.9 (0.4)
0435–088	6676 (157)	8.08 (0.04)	0.62 (0.02)	He	9.5 (0.2)
0503–174	5349 (119)	7.60 (0.16)	0.37 (0.07)	H	21.9 (1.9)
0548–001	6454 (137)	8.32 (0.04)	0.78 (0.03)	He	11.1 (0.3)
0552–041	5054 (70)	8.28 (0.02)	0.75 (0.01)	He	6.5 (0.1)
0553+053	5838 (114)	8.19 (0.04)	0.71 (0.03)	H	8.0 (0.2)
0644+025	7457 (181)	8.65 (0.12)	1.01 (0.07)	H	18.5 (1.9)
0655–390	6404 (168)	8.00 (0.00)	0.59 (0.00)	H	17.1 (0.7)
0657+320	5000 (143)	8.05 (0.03)	0.61 (0.02)	H	18.7 (0.3)
0708–670	5126 (91)	8.00 (0.00)	0.57 (0.00)	He	17.6 (0.6)
0727+482A	5043 (132)	7.91 (0.02)	0.53 (0.01)	H	11.1 (0.1)
0727+482B	5011 (143)	8.11 (0.02)	0.65 (0.01)	H	11.1 (0.1)
0728+642	4976 (149)	8.00 (0.00)	0.58 (0.00)	H	17.1 (1.0)

TABLE 2.2 – continued.

WD	T_{eff} (K)	$\log g$	M/M_{\odot}	Comp.	$D(\text{pc})$
0738–172	8012 (229)	8.20 (0.03)	0.70 (0.02)	He	8.9 (0.2)
0743–340	4622 (55)	8.09 (0.01)	0.62 (0.01)	He	15.2 (0.1)
0747+073A	4795 (61)	7.97 (0.02)	0.55 (0.01)	He	18.3 (0.2)
0747+073B	4398 (121)	7.81 (0.02)	0.47 (0.01)	H	18.3 (0.2)
0749+426	4791 (85)	8.00 (0.00)	0.57 (0.00)	He	25.9 (1.0)
0751–252	5103 (130)	7.93 (0.02)	0.54 (0.01)	H	18.2 (0.3)
0752–676	5782 (112)	8.21 (0.09)	0.72 (0.06)	H	7.1 (0.4)
0806–661	11,907 (525)	8.00 (0.00)	0.59 (0.00)	He	23.4 (1.0)
0810+489	5173 (97)	8.00 (0.00)	0.57 (0.00)	He	14.4 (0.5)
0816–310	7451 (245)	8.00 (0.00)	0.58 (0.00)	He	26.9 (1.2)
0821–669	5077 (133)	8.04 (0.02)	0.60 (0.01)	H	10.8 (0.1)
0827+328	7319 (177)	8.38 (0.11)	0.84 (0.07)	H	22.3 (1.9)
0839–327	8950 (224)	7.69 (0.14)	0.43 (0.07)	H	8.9 (0.8)
0840–136	5840 (131)	8.00 (0.00)	0.57 (0.00)	He	19.3 (0.7)
0843+358	9358 (427)	8.00 (0.00)	0.58 (0.00)	He	29.1 (1.7)
0856+331	10,374 (405)	8.82 (0.08)	1.10 (0.04)	He	20.5 (1.4)
0912+536	7228 (194)	8.28 (0.03)	0.75 (0.02)	He	10.3 (0.2)
0946+534	8786 (258)	8.44 (0.11)	0.86 (0.07)	He	23.0 (1.9)
0955+247	8701 (219)	8.26 (0.15)	0.76 (0.10)	H	24.4 (2.7)
1008+290	4031 (45)	7.93 (0.01)	0.52 (0.01)	He	14.8 (0.1)
1009–184	6336 (172)	8.18 (0.02)	0.69 (0.01)	He	18.0 (0.3)
1019+637	6831 (156)	7.97 (0.09)	0.57 (0.05)	H	16.3 (1.0)
1033+714	4745 (95)	8.00 (0.00)	0.57 (0.00)	He	19.7 (1.0)
1036–204	4847 (85)	8.00 (0.00)	0.57 (0.00)	He	15.5 (0.6)
1043–188	6063 (115)	8.09 (0.18)	0.63 (0.11)	He	17.6 (2.0)
1055–072	7483 (203)	8.42 (0.06)	0.84 (0.04)	He	12.2 (0.5)
1116–470	5938 (139)	8.00 (0.00)	0.57 (0.00)	He	18.3 (0.7)
1121+216	7534 (182)	8.19 (0.05)	0.71 (0.04)	H	13.4 (0.5)
1142–645	8537 (251)	8.24 (0.01)	0.73 (0.01)	He	4.6 (0.0)
1208+576	5930 (117)	7.95 (0.15)	0.56 (0.09)	H	20.4 (1.9)
1236–495	11,580 (471)	8.62 (0.19)	1.00 (0.11)	H	16.4 (2.6)
1257+037	5645 (109)	8.16 (0.09)	0.68 (0.06)	H	16.6 (1.0)
1309+853	5639 (137)	8.09 (0.26)	0.64 (0.16)	H	18.1 (3.1)
1310–472	4343 (100)	8.18 (0.05)	0.69 (0.04)	H	15.0 (0.5)
1315–781	5354 (105)	8.02 (0.03)	0.58 (0.02)	He	19.2 (0.3)
1334+039	5057 (132)	7.94 (0.05)	0.54 (0.03)	H	8.2 (0.2)
1339–340	5341 (127)	8.00 (0.00)	0.58 (0.00)	H	21.0 (0.9)
1344+106	7155 (168)	8.09 (0.11)	0.65 (0.07)	H	20.0 (1.5)
1345+238	4672 (154)	7.79 (0.05)	0.46 (0.03)	H	12.1 (0.3)
1444–174	4939 (68)	8.33 (0.08)	0.79 (0.06)	He	14.5 (0.8)

TABLE 2.2 – continued.

WD	T_{eff} (K)	$\log g$	M/M_{\odot}	Comp.	$D(\text{pc})$
1529+141	9130 (261)	8.00 (0.00)	0.60 (0.00)	H	63.6 (2.5)
1544–377	7446 (912)	6.99 (0.02)	0.20 (0.00)	H	15.2 (0.2)
1609+135	9117 (244)	8.74 (0.10)	1.07 (0.06)	H	18.3 (1.6)
1626+368	8978 (299)	8.14 (0.05)	0.67 (0.03)	He	15.9 (0.5)
1633+433	6701 (151)	8.13 (0.07)	0.67 (0.04)	H	15.1 (0.7)
1633+572	6298 (131)	8.16 (0.05)	0.67 (0.03)	He	14.5 (0.5)
1653+385	8432 (246)	8.00 (0.00)	0.60 (0.00)	H	40.2 (1.6)
1655+215	9207 (232)	7.86 (0.11)	0.52 (0.06)	H	23.3 (1.7)
1657+321	8480 (254)	8.00 (0.00)	0.60 (0.00)	H	66.0 (2.8)
1705+030	7102 (176)	8.35 (0.13)	0.80 (0.09)	He	17.5 (1.7)
1748+708	5425 (89)	8.30 (0.02)	0.77 (0.01)	He	6.1 (0.1)
1756+143	5404 (139)	8.00 (0.00)	0.58 (0.00)	H	21.9 (1.0)
1756+827	7361 (325)	7.99 (0.07)	0.59 (0.04)	H	15.6 (0.7)
1814+134	5279 (123)	8.00 (0.00)	0.58 (0.00)	H	15.3 (0.7)
1820+609	4813 (151)	7.82 (0.09)	0.47 (0.05)	H	12.8 (0.7)
1829+547	6340 (135)	8.50 (0.11)	0.90 (0.07)	He	15.0 (1.3)
1900+705	11,973 (956)	8.55 (0.04)	0.94 (0.02)	He	13.0 (0.4)
1917+386	6453 (142)	8.28 (0.06)	0.75 (0.04)	He	11.7 (0.5)
1917–077	11,314 (612)	8.05 (0.12)	0.61 (0.07)	He	11.2 (0.9)
1919+145	24,290 (3336)	8.69 (0.12)	1.05 (0.07)	H	19.8 (2.2)
1953–011	7960 (196)	8.22 (0.05)	0.73 (0.03)	H	11.4 (0.4)
2002–110	4743 (60)	8.26 (0.02)	0.73 (0.01)	He	17.3 (0.2)
2008–600	5159 (59)	7.93 (0.02)	0.53 (0.01)	H+He	16.6 (0.2)
2048+263	5234 (112)	7.31 (0.13)	0.26 (0.04)	H	20.1 (1.4)
2048–250	7697 (223)	8.00 (0.00)	0.59 (0.00)	H	27.8 (1.1)
2054–050	4563 (51)	7.80 (0.13)	0.45 (0.07)	He	17.7 (1.3)
2105–820	10,220 (286)	8.22 (0.21)	0.74 (0.14)	H	17.1 (2.6)
2138–332	8191 (273)	8.00 (0.00)	0.58 (0.00)	He	20.3 (0.9)
2140+207	8878 (283)	8.05 (0.06)	0.61 (0.04)	He	12.5 (0.5)
2154–512	5990 (126)	7.56 (0.08)	0.35 (0.03)	He	16.2 (0.7)
2211–392	6192 (131)	8.31 (0.07)	0.79 (0.04)	H	18.7 (0.9)
2215+368	4853 (84)	8.00 (0.00)	0.57 (0.00)	He	21.7 (0.8)
2226–754	4392 (112)	8.00 (0.00)	0.58 (0.00)	H	13.8 (0.7)
2226–755	4327 (102)	8.00 (0.00)	0.58 (0.00)	H	14.9 (0.7)
2246+223	10,368 (301)	8.57 (0.10)	0.96 (0.06)	H	19.0 (1.5)
2248+293	5633 (105)	7.53 (0.16)	0.35 (0.06)	H	20.9 (1.9)
2251–070	4532 (74)	8.32 (0.05)	0.78 (0.03)	He	8.1 (0.3)
2322+137	5865 (144)	8.00 (0.00)	0.59 (0.00)	H	19.4 (0.8)
2347+292	5857 (116)	7.82 (0.15)	0.48 (0.08)	H	21.5 (1.9)

TABLE 2.3 – RESULTS FROM SPECTROSCOPIC FITS

WD	T_{eff} (K)	$\log g$	$\log g_{\text{corrected}}$	M/M_{\odot}	M_V	$D(\text{pc})$
0008+423	7207 (107)	8.14 (0.07)	8.11 (0.07)	0.66 (0.05)	13.63	20.9 (2.9)
0009+501	6648 (105)	8.47 (0.10)	...	0.89 (0.06)	14.52	9.3 (1.3)
0101+048	8546 (123)	8.36 (0.06)	8.11 (0.06)	0.66 (0.03)	12.95	16.2 (2.2)
0135–052	7260 (104)	7.86 (0.05)	7.81 (0.05)	0.48 (0.03)	13.18	8.6 (1.2)
0141–675	6287 (101)	7.88 (0.11)	...	0.52 (0.06)	13.88	9.7 (1.3)
0148+467	14,004 (277)	8.04 (0.04)	...	0.63 (0.03)	11.45	15.8 (2.2)
0148+641	9015 (129)	8.41 (0.05)	8.12 (0.05)	0.67 (0.03)	12.76	17.7 (2.4)
0208+396	7360 (109)	8.16 (0.07)	8.09 (0.07)	0.65 (0.04)	13.52	15.8 (2.2)
0243–026	6811 (106)	8.08 (0.10)	8.16 (0.10)	0.69 (0.06)	13.93	21.0 (2.9)
0255–705	10,769 (159)	8.23 (0.05)	7.96 (0.05)	0.58 (0.03)	11.87	27.6 (3.8)
0310–688	16,804 (245)	8.09 (0.04)	...	0.67 (0.03)	11.21	10.9 (1.5)
0326–273	9325 (134)	7.93 (0.06)	7.63 (0.06)	0.41 (0.03)	11.92	26.0 (3.6)
0413–077	17,016 (255)	7.94 (0.04)	...	0.58 (0.03)	10.96	5.1 (0.7)
0419–487	6627 (127)	7.46 (0.19)	...	0.32 (0.07)	13.11	17.8 (2.5)
0457–004	11,409 (168)	8.98 (0.05)	8.75 (0.05)	1.07 (0.03)	13.03	28.4 (3.9)
0532+414	7757 (114)	8.12 (0.07)	7.97 (0.07)	0.57 (0.04)	13.13	21.1 (2.9)
0642–166	26,003 (379)	8.60 (0.04)	...	1.00 (0.03)	11.27	2.7 (0.4)
0644+025	7318 (111)	8.75 (0.08)	8.69 (0.08)	1.03 (0.05)	14.53	17.2 (2.4)
0644+375	22,045 (337)	8.11 (0.05)	...	0.69 (0.03)	10.77	18.3 (2.5)
0659–063	6628 (107)	8.36 (0.11)	...	0.82 (0.07)	14.35	16.4 (2.3)
0827+328	7520 (117)	8.66 (0.09)	8.56 (0.09)	0.95 (0.05)	14.18	20.4 (2.8)
0839–327	9229 (131)	7.96 (0.05)	7.66 (0.05)	0.42 (0.02)	12.01	9.5 (1.3)
0955+247	8640 (126)	8.39 (0.06)	8.13 (0.06)	0.68 (0.04)	12.95	26.5 (3.7)
1019+637	6965 (109)	8.29 (0.10)	8.32 (0.10)	0.80 (0.06)	14.09	13.3 (1.8)
1121+216	7479 (108)	8.22 (0.06)	8.12 (0.06)	0.67 (0.04)	13.50	13.8 (1.9)
1124+595	10,747 (156)	8.88 (0.05)	8.61 (0.05)	0.99 (0.03)	12.94	27.4 (3.8)
1134+300	22,153 (338)	8.59 (0.05)	...	0.99 (0.03)	11.55	15.3 (2.1)
1202–232	8785 (126)	8.35 (0.05)	8.07 (0.05)	0.64 (0.03)	12.79	10.0 (1.4)
1223–659	7629 (108)	7.92 (0.05)	7.80 (0.05)	0.48 (0.03)	12.97	15.9 (2.2)
1236–495	11,533 (167)	8.84 (0.04)	8.62 (0.04)	1.00 (0.03)	12.76	16.2 (2.2)
1242–105	8240 (120)	8.02 (0.07)	7.80 (0.07)	0.48 (0.03)	12.65	22.7 (3.1)
1310+583	10,682 (156)	8.39 (0.05)	8.11 (0.05)	0.67 (0.03)	12.12	24.8 (3.4)
1327–083	14,560 (235)	7.99 (0.04)	...	0.61 (0.03)	11.31	16.0 (2.2)
1344+106	7133 (108)	8.20 (0.08)	8.19 (0.08)	0.71 (0.05)	13.78	18.5 (2.6)
1350–090	9579 (136)	8.44 (0.05)	8.14 (0.05)	0.68 (0.03)	12.55	25.1 (3.5)
1425–811	12,330 (182)	8.17 (0.04)	8.01 (0.04)	0.61 (0.03)	11.62	26.7 (3.7)
1538+333	8893 (127)	8.37 (0.05)	8.09 (0.05)	0.65 (0.03)	12.76	28.4 (3.9)
1544–377	10,611 (151)	8.20 (0.04)	7.92 (0.04)	0.55 (0.03)	11.85	16.7 (2.3)
1609+135	9369 (134)	8.73 (0.05)	8.43 (0.05)	0.87 (0.03)	13.11	25.1 (3.5)
1620–391	25,940 (370)	7.99 (0.04)	...	0.63 (0.02)	10.26	13.9 (1.9)

TABLE 2.3 – continued.

WD	T_{eff} (K)	$\log g$	$\log g_{\text{corrected}}$	M/M_{\odot}	M_V	$D(\text{pc})$
1632+177	10,225 (145)	8.04 (0.04)	7.74 (0.04)	0.46 (0.02)	11.73	18.6 (2.6)
1633+433	6550 (113)	7.78 (0.15)	...	0.47 (0.08)	13.57	17.9 (2.5)
1647+591	12,738 (201)	8.38 (0.05)	8.25 (0.05)	0.76 (0.03)	11.91	11.6 (1.6)
1655+215	9374 (134)	8.27 (0.05)	7.97 (0.05)	0.58 (0.03)	12.38	22.3 (3.1)
1729+371	9591 (171)	9.01 (0.11)	8.71 (0.11)	1.05 (0.07)	13.54	34.5 (4.8)
1756+827	7396 (110)	8.09 (0.08)	8.01 (0.08)	0.60 (0.05)	13.38	15.5 (2.1)
1919+145	15,278 (247)	8.21 (0.04)	...	0.74 (0.03)	11.55	19.3 (2.7)
1935+276	12,625 (194)	8.13 (0.05)	7.99 (0.05)	0.60 (0.03)	11.55	21.4 (3.0)
1953–011	7863 (115)	8.40 (0.06)	8.23 (0.06)	0.74 (0.04)	13.47	11.1 (1.5)
2007–303	16,117 (234)	7.99 (0.04)	...	0.61 (0.03)	11.13	16.2 (2.2)
2032+248	20,367 (312)	7.97 (0.05)	...	0.61 (0.03)	10.70	14.6 (2.0)
2039–202	20,016 (293)	7.96 (0.04)	...	0.60 (0.02)	10.71	21.1 (2.9)
2039–682	17,050 (280)	8.56 (0.05)	...	0.96 (0.03)	11.94	20.1 (2.8)
2040–392	11,301 (163)	8.26 (0.04)	8.02 (0.04)	0.61 (0.03)	11.82	24.2 (3.3)
2047+372	14,711 (285)	8.31 (0.04)	...	0.81 (0.03)	11.78	17.0 (2.3)
2105–820	10,600 (153)	8.24 (0.05)	7.96 (0.05)	0.58 (0.03)	11.92	21.8 (3.0)
2115–560	9840 (141)	8.21 (0.05)	7.91 (0.05)	0.55 (0.03)	12.10	27.3 (3.8)
2117+539	14,678 (239)	7.91 (0.05)	...	0.56 (0.03)	11.18	17.0 (2.3)
2126+734	16,167 (237)	7.99 (0.04)	...	0.61 (0.03)	11.12	21.9 (3.0)
2151–015	9194 (133)	8.28 (0.06)	7.98 (0.06)	0.59 (0.03)	12.48	24.3 (3.4)
2159–754	8934 (132)	8.94 (0.06)	8.65 (0.06)	1.01 (0.04)	13.70	18.7 (2.6)
2246+223	10,722 (155)	8.89 (0.05)	8.61 (0.05)	0.99 (0.03)	12.95	19.4 (2.7)
2326+049	12,203 (187)	8.22 (0.05)	8.05 (0.05)	0.64 (0.03)	11.69	18.7 (2.6)
2336–079	11,272 (165)	8.18 (0.05)	7.94 (0.05)	0.57 (0.03)	11.71	25.6 (3.5)
2341+322	13,121 (197)	8.02 (0.04)	7.92 (0.04)	0.57 (0.03)	11.40	20.1 (2.8)
2351–335	8846 (128)	8.31 (0.06)	8.03 (0.06)	0.61 (0.03)	12.70	22.1 (3.1)
2359–434	8572 (122)	8.50 (0.05)	8.24 (0.05)	0.75 (0.03)	13.14	9.1 (1.3)

TABLE 2.4 – ADOPTED ATMOSPHERIC PARAMETERS OF NEARBY CANDIDATES

WD	T_{eff} (K)	$\log g$	M/M_{\odot}	Comp.	$\log L/L_{\odot}$	$D(\text{pc})$	$\log \tau$	Notes
0000–345	6297 (137)	8.31 (0.17)	0.77 (0.11)	He	−3.83	13.2 (1.6)	9.61	2
0008+423	7207 (107)	8.11 (0.07)	0.66 (0.05)	H	−3.47	20.9 (2.9)	9.21	1
0009+501	6595 (146)	8.22 (0.06)	0.73 (0.04)	H	−3.69	11.0 (0.5)	9.45	2
0011–134	6065 (122)	8.19 (0.11)	0.71 (0.07)	H	−3.82	19.5 (1.5)	9.54	2
0011–721	6393 (169)	8.00 (0.00)	0.59 (0.00)	H	−3.61	17.5 (0.7)	9.28	2
0038–226	5535 (100)	7.95 (0.17)	0.54 (0.10)	H+He	−3.85	9.9 (1.0)	9.53	2
0046+051	6296 (256)	8.22 (0.03)	0.71 (0.02)	He	−3.77	4.4 (0.1)	9.54	2
0101+048	8116 (193)	7.53 (0.14)	0.36 (0.05)	H	−2.95	21.3 (1.7)	8.79	2
0108+277	6485 (179)	8.00 (0.00)	0.59 (0.00)	H	−3.59	28.1 (1.2)	9.26	2
0115+159	9086 (302)	8.19 (0.07)	0.70 (0.04)	He	−3.12	15.4 (0.7)	9.03	2
0121–429	6370 (171)	7.65 (0.03)	0.40 (0.01)	H	−3.43	18.3 (0.3)	9.09	2
0123–262	7281 (191)	8.00 (0.00)	0.58 (0.00)	He	−3.40	21.7 (0.8)	9.18	2
0135–052	7182 (162)	7.18 (0.06)	0.24 (0.01)	H	−2.98	12.3 (0.4)	8.81	2
0141–675	6287 (101)	7.88 (0.11)	0.52 (0.06)	H	−3.58	9.7 (1.3)	9.22	1
0148+467	14,004 (277)	8.04 (0.04)	0.63 (0.03)	H	−2.26	15.8 (2.2)	8.41	1
0148+641	9015 (129)	8.12 (0.05)	0.67 (0.03)	H	−3.08	17.7 (2.4)	8.97	1
0208+396	7357 (173)	8.00 (0.09)	0.59 (0.05)	H	−3.37	16.7 (1.0)	9.13	2
0213+427	5657 (167)	8.12 (0.12)	0.66 (0.08)	H	−3.90	19.9 (1.6)	9.57	2
0230–144	5530 (129)	8.11 (0.09)	0.65 (0.06)	H	−3.93	15.6 (1.0)	9.61	2
0233–242	5372 (107)	8.00 (0.00)	0.57 (0.00)	He	−3.93	15.9 (0.6)	9.65	2
0236+259	5315 (130)	8.00 (0.00)	0.58 (0.00)	H	−3.94	19.3 (0.9)	9.61	2
0243–026	6868 (158)	8.17 (0.15)	0.70 (0.10)	H	−3.59	21.2 (2.3)	9.34	2
0245+541	5309 (128)	8.27 (0.05)	0.75 (0.03)	H	−4.10	10.4 (0.3)	9.83	2
0255–705	10,769 (159)	7.96 (0.05)	0.58 (0.03)	H	−2.68	27.6 (3.8)	8.67	1
0310–688	16,804 (245)	8.09 (0.04)	0.67 (0.03)	H	−1.97	10.9 (1.5)	8.20	1
0322–019	5235 (130)	8.05 (0.08)	0.61 (0.05)	H	−3.99	16.8 (0.9)	9.71	2
0326–273	7247 (200)	7.51 (0.40)	0.35 (0.15)	H	−3.14	17.4 (4.3)	8.90	2
0341+182	6509 (137)	7.99 (0.10)	0.57 (0.06)	He	−3.59	19.0 (1.0)	9.29	2
0344+014	5058 (92)	8.00 (0.00)	0.57 (0.00)	He	−4.03	19.5 (0.7)	9.76	2
0357+081	5536 (129)	8.02 (0.10)	0.60 (0.06)	H	−3.88	17.8 (1.2)	9.51	2
0413–077	17,016 (255)	7.94 (0.04)	0.58 (0.03)	H	−1.86	5.1 (0.7)	8.06	1
0419–487	6627 (127)	7.46 (0.19)	0.32 (0.07)	H	−3.27	17.8 (2.5)	8.98	1
0423+120	6162 (127)	8.12 (0.07)	0.65 (0.04)	He	−3.75	17.4 (0.8)	9.48	2
0426+588	7171 (181)	8.17 (0.03)	0.68 (0.02)	He	−3.52	5.5 (0.1)	9.30	2
0433+270	5669 (107)	8.03 (0.03)	0.60 (0.02)	H	−3.84	17.9 (0.4)	9.47	2
0435–088	6302 (117)	7.93 (0.04)	0.53 (0.02)	He	−3.61	9.5 (0.2)	9.28	2
0457–004	11,409 (168)	8.75 (0.05)	1.07 (0.03)	H	−3.10	28.4 (3.9)	9.21	1
0503–174	5349 (119)	7.60 (0.16)	0.37 (0.07)	H	−3.72	21.9 (1.9)	9.26	2
0532+414	7757 (114)	7.97 (0.07)	0.57 (0.04)	H	−3.25	21.1 (2.9)	9.05	1
0548–001	6069 (105)	8.18 (0.05)	0.69 (0.03)	He	−3.82	11.1 (0.3)	9.58	2

TABLE 2.4 – continued.

WD	T_{eff} (K)	$\log g$	M/M_{\odot}	Comp.	$\log L/L_{\odot}$	$D(\text{pc})$	$\log \tau$	Notes
0552–041	4313 (48)	7.83 (0.02)	0.47 (0.01)	He	−4.23	6.5 (0.1)	9.75	2
0553+053	5838 (114)	8.19 (0.04)	0.71 (0.03)	H	−3.89	8.0 (0.2)	9.60	2
0642–166	26,003 (379)	8.60 (0.04)	1.00 (0.03)	H	−1.55	2.7 (0.4)	8.02	1
0644+025	7457 (181)	8.65 (0.12)	1.01 (0.07)	H	−3.76	18.5 (1.9)	9.57	2
0644+375	22,045 (337)	8.11 (0.05)	0.69 (0.03)	H	−1.50	18.3 (2.5)	7.77	1
0655–390	6404 (168)	8.00 (0.00)	0.59 (0.00)	H	−3.61	17.1 (0.7)	9.28	2
0657+320	5000 (143)	8.05 (0.03)	0.61 (0.02)	H	−4.08	18.7 (0.3)	9.80	2
0659–063	6628 (107)	8.36 (0.11)	0.82 (0.07)	H	−3.77	16.4 (2.3)	9.57	1
0708–670	5126 (91)	8.00 (0.00)	0.57 (0.00)	He	−4.01	17.6 (0.6)	9.74	2
0727+482A	5043 (132)	7.91 (0.02)	0.53 (0.01)	H	−3.98	11.1 (0.1)	9.64	2
0727+482B	5011 (143)	8.11 (0.02)	0.65 (0.01)	H	−4.10	11.1 (0.1)	9.83	2
0728+642	4976 (149)	8.00 (0.00)	0.58 (0.00)	H	−4.06	17.1 (1.0)	9.76	2
0736+053	7267 (264)	7.91 (0.01)	0.52 (0.00)	He	−3.35	3.5 (0.0)	9.11	2
0738–172	7679 (199)	8.10 (0.04)	0.64 (0.02)	He	−3.36	8.9 (0.2)	9.17	2
0743–340	4622 (55)	8.09 (0.01)	0.62 (0.01)	He	−4.24	15.2 (0.1)	9.87	2
0747+073A	4795 (61)	7.97 (0.02)	0.55 (0.01)	He	−4.11	18.3 (0.2)	9.79	2
0747+073B	4398 (121)	7.81 (0.02)	0.47 (0.01)	H	−4.18	18.3 (0.2)	9.77	2
0749+426	4791 (85)	8.00 (0.00)	0.57 (0.00)	He	−4.13	25.9 (1.0)	9.81	2
0751–252	5103 (130)	7.93 (0.02)	0.54 (0.01)	H	−3.97	18.2 (0.3)	9.63	2
0752–676	5782 (112)	8.21 (0.09)	0.72 (0.06)	H	−3.91	7.1 (0.4)	9.62	2
0806–661	11,907 (525)	8.00 (0.00)	0.59 (0.00)	He	−2.54	23.4 (1.0)	8.62	2
0810+489	5173 (97)	8.00 (0.00)	0.57 (0.00)	He	−4.00	14.4 (0.5)	9.73	2
0816–310	6438 (274)	8.00 (0.00)	0.57 (0.00)	He	−3.61	22.3 (1.2)	9.31	2
0821–669	5077 (133)	8.04 (0.02)	0.60 (0.01)	H	−4.04	10.8 (0.1)	9.76	2
0827+328	7319 (177)	8.38 (0.11)	0.84 (0.07)	H	−3.61	22.3 (1.9)	9.47	2
0839–327	8950 (224)	7.69 (0.14)	0.43 (0.07)	H	−2.85	8.9 (0.8)	8.74	2
0840–136	5840 (131)	8.00 (0.00)	0.57 (0.00)	He	−3.78	19.3 (0.7)	9.45	2
0843+358	8602 (499)	8.00 (0.00)	0.58 (0.00)	He	−3.10	26.2 (1.6)	8.99	2
0856+331	9930 (245)	8.74 (0.08)	1.05 (0.05)	He	−3.34	20.5 (1.3)	9.33	2
0912+536	7228 (194)	8.28 (0.03)	0.75 (0.02)	He	−3.57	10.3 (0.2)	9.39	2
0946+534	8112 (240)	8.27 (0.12)	0.75 (0.08)	He	−3.37	23.0 (1.7)	9.22	2
0955+247	8701 (219)	8.26 (0.15)	0.76 (0.10)	H	−3.23	24.4 (2.7)	9.10	2
1008+290	4031 (45)	7.93 (0.01)	0.52 (0.01)	He	−4.39	14.8 (0.1)	9.87	2
1009–184	6336 (172)	8.18 (0.02)	0.69 (0.01)	He	−3.74	18.0 (0.3)	9.50	2
1019+637	6831 (156)	7.97 (0.09)	0.57 (0.05)	H	−3.48	16.3 (1.0)	9.19	2
1033+714	4745 (95)	8.00 (0.00)	0.57 (0.00)	He	−4.15	19.7 (1.0)	9.82	2
1036–204	4847 (85)	8.00 (0.00)	0.57 (0.00)	He	−4.11	15.5 (0.6)	9.80	2
1043–188	6063 (115)	8.09 (0.18)	0.63 (0.11)	He	−3.77	17.6 (2.0)	9.48	2
1055–072	7483 (203)	8.42 (0.06)	0.84 (0.04)	He	−3.60	12.2 (0.5)	9.47	2
1116–470	5938 (139)	8.00 (0.00)	0.57 (0.00)	He	−3.75	18.3 (0.7)	9.42	2

TABLE 2.4 – continued.

WD	T_{eff} (K)	$\log g$	M/M_{\odot}	Comp.	$\log L/L_{\odot}$	$D(\text{pc})$	$\log \tau$	Notes
1121+216	7534 (182)	8.19 (0.05)	0.71 (0.04)	H	-3.44	13.4 (0.5)	9.23	2
1124+595	10,747 (156)	8.61 (0.05)	0.99 (0.03)	H	-3.10	27.4 (3.8)	9.18	1
1134+300	22,153 (338)	8.59 (0.05)	0.99 (0.03)	H	-1.82	15.3 (2.1)	8.23	1
1142-645	7918 (215)	8.07 (0.01)	0.62 (0.01)	He	-3.29	4.6 (0.0)	9.12	2
1202-232	8785 (126)	8.07 (0.05)	0.64 (0.03)	H	-3.10	10.0 (1.4)	8.97	1
1208+576	5930 (117)	7.95 (0.15)	0.56 (0.09)	H	-3.72	20.4 (1.9)	9.32	2
1223-659	7629 (108)	7.80 (0.05)	0.48 (0.03)	H	-3.19	15.9 (2.2)	8.97	1
1236-495	11,580 (471)	8.62 (0.19)	1.00 (0.11)	H	-2.97	16.4 (2.6)	9.08	2
1242-105	8240 (120)	7.80 (0.07)	0.48 (0.03)	H	-3.06	22.7 (3.1)	8.88	1
1257+037	5645 (109)	8.16 (0.09)	0.68 (0.06)	H	-3.92	16.6 (1.0)	9.62	2
1309+853	5639 (137)	8.09 (0.26)	0.64 (0.16)	H	-3.89	18.1 (3.1)	9.55	2
1310+583	10,682 (156)	8.11 (0.05)	0.67 (0.03)	H	-2.78	24.8 (3.4)	8.77	1
1310-472	4343 (100)	8.18 (0.05)	0.69 (0.04)	H	-4.40	15.0 (0.5)	9.97	2
1315-781	5354 (105)	8.02 (0.03)	0.58 (0.02)	He	-3.95	19.2 (0.3)	9.68	2
1327-083	14,560 (235)	7.99 (0.04)	0.61 (0.03)	H	-2.16	16.0 (2.2)	8.33	1
1334+039	5057 (132)	7.94 (0.05)	0.54 (0.03)	H	-4.00	8.2 (0.2)	9.67	2
1339-340	5341 (127)	8.00 (0.00)	0.58 (0.00)	H	-3.93	21.0 (0.9)	9.59	2
1344+106	7155 (168)	8.09 (0.11)	0.65 (0.07)	H	-3.47	20.0 (1.5)	9.21	2
1345+238	4672 (154)	7.79 (0.05)	0.46 (0.03)	H	-4.06	12.1 (0.3)	9.67	2
1350-090	9579 (136)	8.14 (0.05)	0.68 (0.03)	H	-2.98	25.1 (3.5)	8.92	1
1425-811	12,330 (182)	8.01 (0.04)	0.61 (0.03)	H	-2.47	26.7 (3.7)	8.55	1
1444-174	4939 (68)	8.33 (0.08)	0.79 (0.06)	He	-4.27	14.5 (0.8)	9.86	2
1529+141	9130 (261)	8.00 (0.00)	0.60 (0.00)	H	-2.99	63.6 (2.5)	8.88	2
1538+333	8893 (127)	8.09 (0.05)	0.65 (0.03)	H	-3.08	28.4 (3.9)	8.97	1
1544-377	10,611 (151)	7.92 (0.04)	0.55 (0.03)	H	-2.68	16.7 (2.3)	8.67	1
1609+135	9117 (244)	8.74 (0.10)	1.07 (0.06)	H	-3.48	18.3 (1.6)	9.43	2
1620-391	25,940 (370)	7.99 (0.04)	0.63 (0.02)	H	-1.14	13.9 (1.9)	7.25	1
1626+368	8978 (299)	8.14 (0.05)	0.67 (0.03)	He	-3.11	15.9 (0.5)	9.02	2
1632+177	10,225 (145)	7.74 (0.04)	0.46 (0.02)	H	-2.65	18.6 (2.6)	8.62	1
1633+433	6701 (151)	8.13 (0.07)	0.67 (0.04)	H	-3.61	15.1 (0.7)	9.34	2
1633+572	6298 (131)	8.16 (0.05)	0.67 (0.03)	He	-3.74	14.5 (0.5)	9.49	2
1647+591	12,738 (201)	8.25 (0.05)	0.76 (0.03)	H	-2.56	11.6 (1.6)	8.66	1
1653+385	7561 (314)	8.00 (0.00)	0.58 (0.00)	He	-3.33	34.0 (1.6)	9.14	2
1655+215	9207 (232)	7.86 (0.11)	0.52 (0.06)	H	-2.90	23.3 (1.7)	8.80	2
1657+321	8480 (254)	8.00 (0.00)	0.60 (0.00)	H	-3.12	66.0 (2.8)	8.96	2
1705+030	7102 (176)	8.35 (0.13)	0.80 (0.09)	He	-3.65	17.5 (1.7)	9.48	2
1729+371	10,560 (182)	7.82 (0.11)	0.50 (0.06)	H	-2.63	79.5 (11.0)	8.62	1
1748+708	5173 (89)	8.21 (0.02)	0.70 (0.01)	He	-4.11	6.1 (0.1)	9.81	2
1756+143	5404 (139)	8.00 (0.00)	0.58 (0.00)	H	-3.91	21.9 (1.0)	9.55	2
1756+827	7361 (325)	7.99 (0.07)	0.59 (0.04)	H	-3.36	15.6 (0.7)	9.12	2

TABLE 2.4 – continued.

WD	T_{eff} (K)	$\log g$	M/M_{\odot}	Comp.	$\log L/L_{\odot}$	$D(\text{pc})$	$\log \tau$	Notes
1814+134	5279 (123)	8.00 (0.00)	0.58 (0.00)	H	-3.95	15.3 (0.7)	9.63	2
1820+609	4813 (151)	7.82 (0.09)	0.47 (0.05)	H	-4.02	12.8 (0.7)	9.65	2
1829+547	6340 (135)	8.50 (0.11)	0.90 (0.07)	He	-3.94	15.0 (1.3)	9.67	2
1900+705	11,973 (956)	8.55 (0.04)	0.94 (0.02)	He	-2.87	13.0 (0.4)	8.96	2
1917+386	6453 (142)	8.28 (0.06)	0.75 (0.04)	He	-3.77	11.7 (0.5)	9.55	2
1917-077	11,314 (612)	8.05 (0.12)	0.61 (0.07)	He	-2.65	11.2 (0.9)	8.71	2
1919+145	15,278 (247)	8.21 (0.04)	0.74 (0.03)	H	-2.21	19.3 (2.7)	8.42	1
1935+276	12,625 (194)	7.99 (0.05)	0.60 (0.03)	H	-2.42	21.4 (3.0)	8.51	1
1953-011	7960 (196)	8.22 (0.05)	0.73 (0.03)	H	-3.36	11.4 (0.4)	9.19	2
2002-110	4743 (60)	8.26 (0.02)	0.73 (0.01)	He	-4.29	17.3 (0.2)	9.86	2
2007-303	16,117 (234)	7.99 (0.04)	0.61 (0.03)	H	-1.98	16.2 (2.2)	8.19	1
2008-600	5159 (59)	7.93 (0.02)	0.53 (0.01)	H+He	-3.96	16.6 (0.2)	9.67	2
2032+248	20,367 (312)	7.97 (0.05)	0.61 (0.03)	H	-1.56	14.6 (2.0)	7.77	1
2039-202	20,016 (293)	7.96 (0.04)	0.60 (0.02)	H	-1.58	21.1 (2.9)	7.80	1
2039-682	17,050 (280)	8.56 (0.05)	0.96 (0.03)	H	-2.25	20.1 (2.8)	8.54	1
2040-392	11,301 (163)	8.02 (0.04)	0.61 (0.03)	H	-2.62	24.2 (3.3)	8.65	1
2047+372	14,711 (285)	8.31 (0.04)	0.81 (0.03)	H	-2.34	17.0 (2.3)	8.54	1
2048+263	5234 (112)	7.31 (0.13)	0.26 (0.04)	H	-3.62	20.1 (1.4)	9.17	2
2048-250	7697 (223)	8.00 (0.00)	0.59 (0.00)	H	-3.29	27.8 (1.1)	9.08	2
2054-050	4563 (51)	7.80 (0.13)	0.45 (0.07)	He	-4.11	17.7 (1.3)	9.68	2
2105-820	10,220 (286)	8.22 (0.21)	0.74 (0.14)	H	-2.92	17.1 (2.6)	8.90	2
2115-560	9840 (141)	7.91 (0.05)	0.55 (0.03)	H	-2.80	27.3 (3.8)	8.75	1
2117+539	14,678 (239)	7.91 (0.05)	0.56 (0.03)	H	-2.10	17.0 (2.3)	8.26	1
2126+734	16,167 (237)	7.99 (0.04)	0.61 (0.03)	H	-1.98	21.9 (3.0)	8.18	1
2138-332	8191 (273)	8.00 (0.00)	0.58 (0.00)	He	-3.19	20.3 (0.9)	9.05	2
2140+207	8210 (252)	7.85 (0.07)	0.49 (0.04)	He	-3.11	12.5 (0.5)	8.93	2
2151-015	9194 (133)	7.98 (0.06)	0.59 (0.03)	H	-2.97	24.3 (3.4)	8.87	1
2154-512	6375 (74)	7.71 (0.08)	0.42 (0.04)	He	-3.48	16.1 (0.6)	9.14	2
2159-754	8934 (132)	8.65 (0.06)	1.01 (0.04)	H	-3.45	18.7 (2.6)	9.41	1
2211-392	6192 (131)	8.31 (0.07)	0.79 (0.04)	H	-3.86	18.7 (0.9)	9.61	2
2215+368	4853 (84)	8.00 (0.00)	0.57 (0.00)	He	-4.11	21.7 (0.8)	9.80	2
2226-754	4392 (112)	8.00 (0.00)	0.58 (0.00)	H	-4.27	13.8 (0.7)	9.90	2
2226-755	4327 (102)	8.00 (0.00)	0.58 (0.00)	H	-4.30	14.9 (0.7)	9.91	2
2246+223	10,368 (301)	8.57 (0.10)	0.96 (0.06)	H	-3.13	19.0 (1.5)	9.18	2
2248+293	5633 (105)	7.53 (0.16)	0.35 (0.06)	H	-3.59	20.9 (1.9)	9.16	2
2251-070	4532 (74)	8.32 (0.05)	0.78 (0.03)	He	-4.41	8.1 (0.3)	9.89	2
2322+137	5865 (144)	8.00 (0.00)	0.59 (0.00)	H	-3.77	19.4 (0.8)	9.38	2
2326+049	12,203 (187)	8.05 (0.05)	0.64 (0.03)	H	-2.51	18.7 (2.6)	8.58	1
2336-079	11,272 (165)	7.94 (0.05)	0.57 (0.03)	H	-2.58	25.6 (3.5)	8.61	1
2341+322	13,121 (197)	7.92 (0.04)	0.57 (0.03)	H	-2.31	20.1 (2.8)	8.42	1

TABLE 2.4 – continued.

WD	T_{eff} (K)	$\log g$	M/M_{\odot}	Comp.	$\log L/L_{\odot}$	$D(\text{pc})$	$\log \tau$	Notes
2347+292	5857 (116)	7.82 (0.15)	0.48 (0.08)	H	-3.67	21.5 (1.9)	9.27	2
2351-335	8846 (128)	8.03 (0.06)	0.61 (0.03)	H	-3.06	22.1 (3.1)	8.94	1
2359-434	8572 (122)	8.24 (0.05)	0.75 (0.03)	H	-3.24	9.1 (1.3)	9.11	1

Note. – (1) Spectroscopic technique; (2) Photometric technique.

2.10 Figures

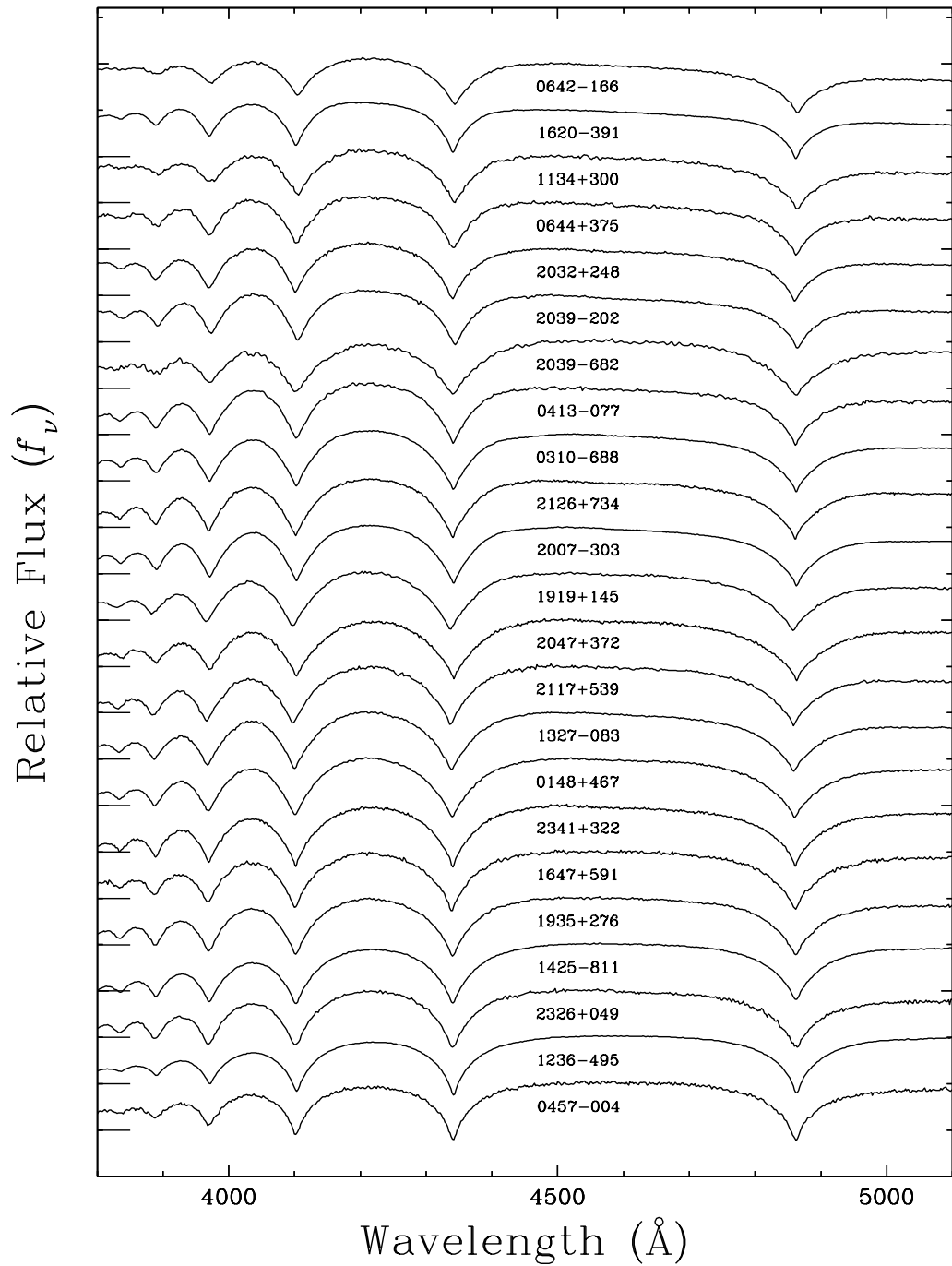


FIGURE 2.1 – (a) Our blue spectroscopic observations of DA and DAZ stars. Spectra are shown in order of decreasing T_{eff} , from top to bottom. All spectra are normalized at 4500 Å and are offset from each other by a factor of 0.5.

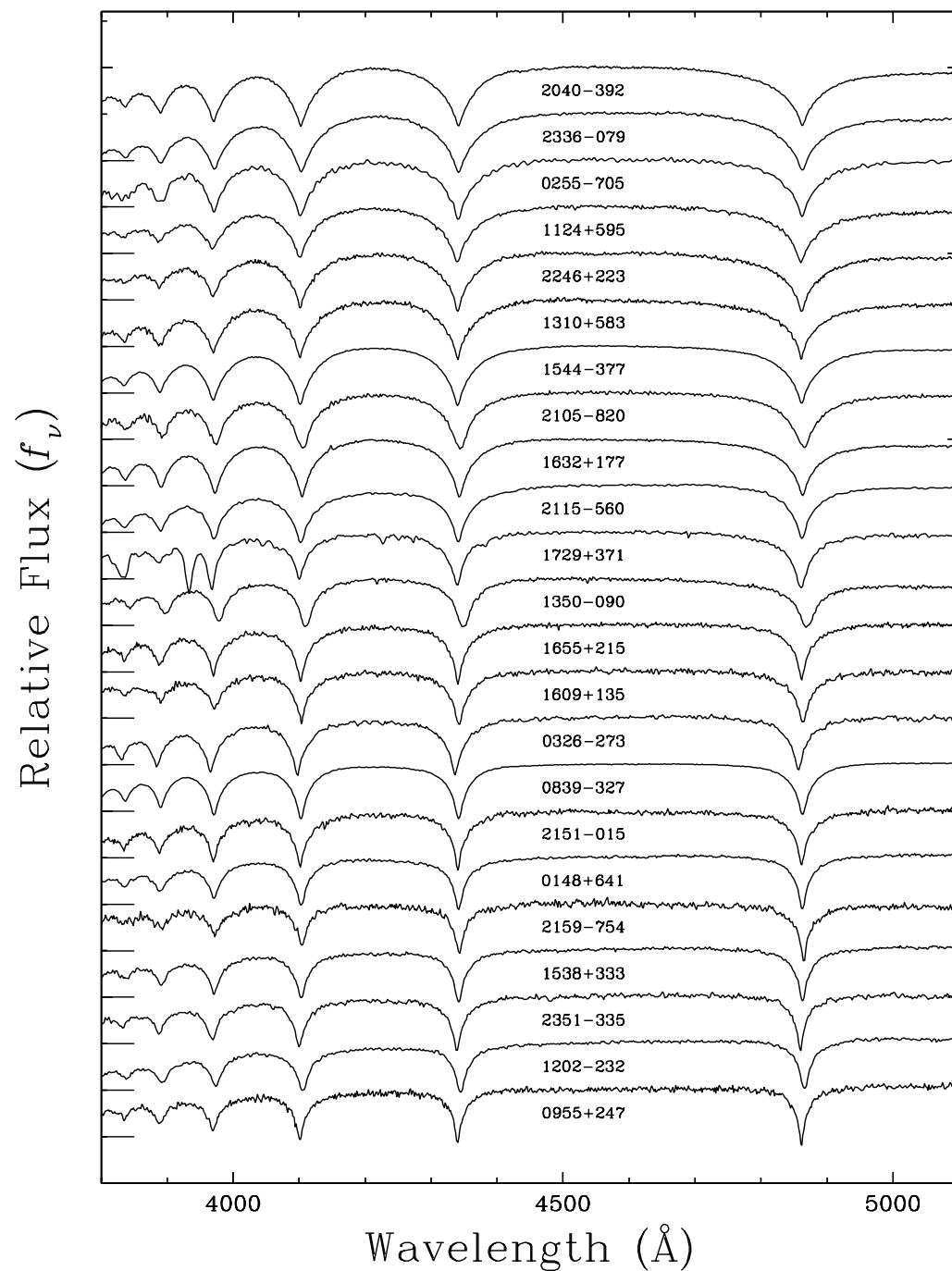


FIGURE 2.1 – (b) Optical spectra of DA and DAZ white dwarfs - continued.

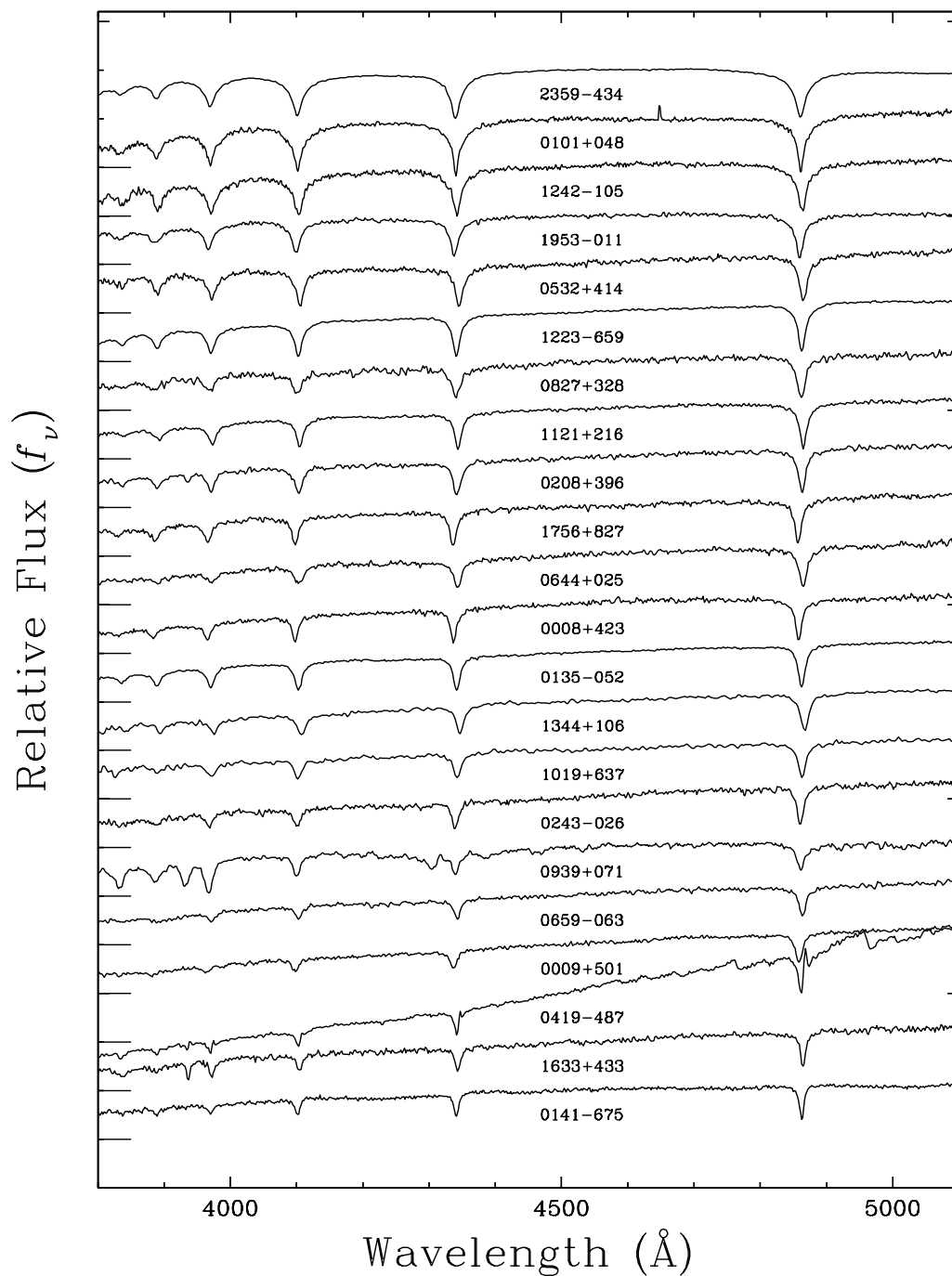


FIGURE 2.1 – (c) Optical spectra of DA and DAZ white dwarfs - continued.

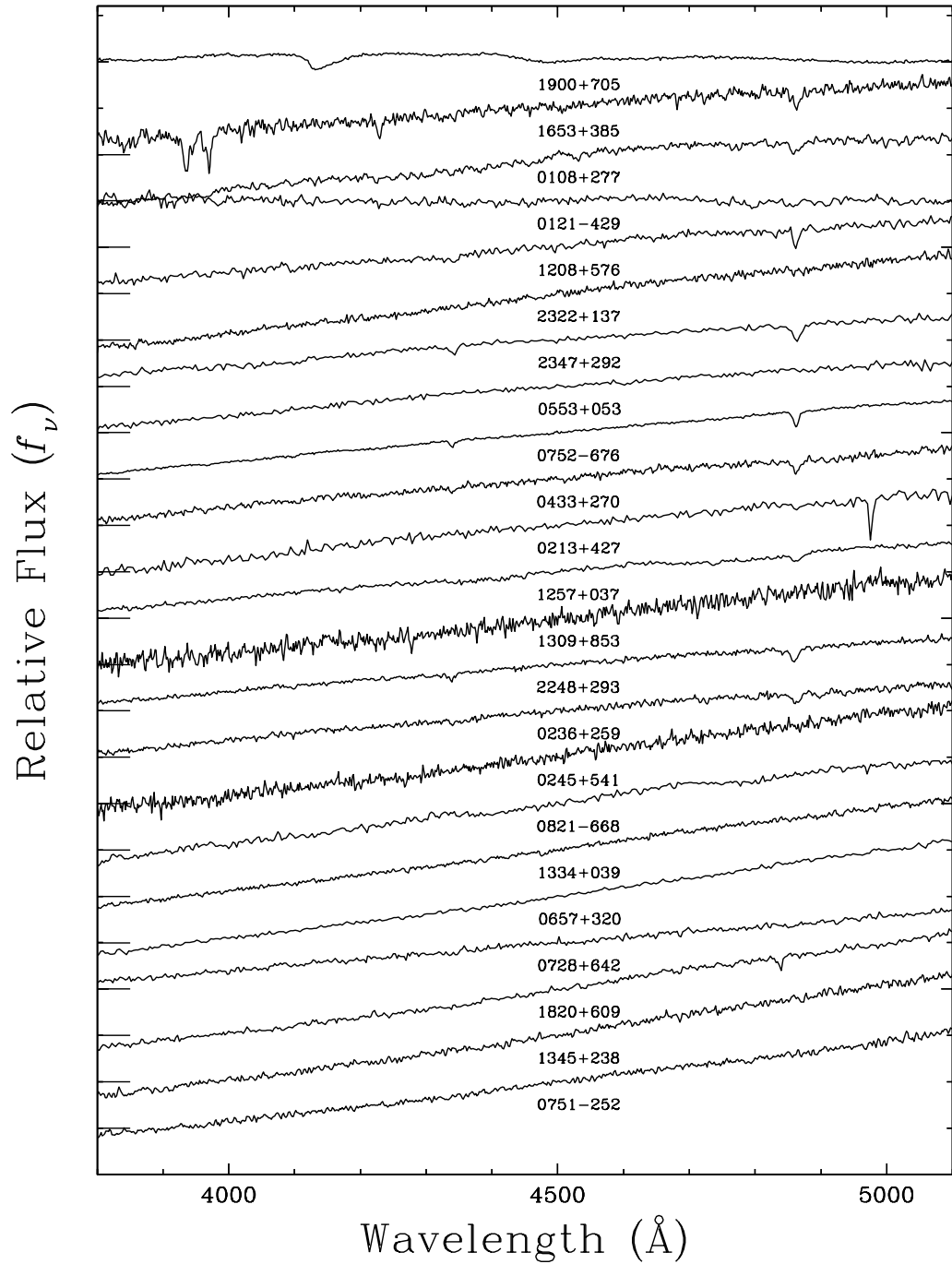


FIGURE 2.2 – Blue coverage of the DA and DAZ spectra of objects too cool to be analyzed using line profile fitting techniques. All spectra are normalized at 4500 Å and are offset from each other by a factor of 0.5. They are shown in order of decreasing T_{eff} from top to bottom.

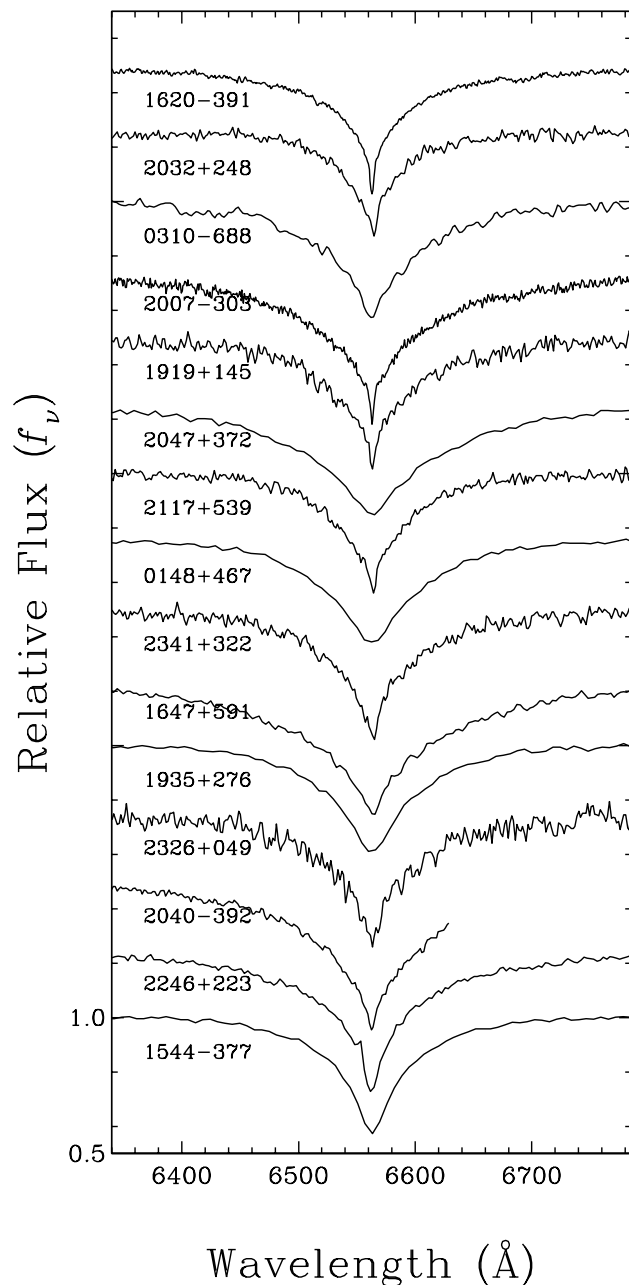


FIGURE 2.3 – (a) White dwarfs in our sample whose spectra show H α . All spectra are normalized to a continuum set to unity, and offset vertically from each other by a factor of 0.3, in order of decreasing equivalent width from top to bottom.

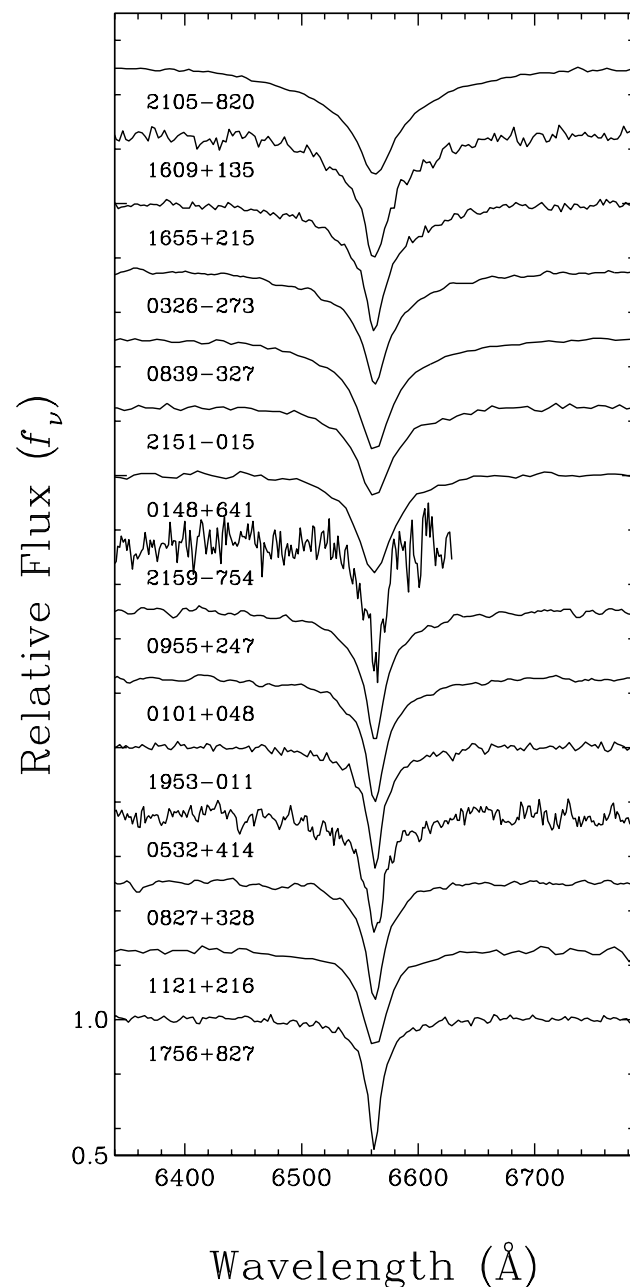


FIGURE 2.3 – (b) Optical spectra of halpha from DA and DAZ white dwarfs - continued.

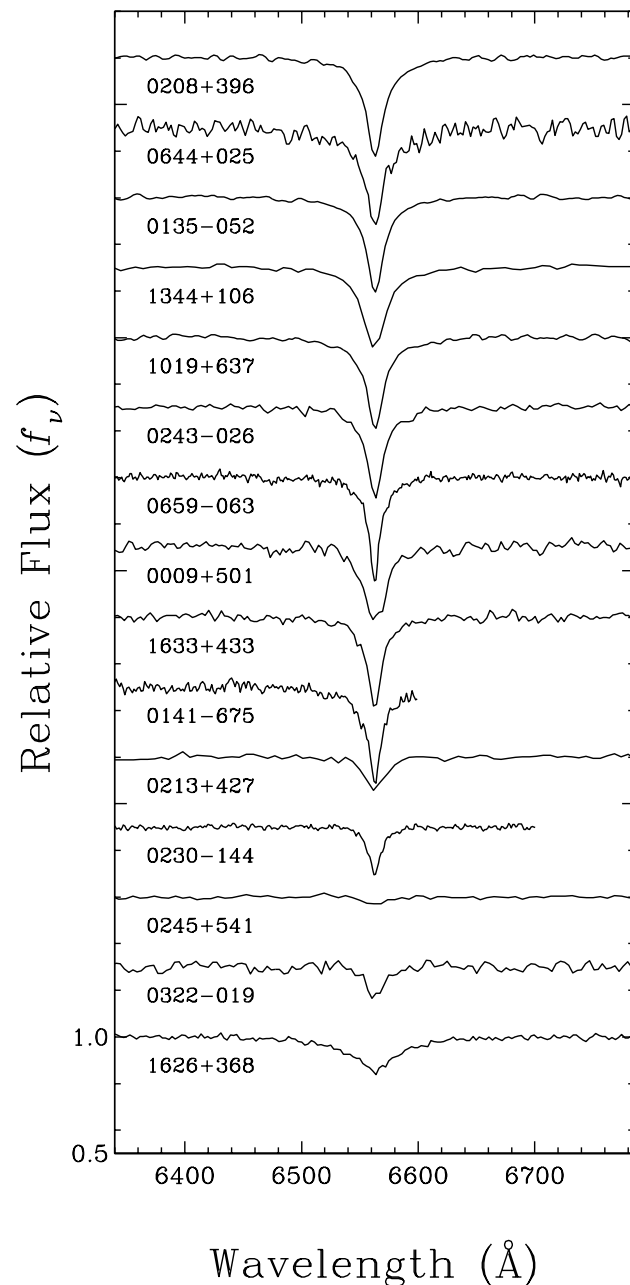


FIGURE 2.3 – (c) Optical spectra of halpha from DA and DAZ white dwarfs - continued.

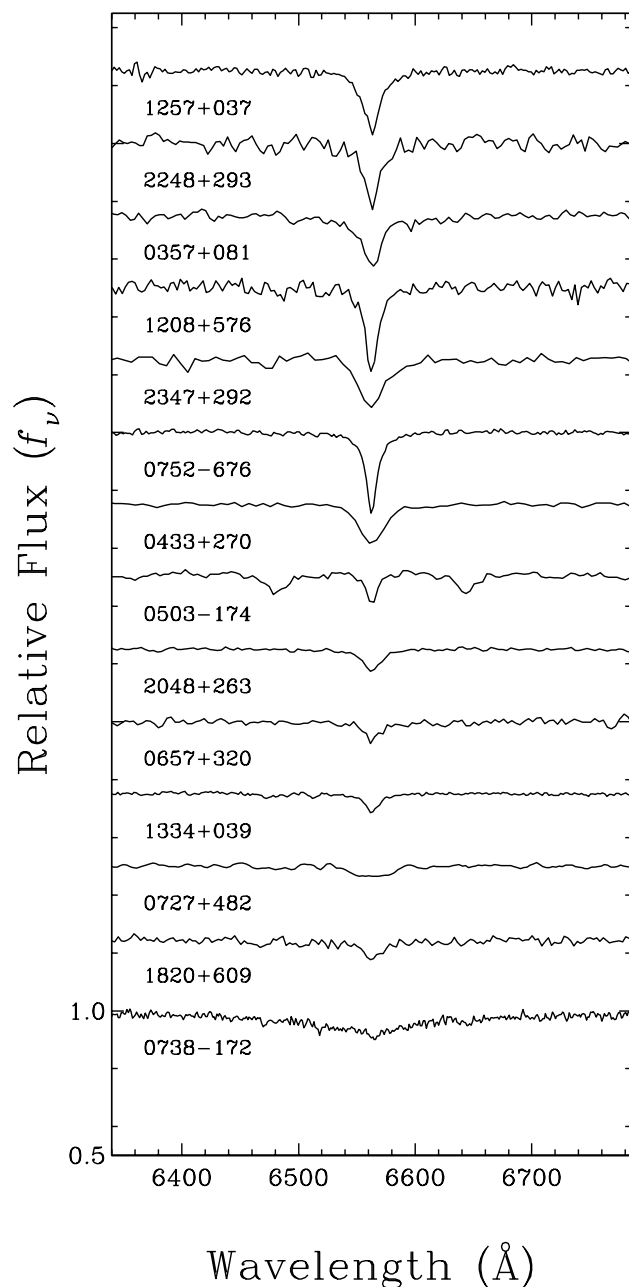


FIGURE 2.3 – (d) Optical spectra of halpha from DA and DAZ white dwarfs - continued.

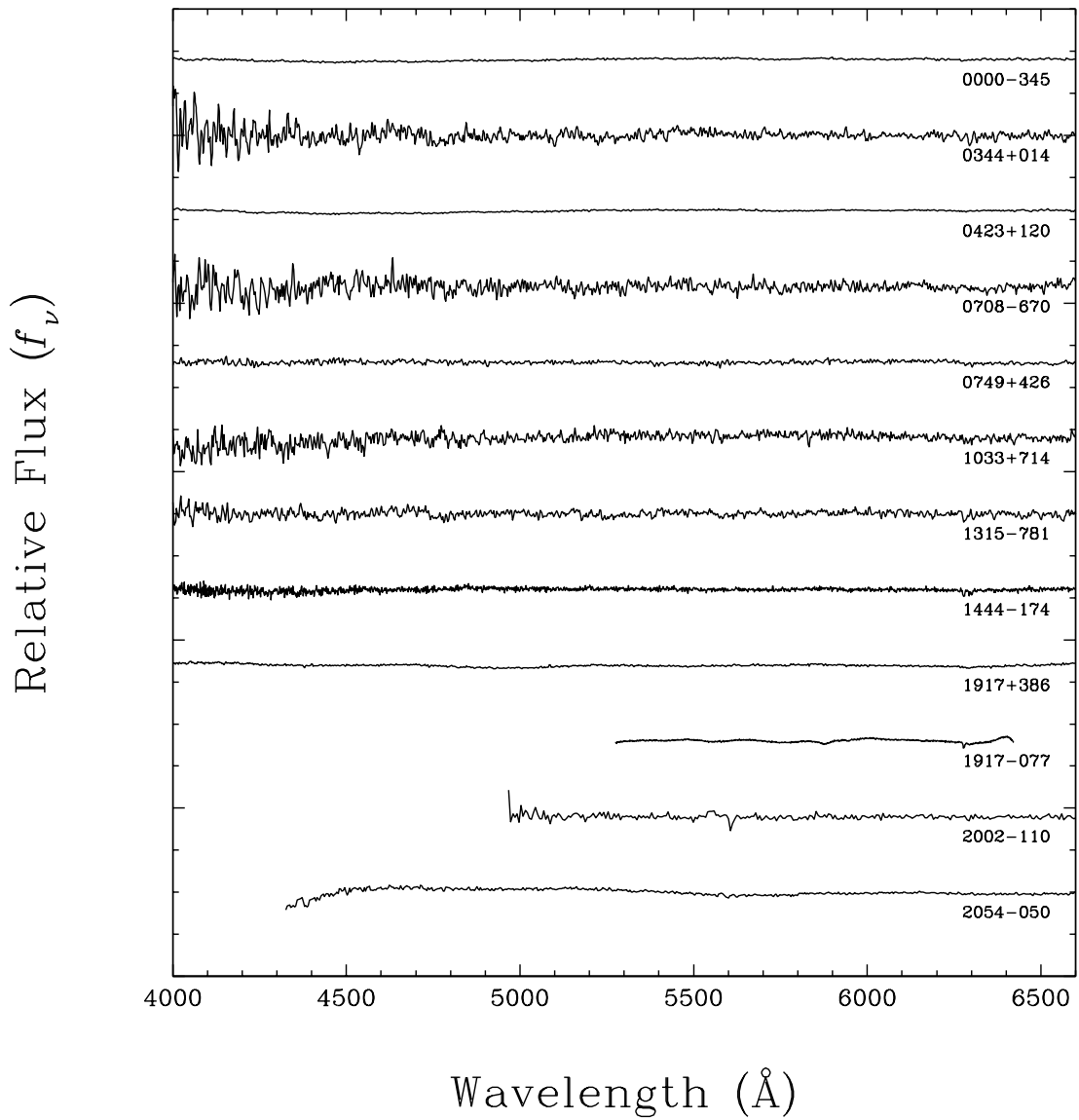


FIGURE 2.4 – (a) Our spectroscopic observations of featureless DC stars. All spectra are normalized at 6100 \AA and are offset from each other by a factor of 0.9. The spectrum of the DBQA star LDS 678A (1917–077) is also displayed.

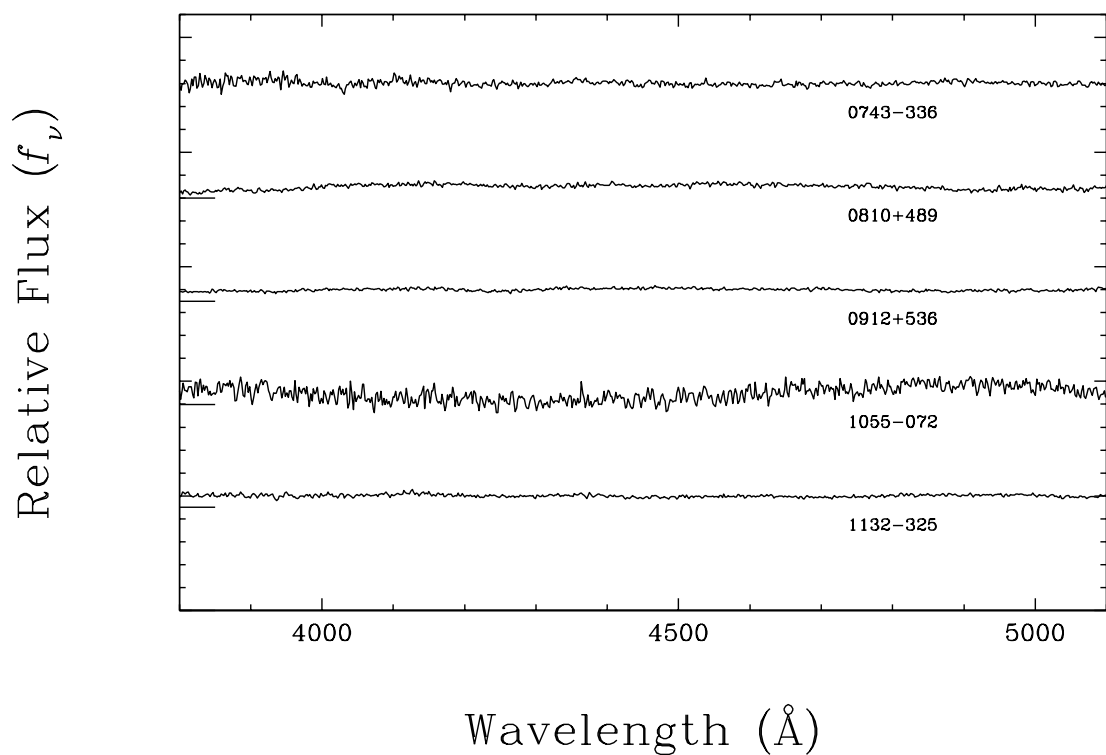


FIGURE 2.4 – (b) Blue coverage of our spectroscopic observations of DC stars. All spectra are normalized at 4800 Å and are offset from each other by a factor of 0.6.

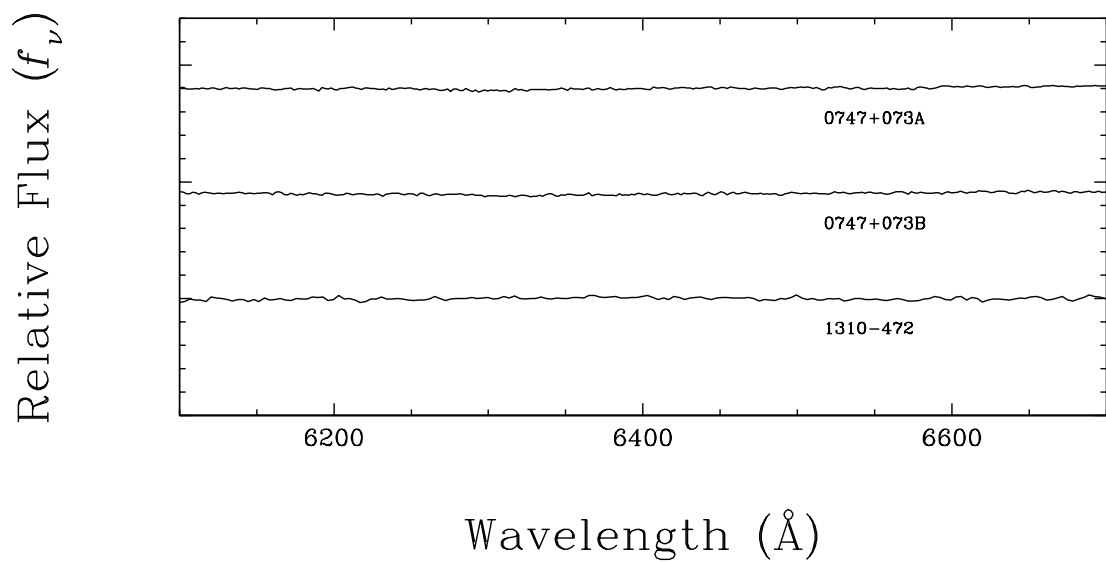


FIGURE 2.4 – (c) Red coverage of our spectroscopic observations of DC stars. All spectra are normalized at 6600 Å and are offset from each other by a factor of 0.9.

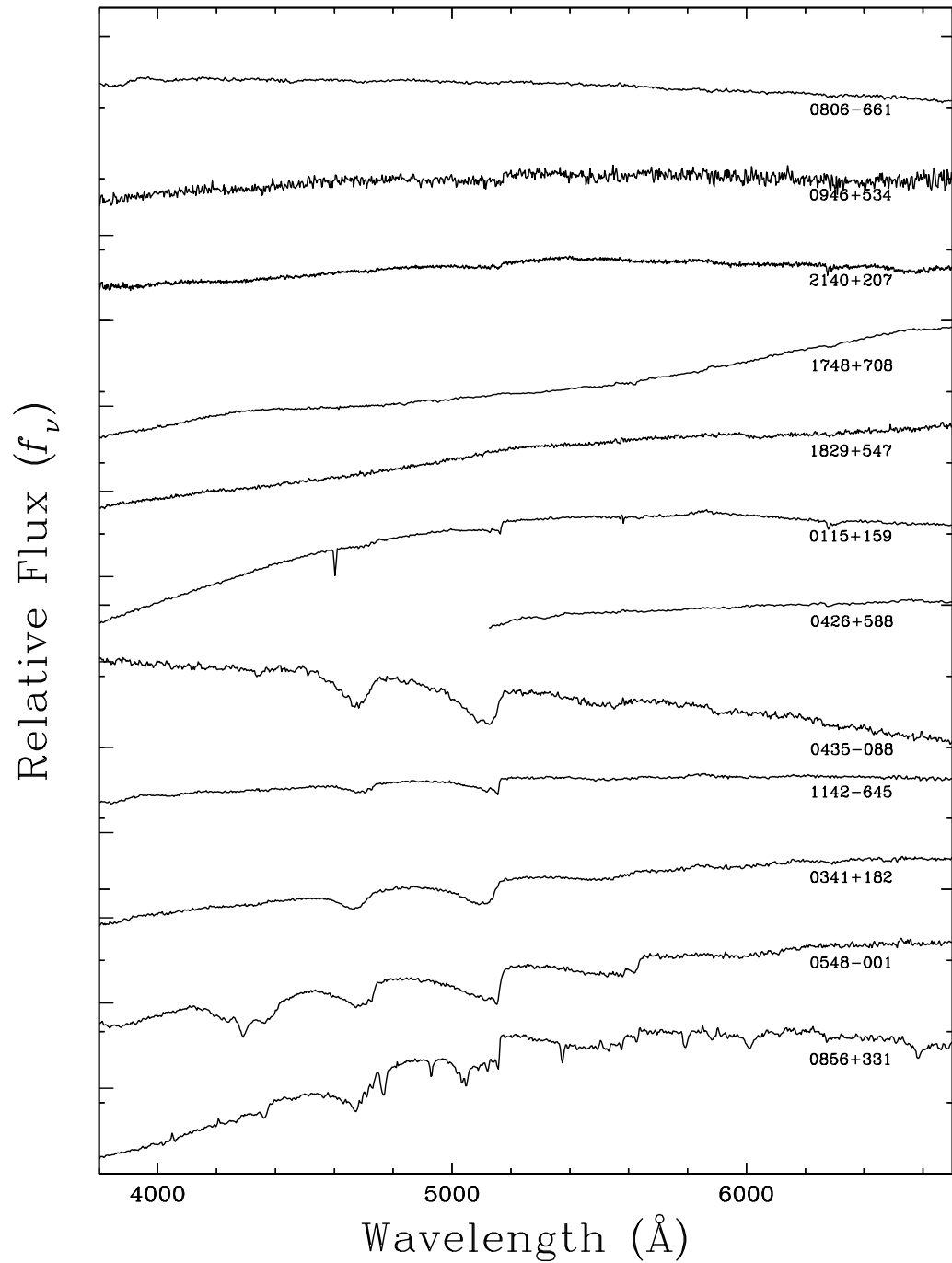


FIGURE 2.5 – (a) Our spectroscopic observations of DQ stars. All spectra are normalized at 6200 \AA and are offset from each other by a factor of 0.6.

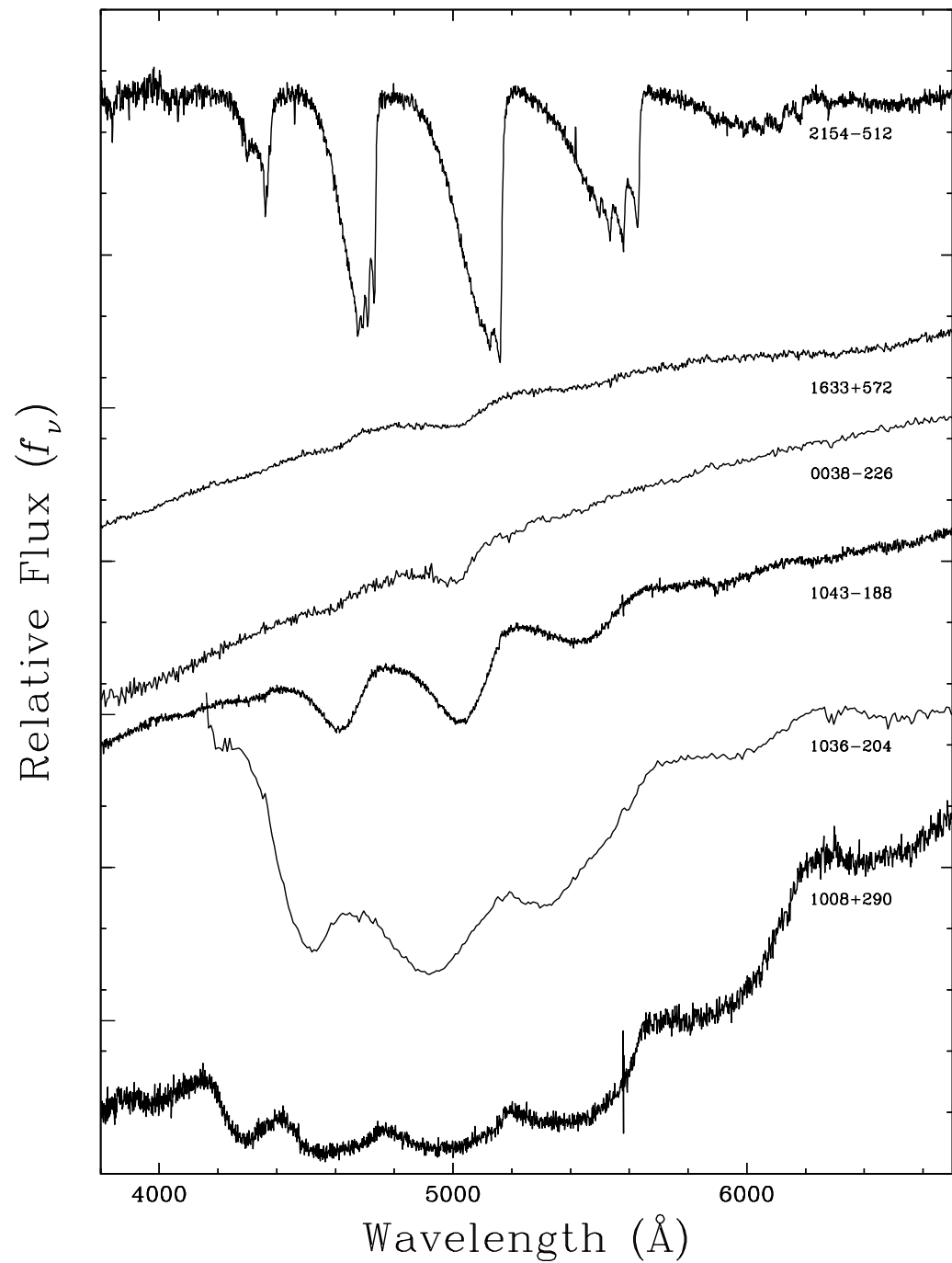


FIGURE 2.5 – (b) Our spectroscopic observations of DQ and peculiar DQ stars. All spectra are normalized at 6200 Å and are offset from each other by a factor of 0.6.

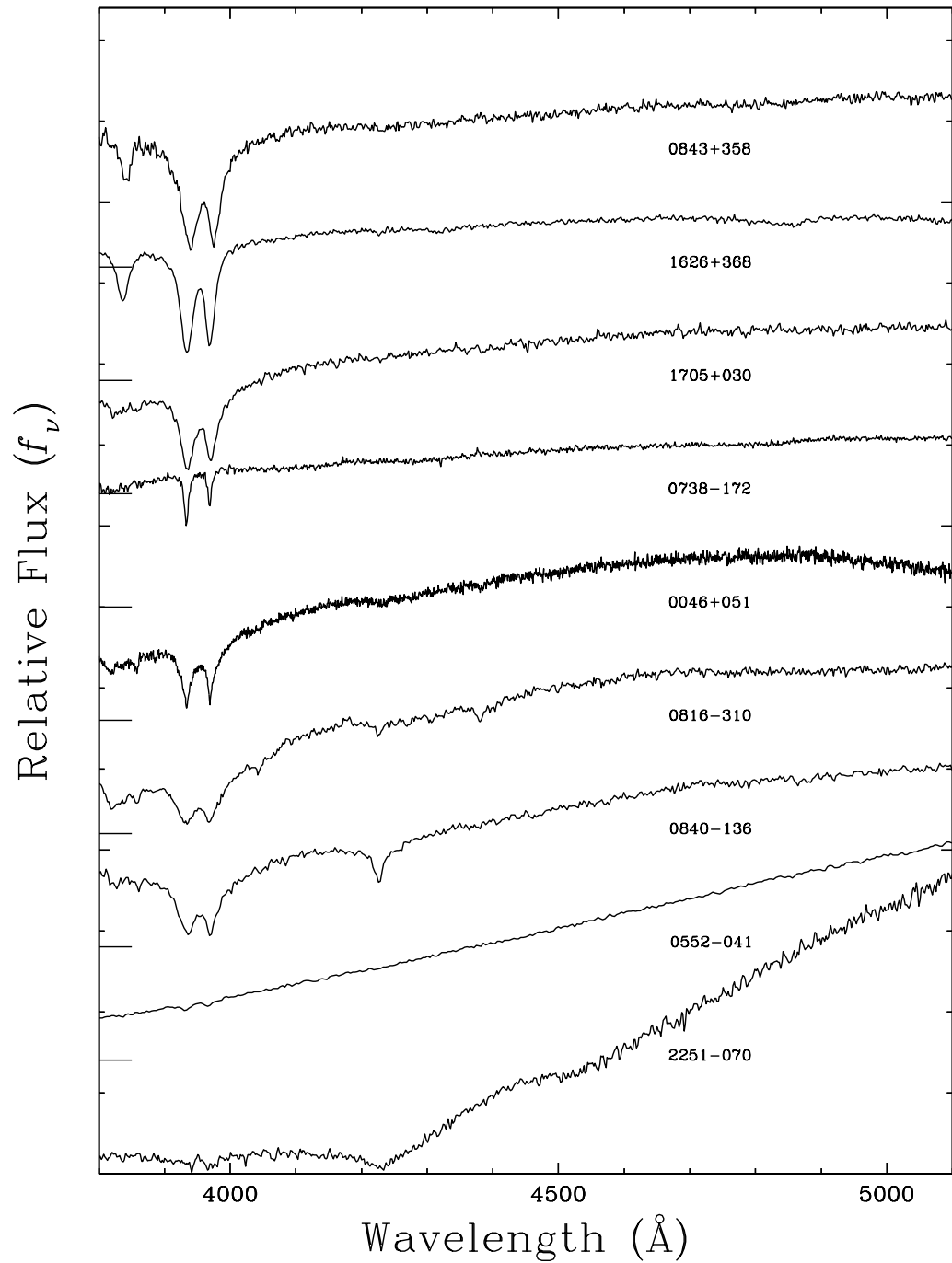


FIGURE 2.6 – Our blue spectroscopic observations of DZ stars. Spectra are shown in order of approximately decreasing metal lines strength, from top to bottom. All spectra are normalized at 4700 Å and are offset from each other by a factor of 0.7.

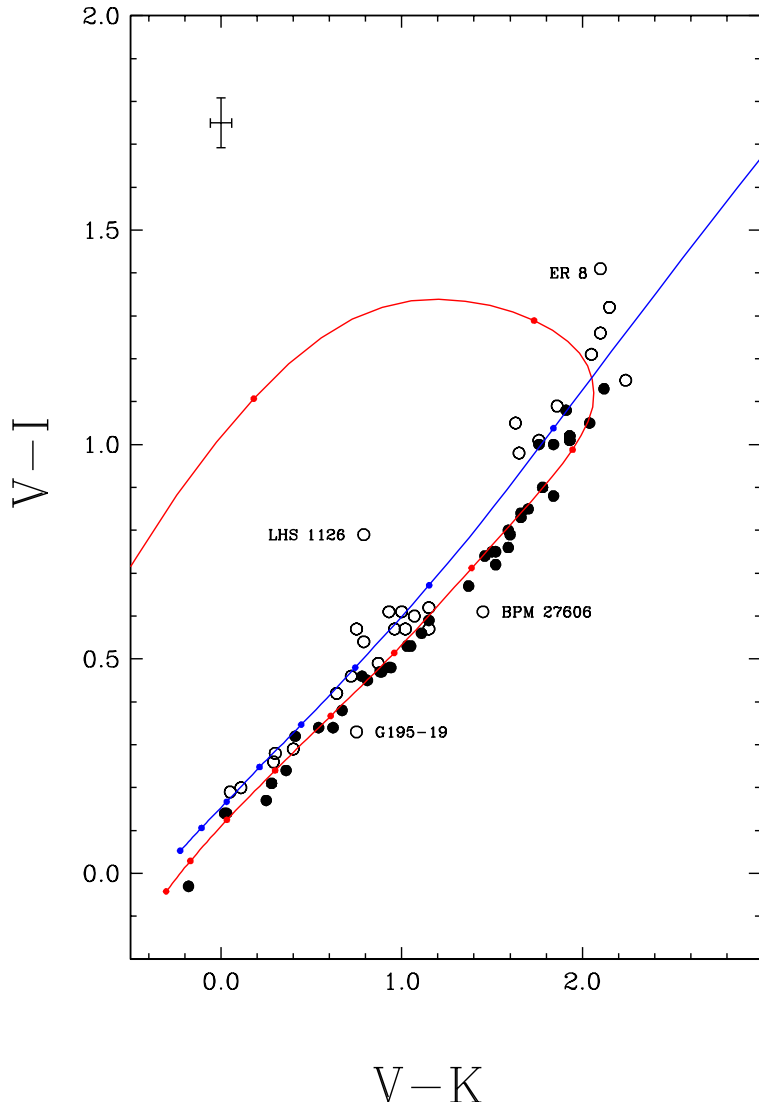


FIGURE 2.7 – ($V - I$, $V - K$) two-color diagram for the data set from Table 2.1. DA and non-DA stars are represented by filled and open circles, respectively, and the cross indicates the size of the average error bar. The pure hydrogen (red line) and pure helium (blue line) model sequences at $\log g = 8.0$ are superimposed on the observed data. Temperatures are indicated by small filled circles every 10^3 K on the cooling sequence, starting at 12,000 K at the bottom left, down to 3000 K.

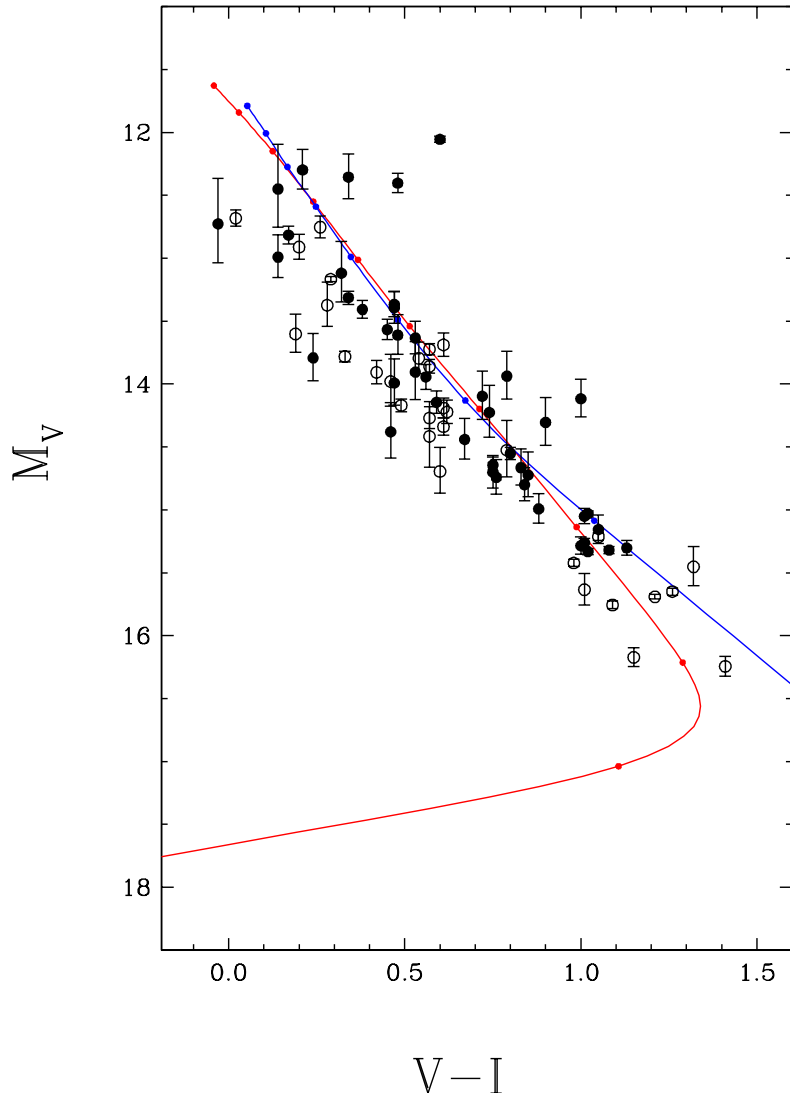


FIGURE 2.8 – M_V vs. $(V-I)$ color-magnitude diagram for the data set from Table 2.1. Objects are split into DA stars (filled circles) and non-DA stars (open circles), based on the presence or absence of $H\alpha$. The pure hydrogen (red line) and pure helium (blue line) model sequences at $\log g = 8.0$ are superimposed on the observed data. Temperatures are indicated by small filled circles every 10^3 K on the cooling sequence, starting at 12,000 K at the upper left of the diagram, down to 3000 K.

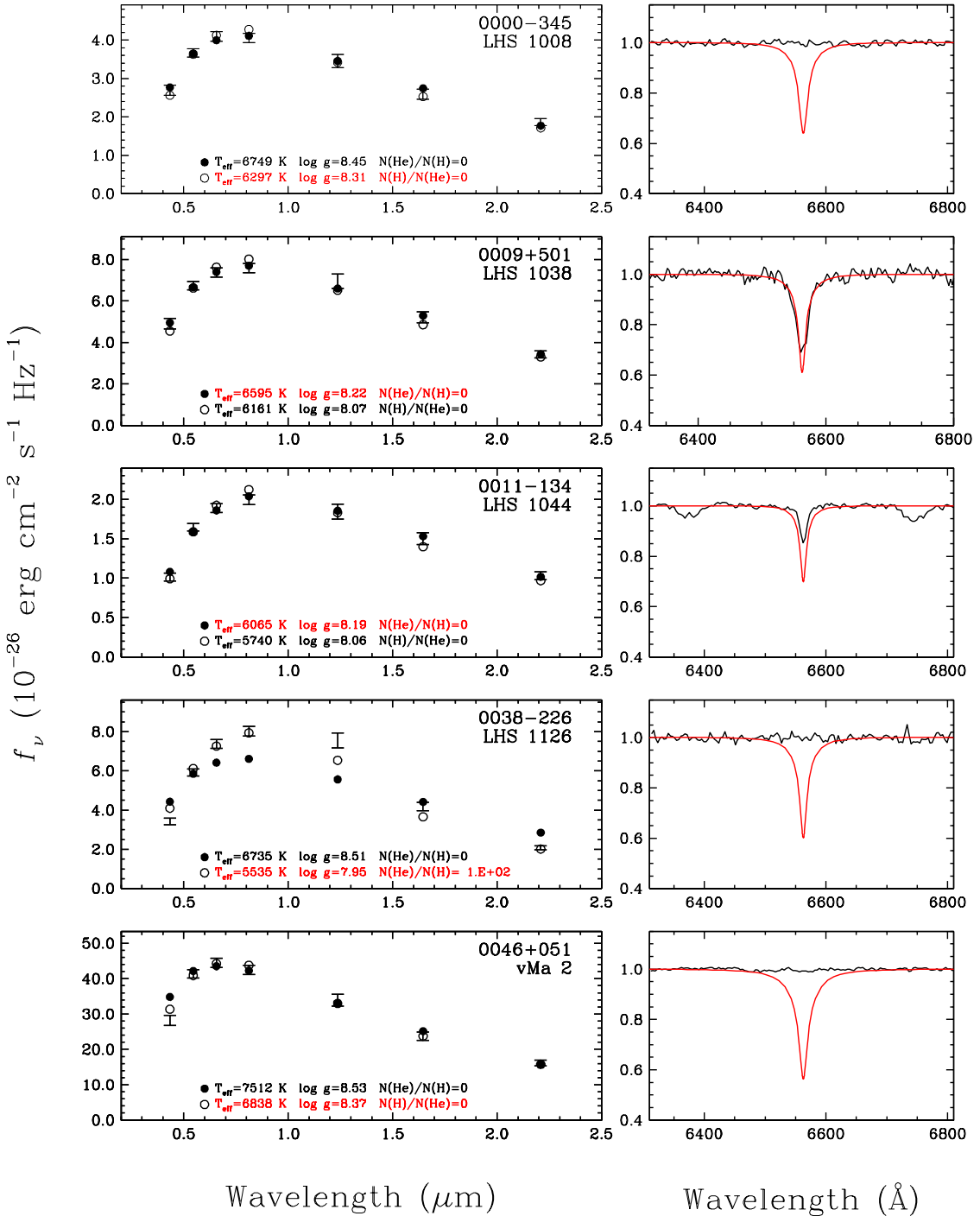


FIGURE 2.9 – (a) Fits to the energy distributions with pure hydrogen models (filled circles) and with mixed hydrogen/helium or pure helium models (open circles), with abundances indicated in each panel. Adopted atmospheric parameters and abundances are emphasized in red. Here and in the following figures, the *BVRI* and *JHK* photometric observations are represented by error bars. In the right panels are shown the observed normalized spectra together with the synthetic line profiles calculated with the atmospheric parameters corresponding to the pure hydrogen solutions.

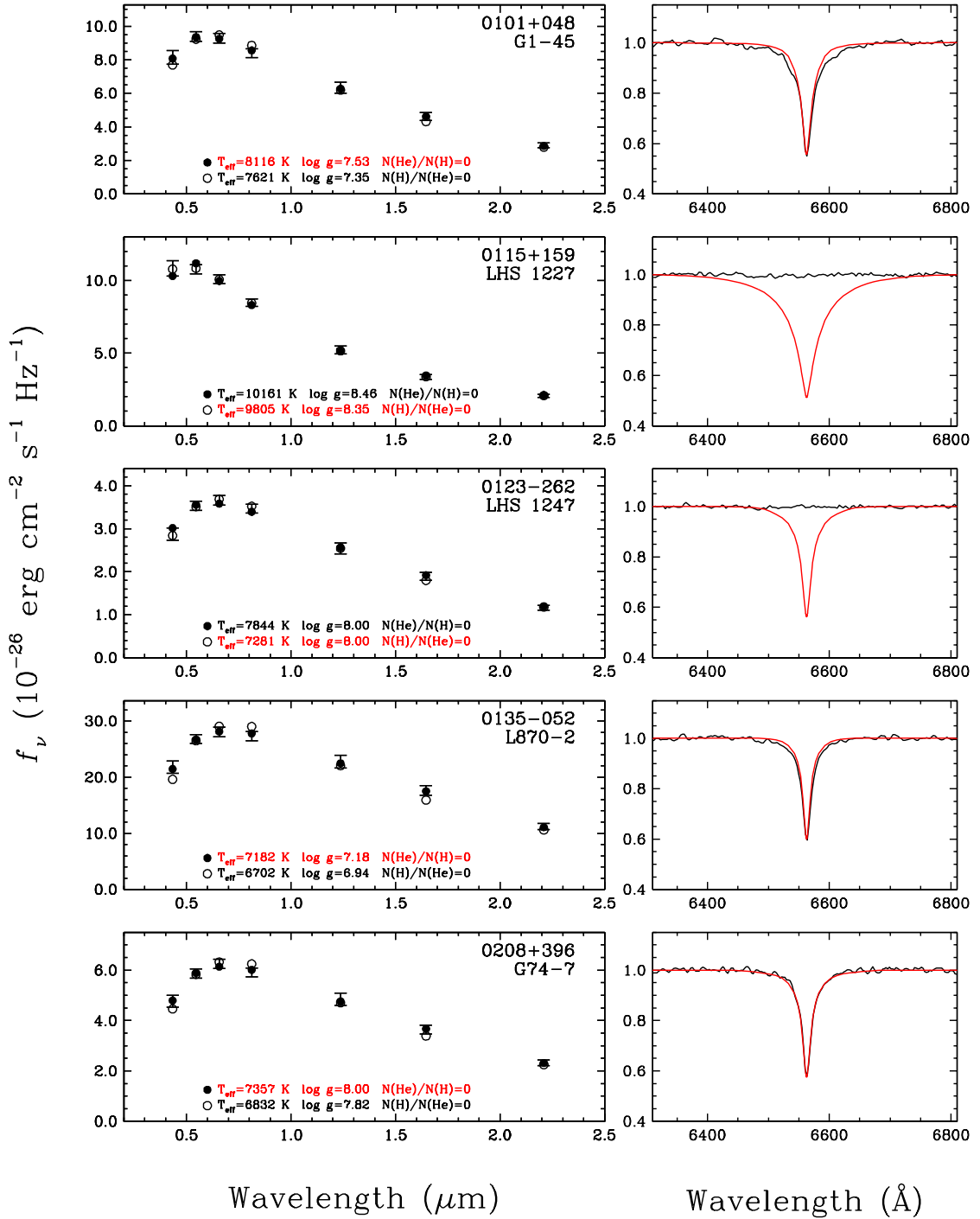


FIGURE 2.9 – (b) Fits to the energy distributions - continued.

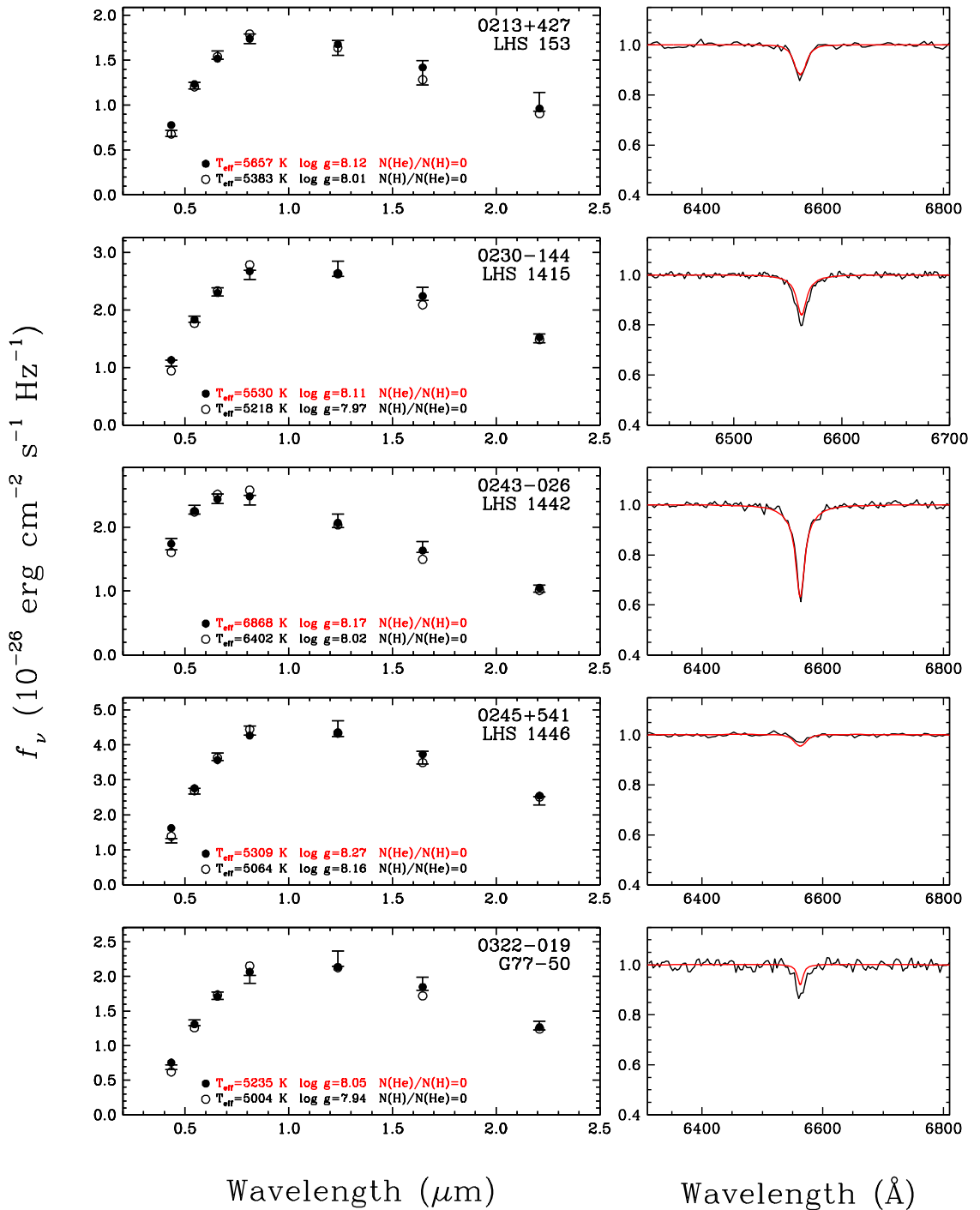


FIGURE 2.9 – (c) Fits to the energy distributions - continued.

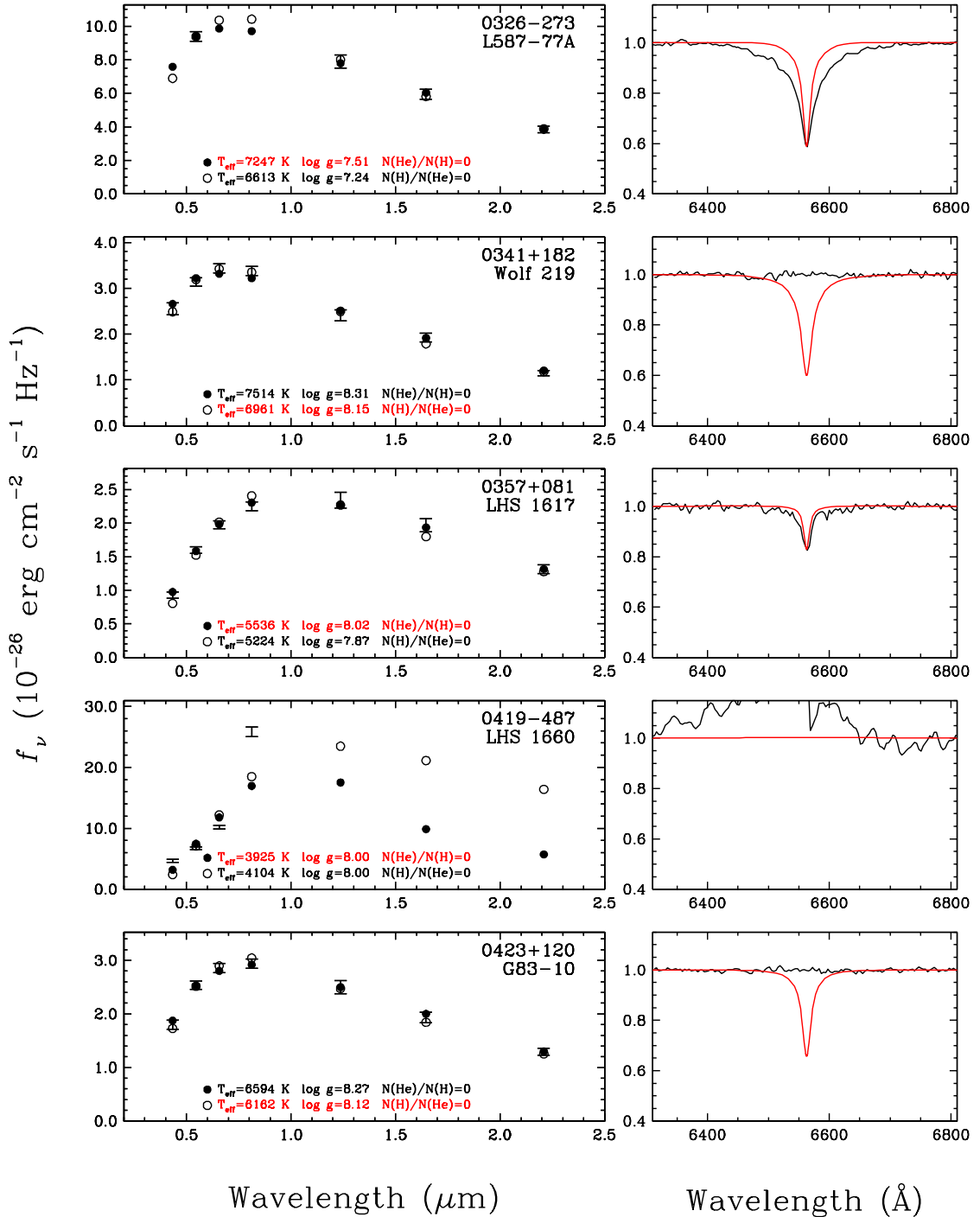


FIGURE 2.9 – (d) Fits to the energy distributions - continued.

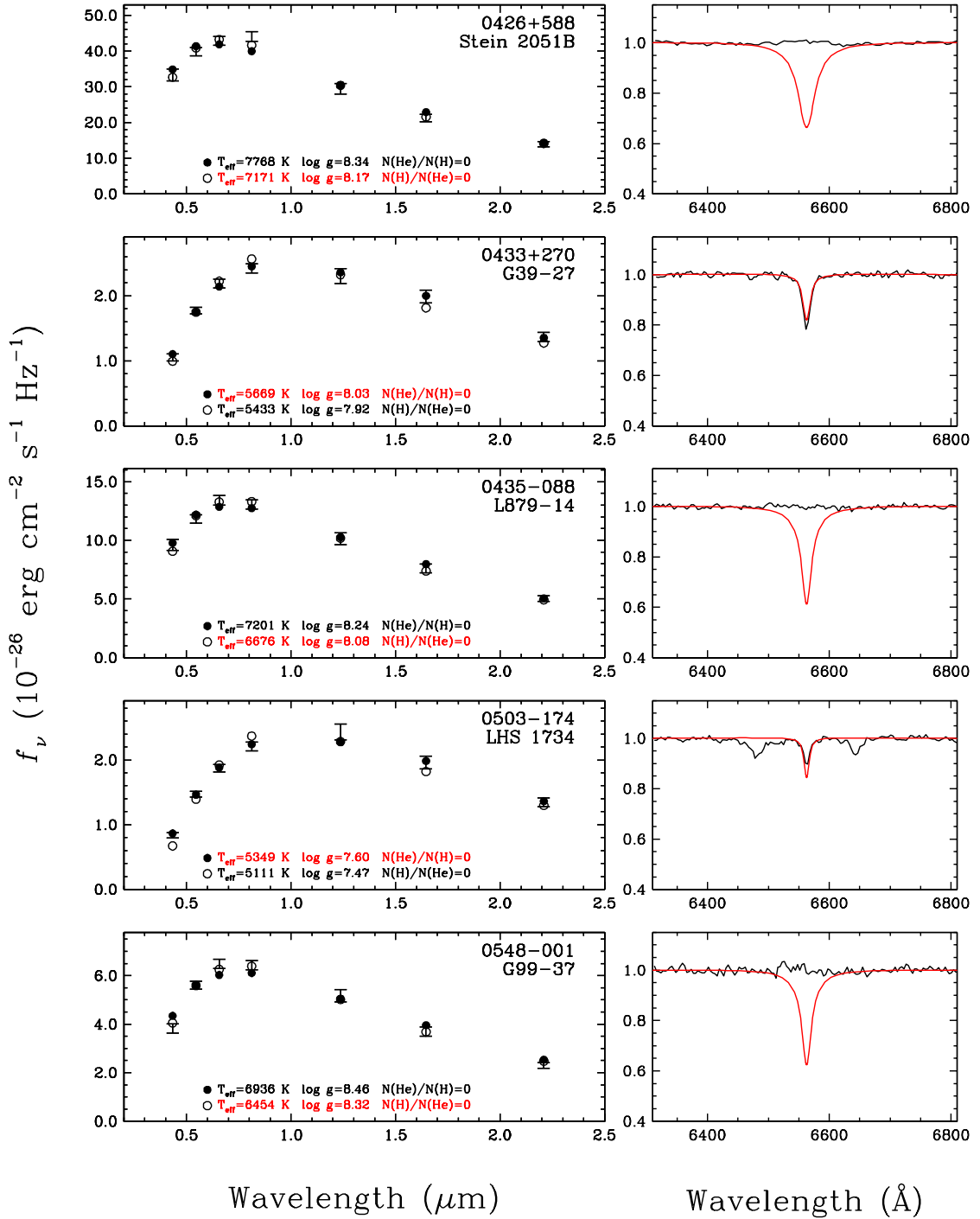


FIGURE 2.9 – (e) Fits to the energy distributions - continued.

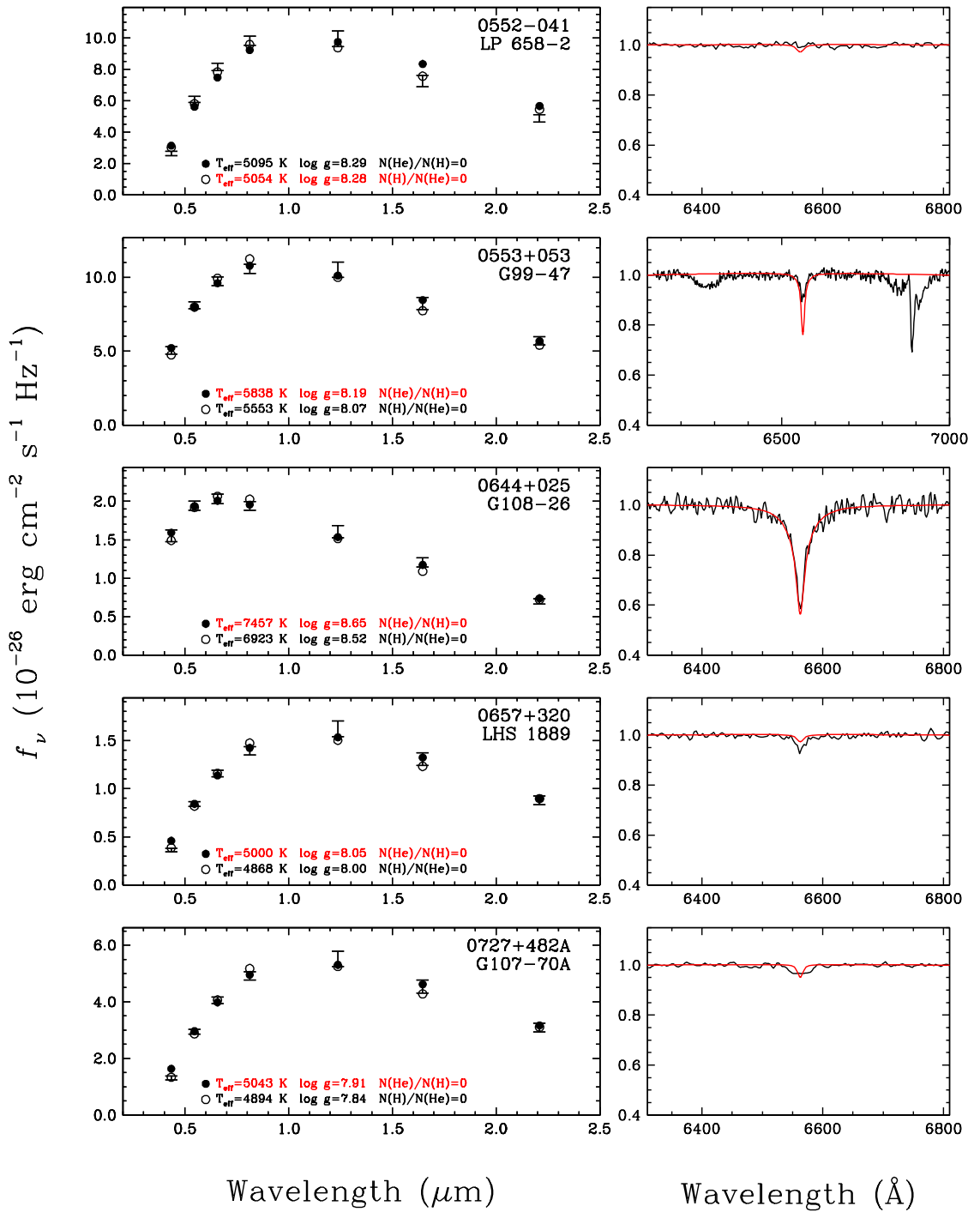


FIGURE 2.9 – (f) Fits to the energy distributions - continued.

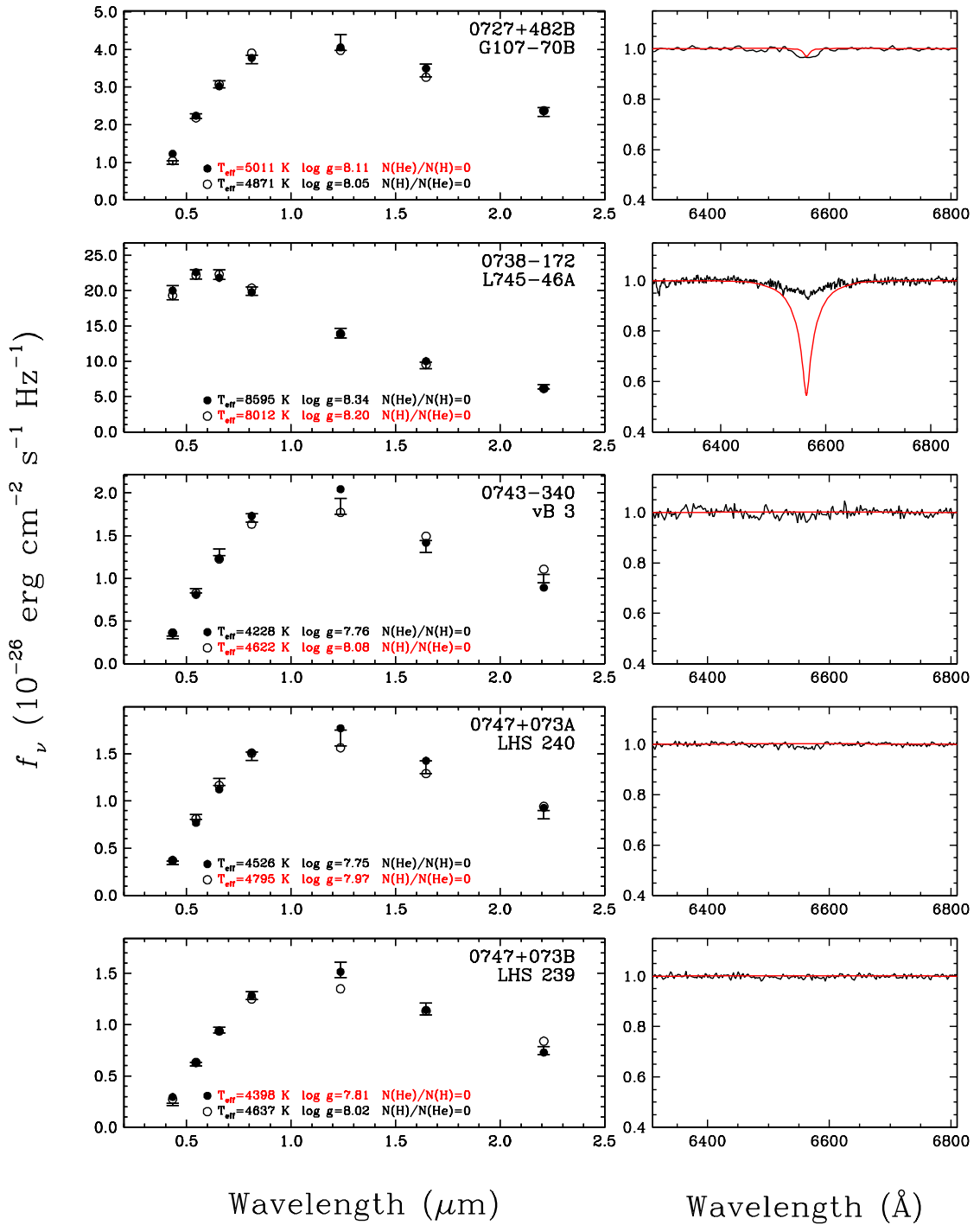


FIGURE 2.9 – (g) Fits to the energy distributions - continued.

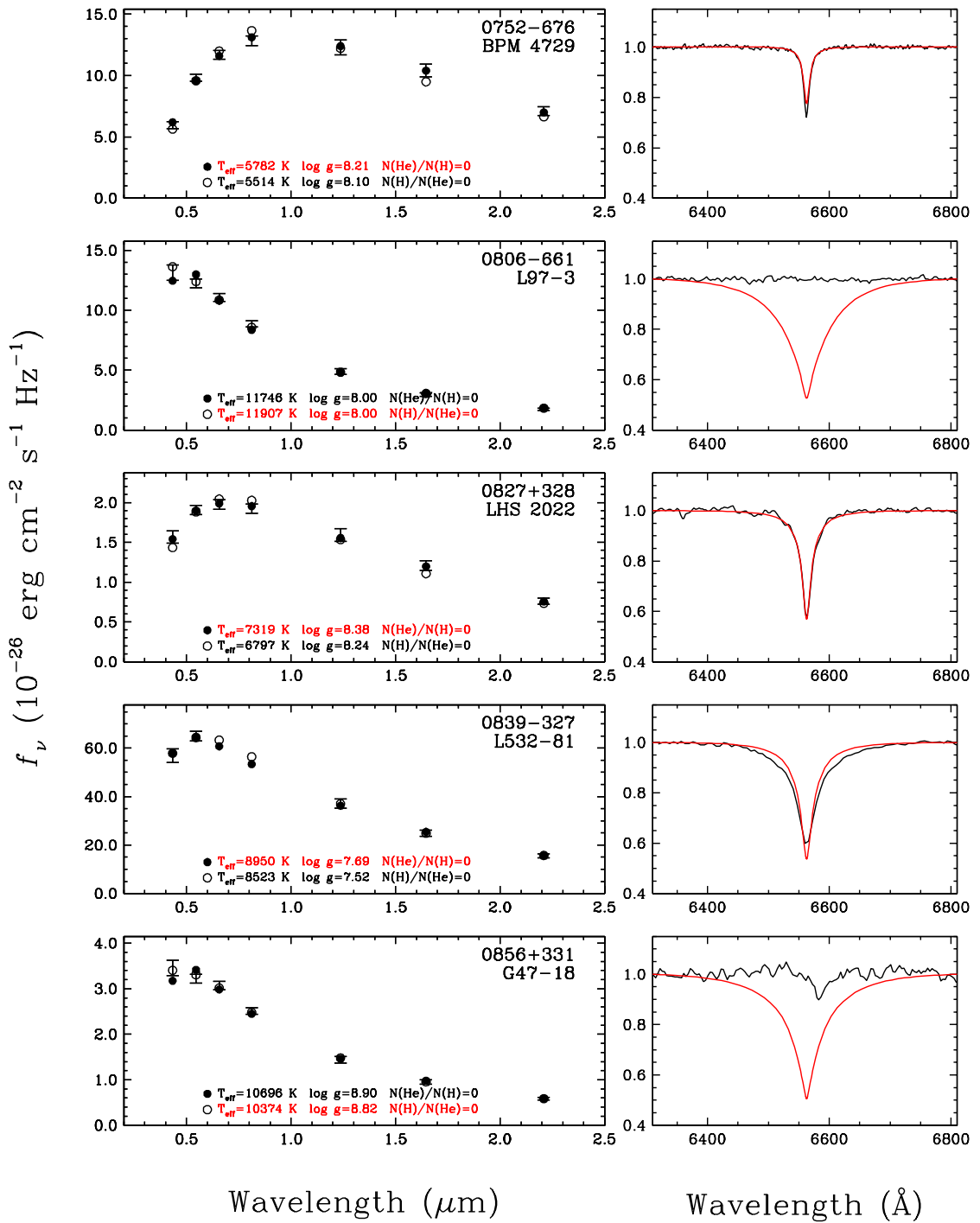


FIGURE 2.9 – (h) Fits to the energy distributions - continued.

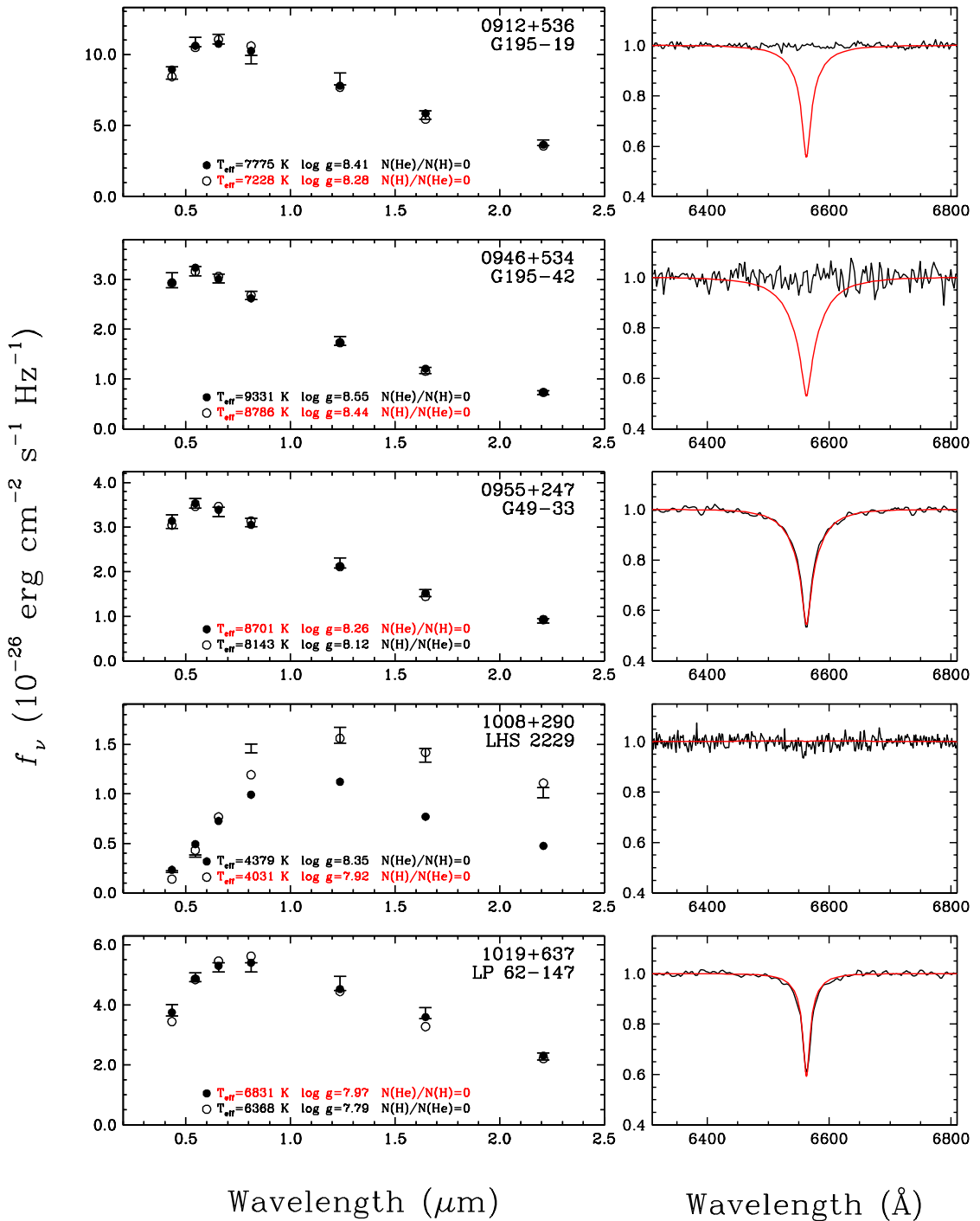


FIGURE 2.9 – (i) Fits to the energy distributions - continued.

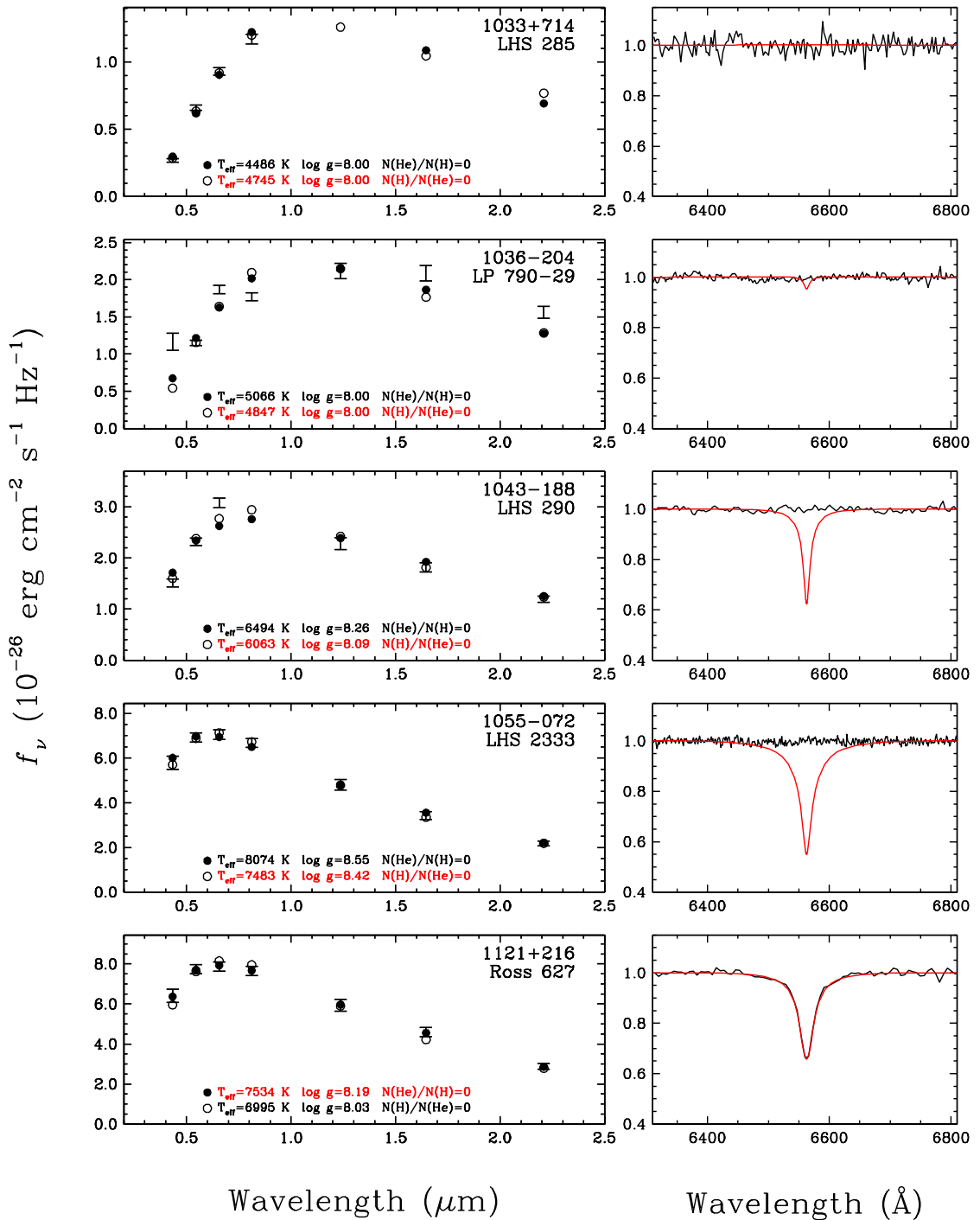


FIGURE 2.9 – (j) Fits to the energy distributions - continued.

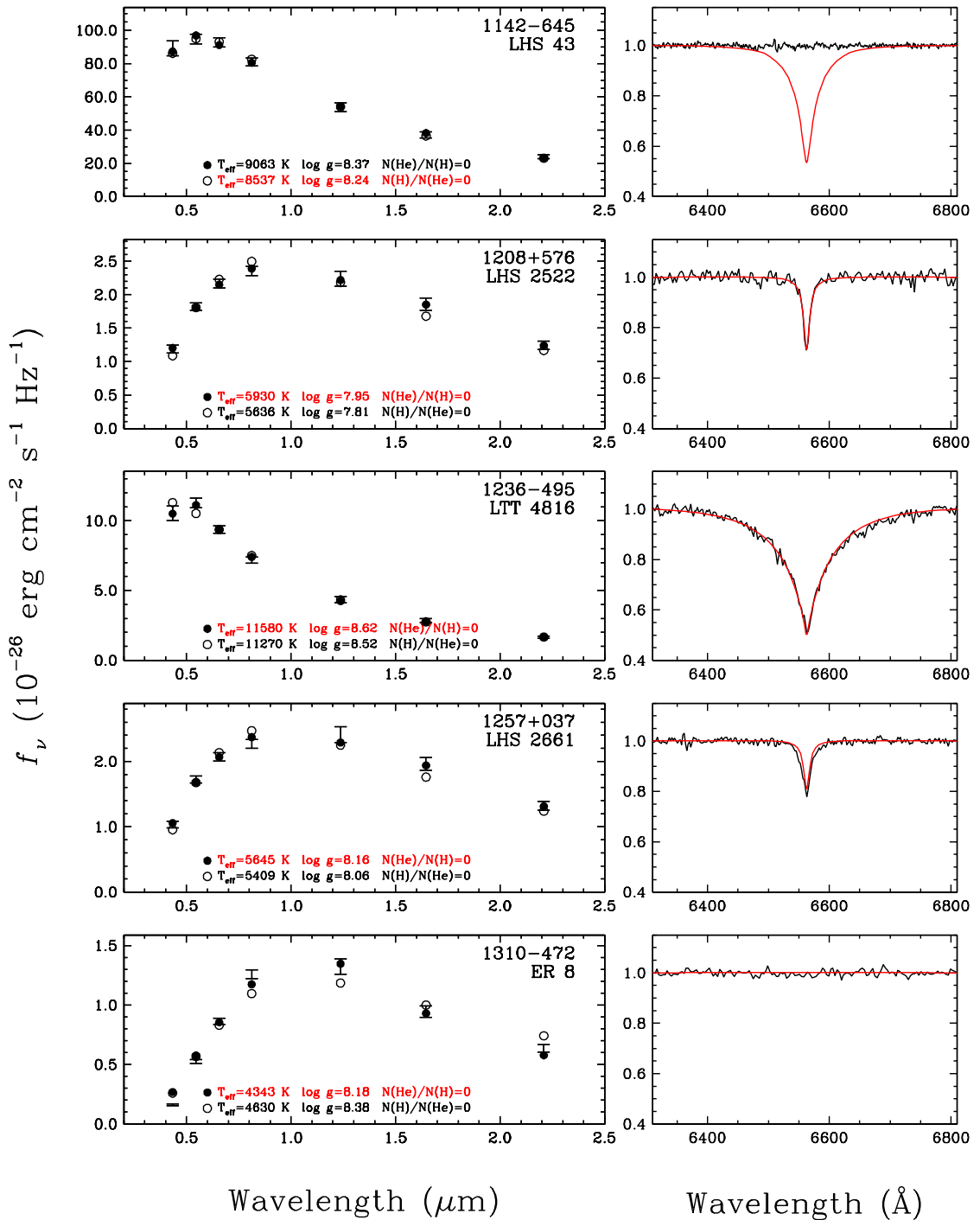


FIGURE 2.9 – (k) Fits to the energy distributions - continued.

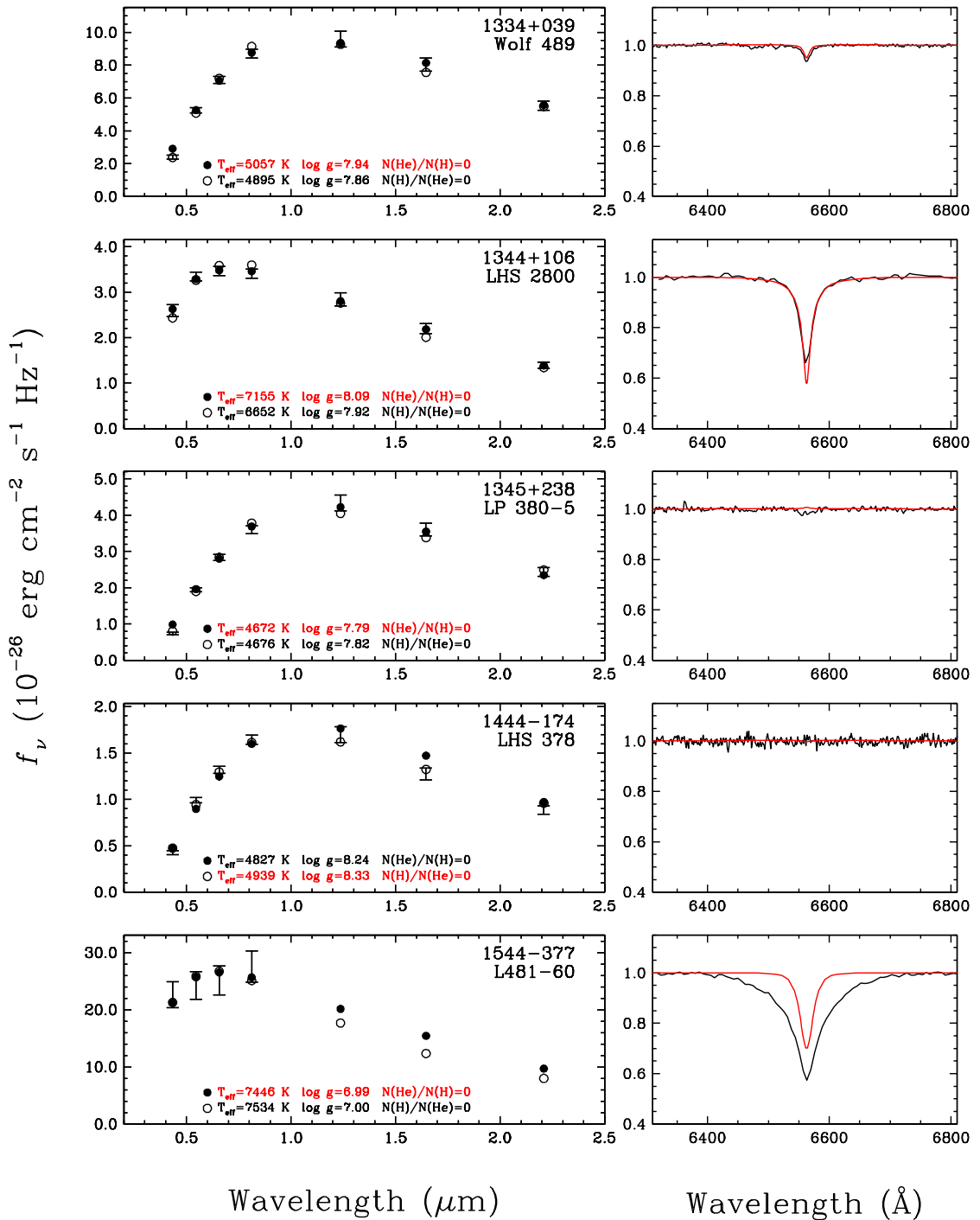


FIGURE 2.9 – (l) Fits to the energy distributions - continued.

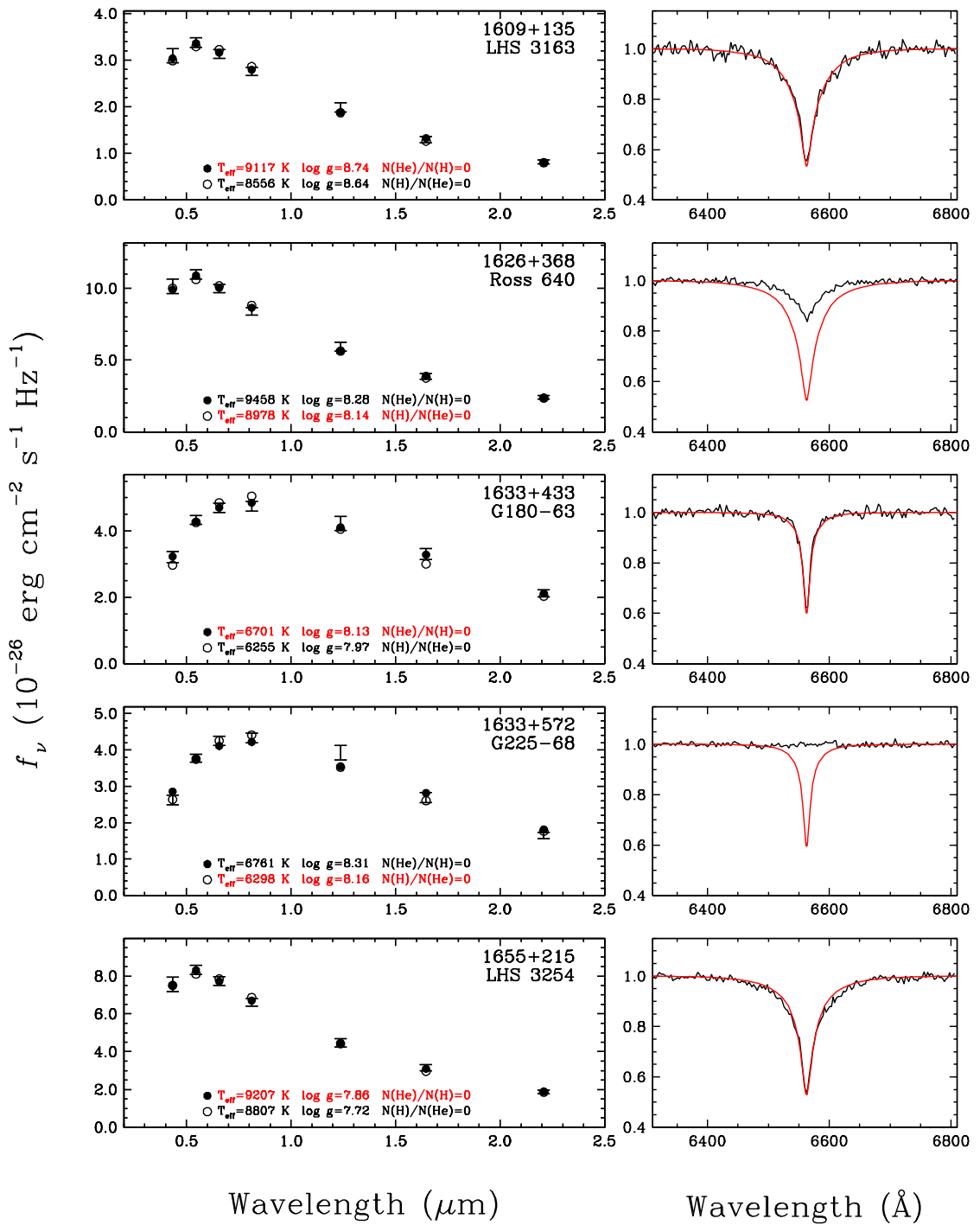


FIGURE 2.9 – (m) Fits to the energy distributions - continued.

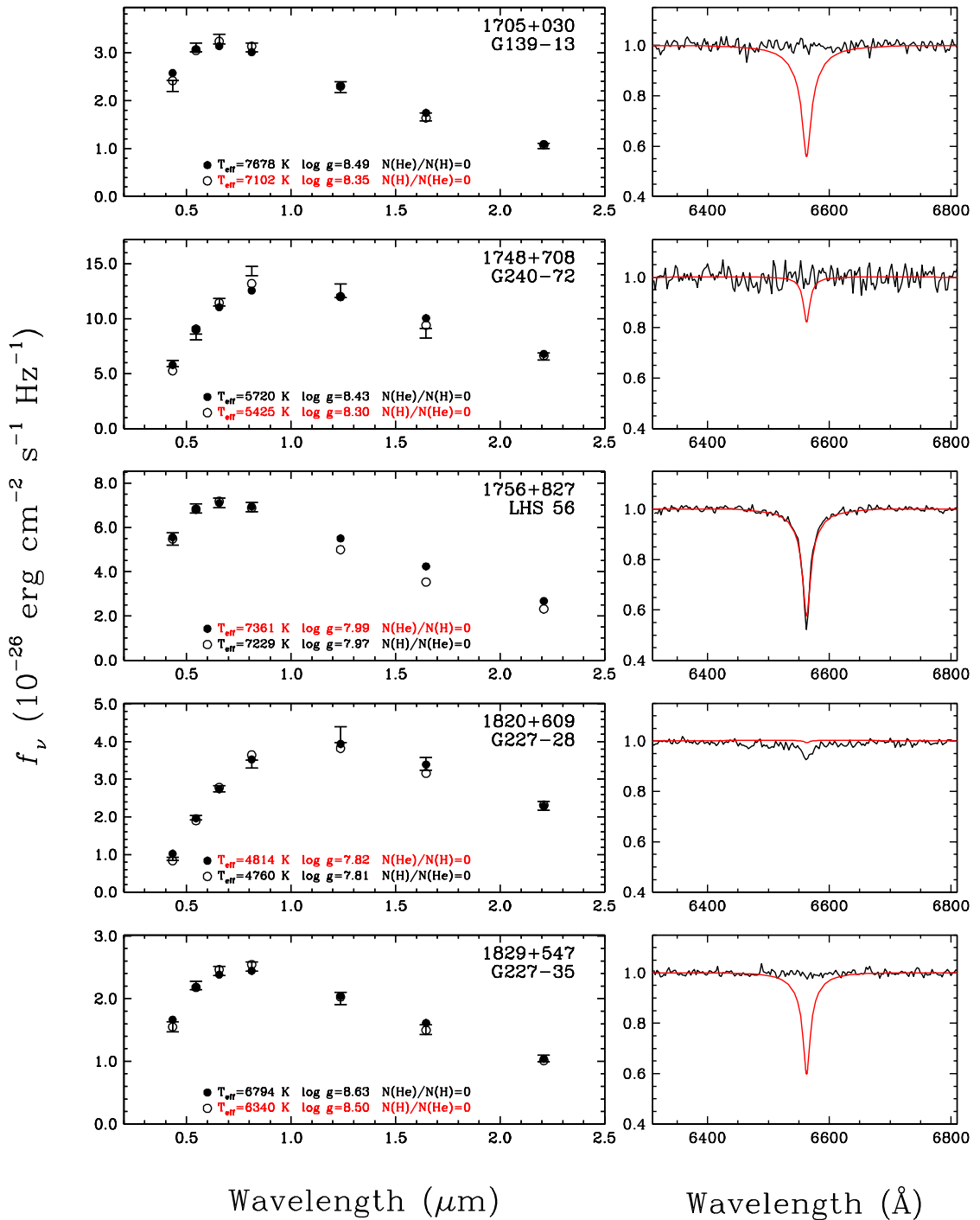


FIGURE 2.9 – (n) Fits to the energy distributions - continued.

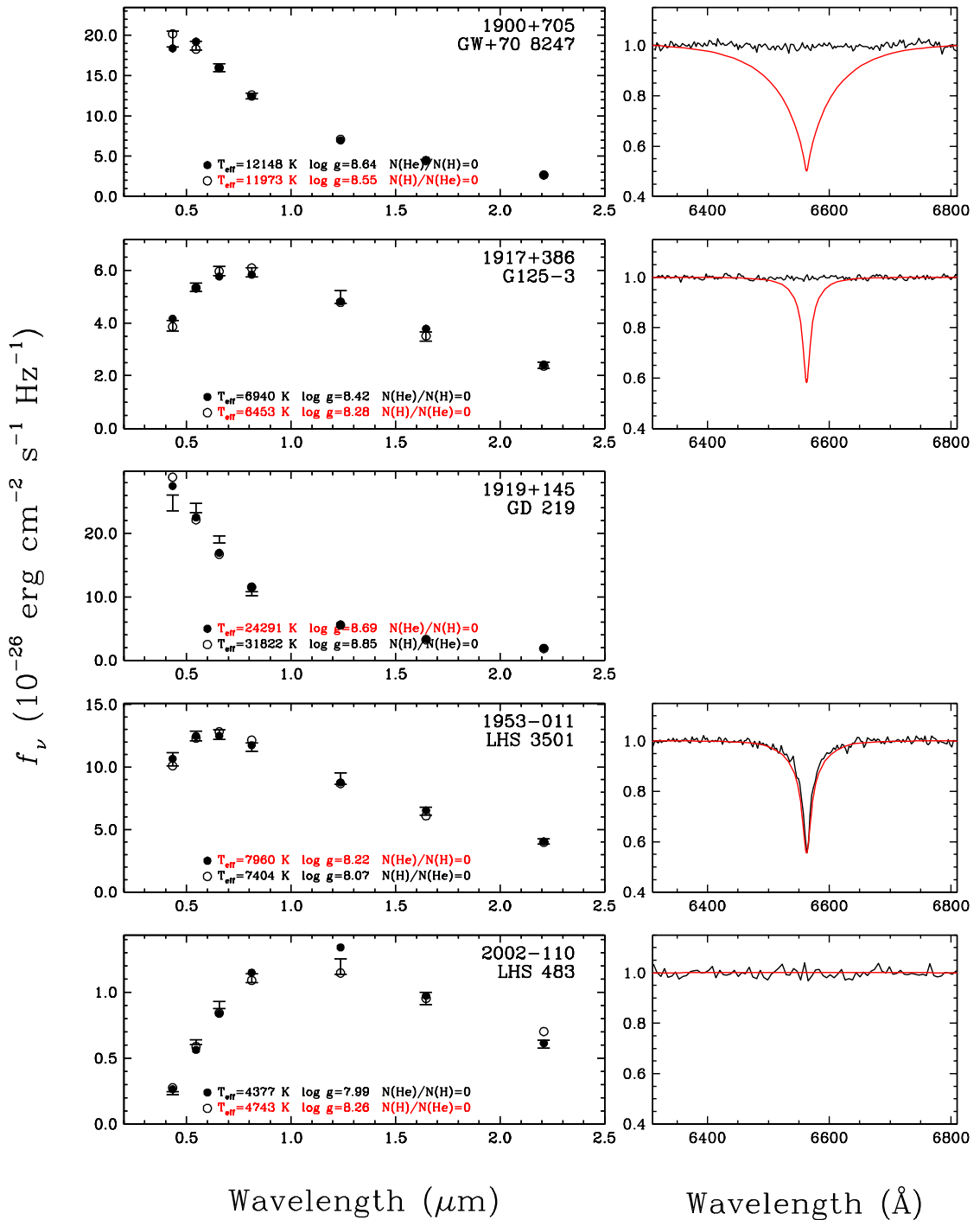


FIGURE 2.9 – (o) Fits to the energy distributions - continued.

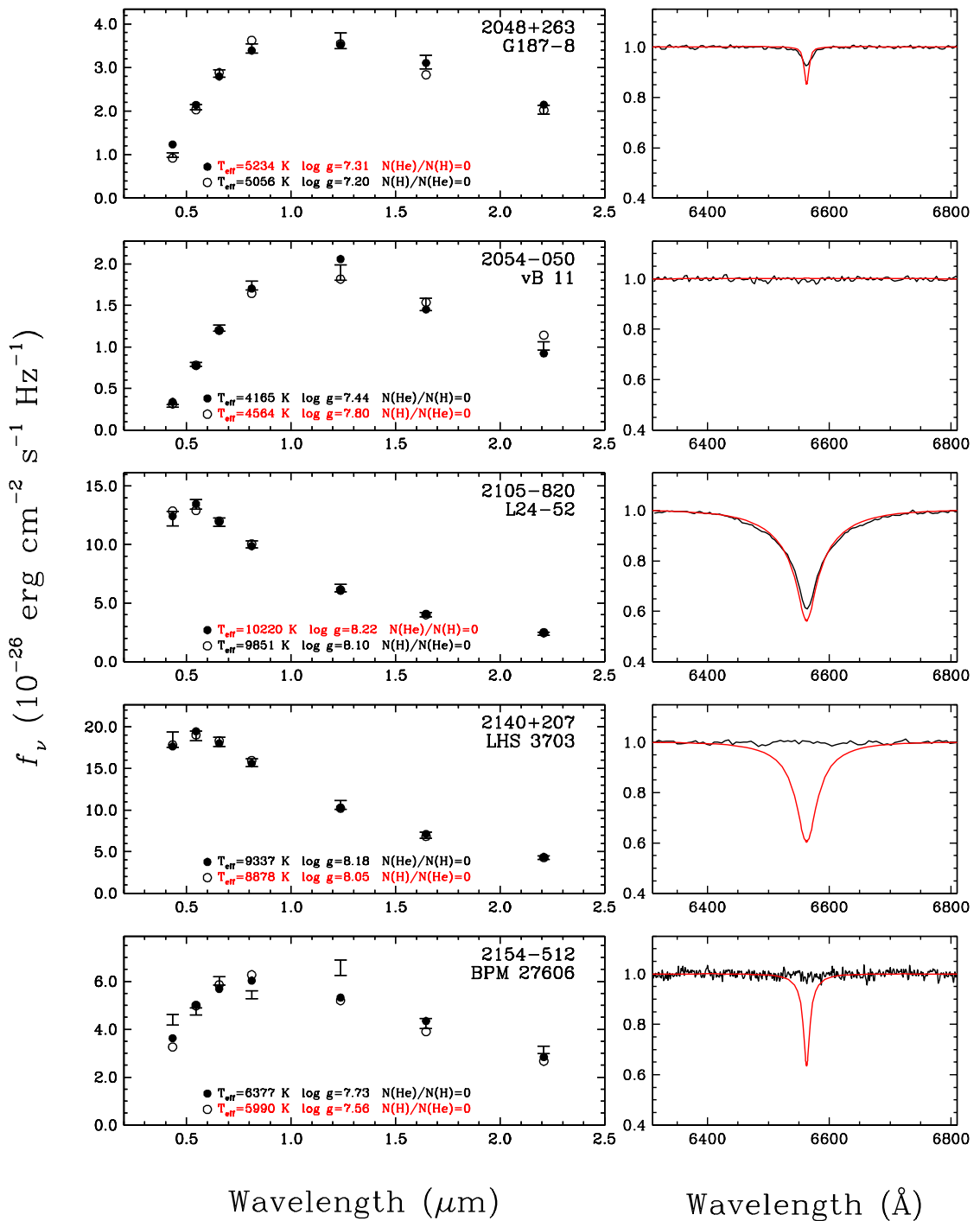


FIGURE 2.9 – (p) Fits to the energy distributions - continued.

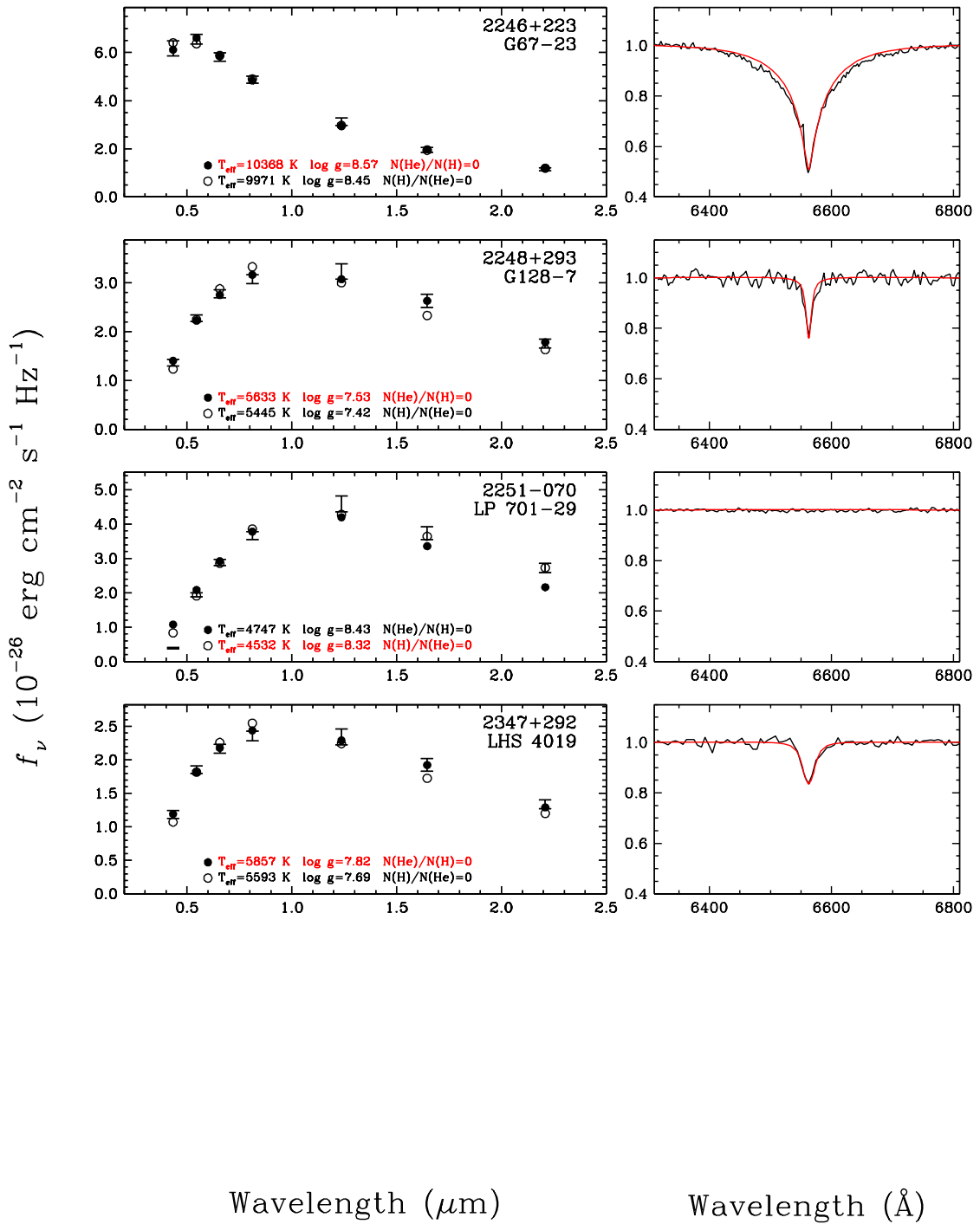


FIGURE 2.9 – (q) Fits to the energy distributions - continued.

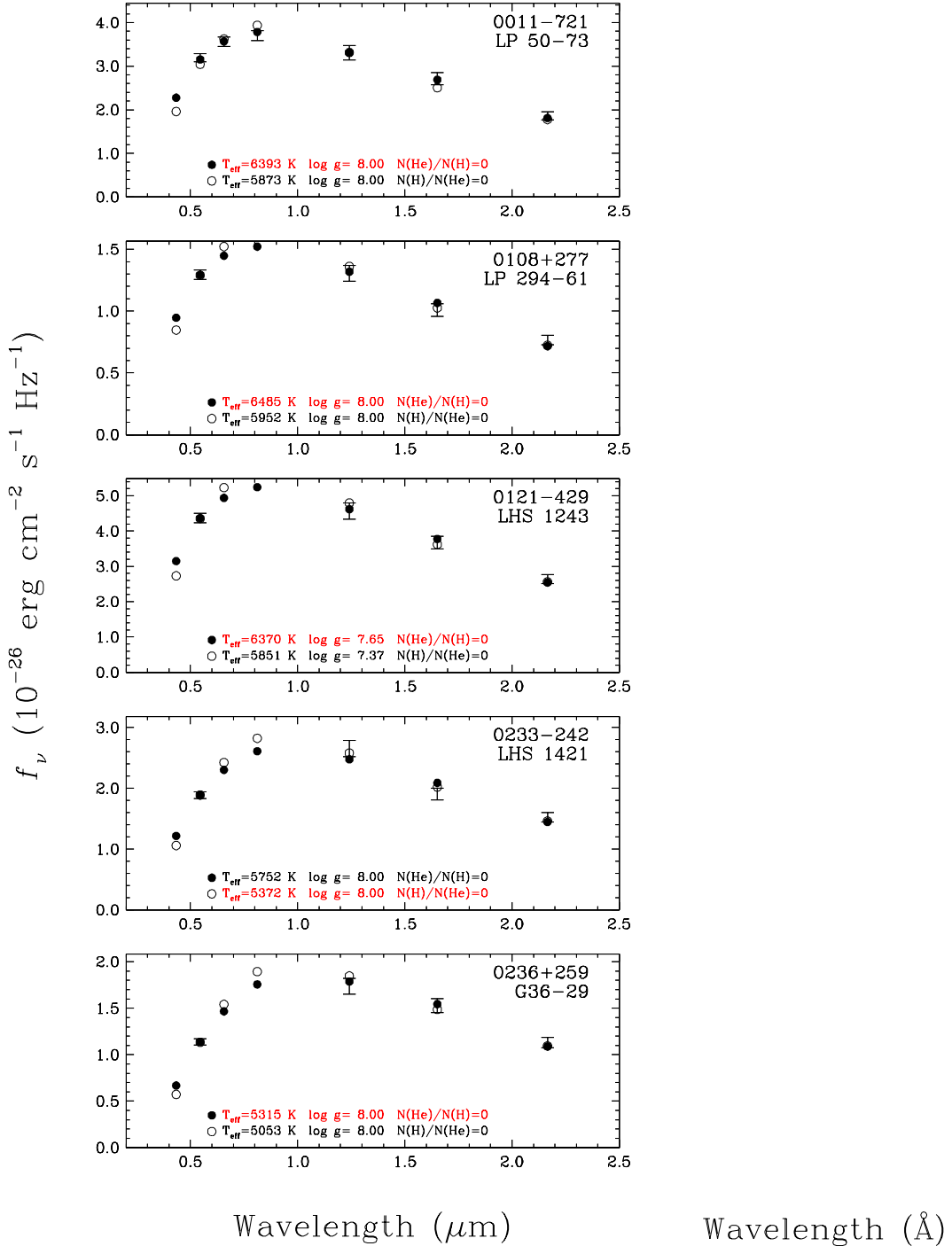


FIGURE 2.10 – (a) Fits to the energy distributions of objects with optical and JHK_S photometry with pure hydrogen models (filled circles) and pure helium models (open circles). Adopted atmospheric parameters and abundances are emphasized in red. Here and in the following figures, the V and JHK_S photometric observations are represented by error bars. In the right panels are shown, when available, the observed normalized spectra together with the synthetic line profiles calculated with the atmospheric parameters corresponding to the pure hydrogen solutions.

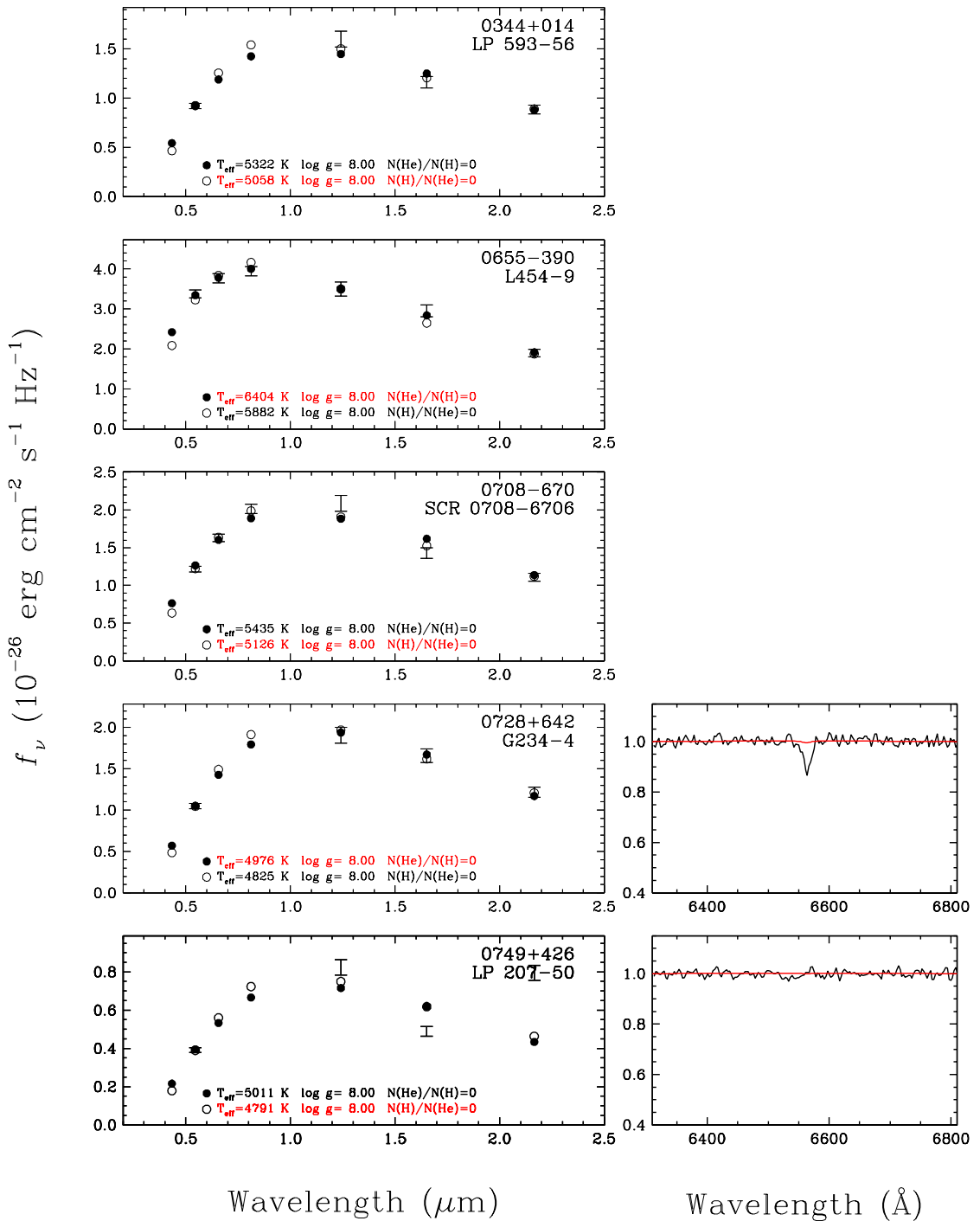


FIGURE 2.10 – (b) Fits to the energy distributions - continued.

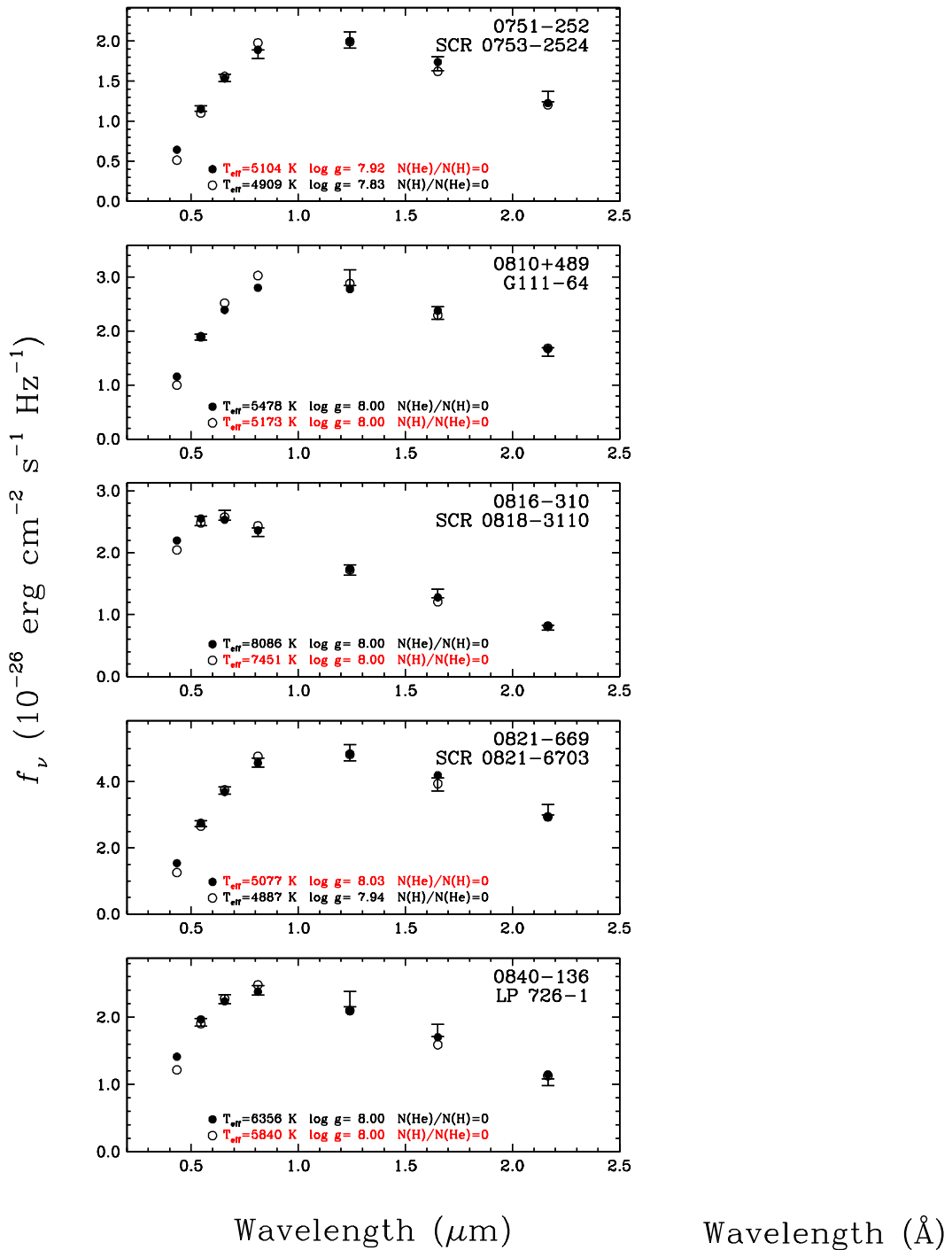


FIGURE 2.10 – (c) Fits to the energy distributions - continued.

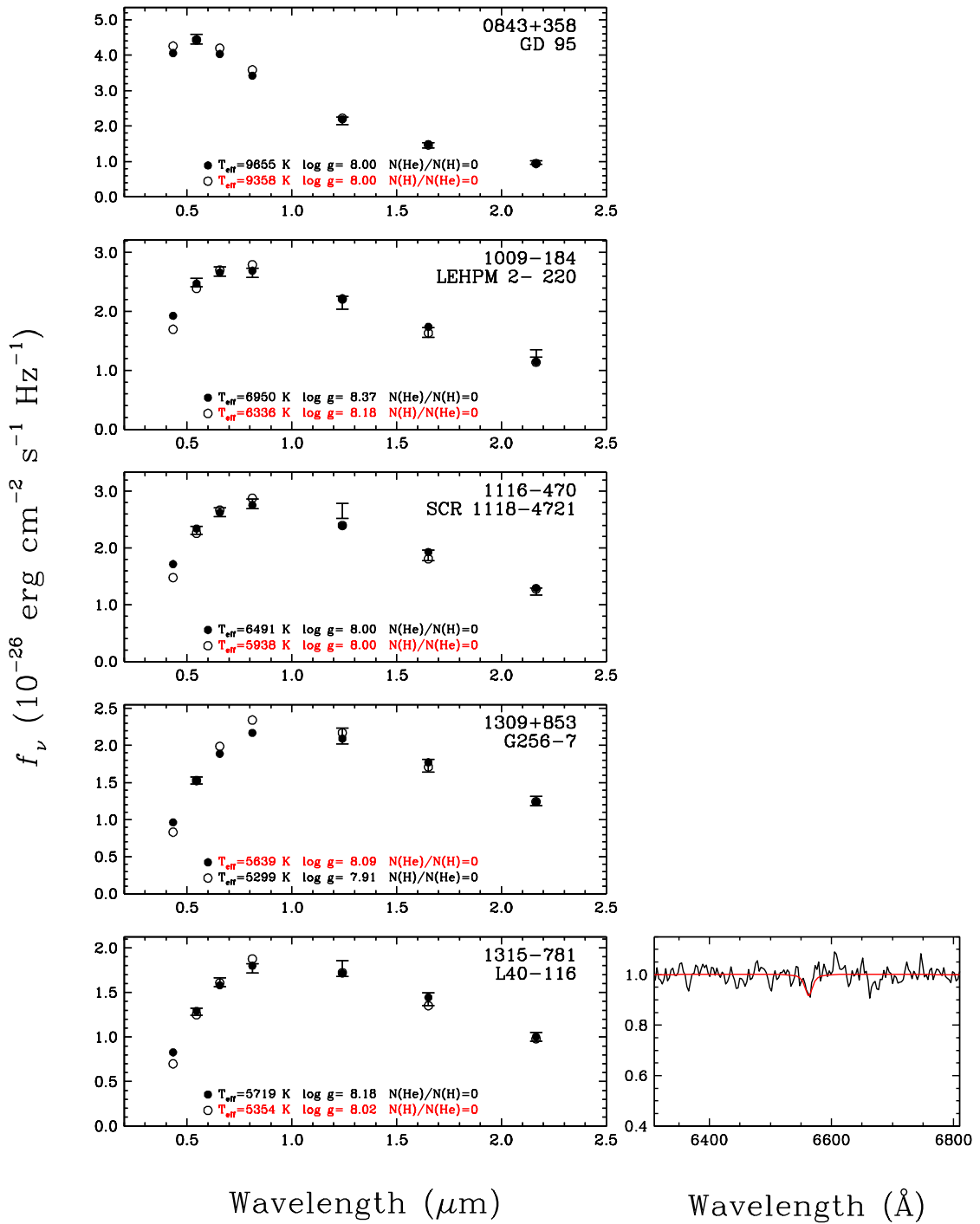


FIGURE 2.10 – (d) Fits to the energy distributions - continued.

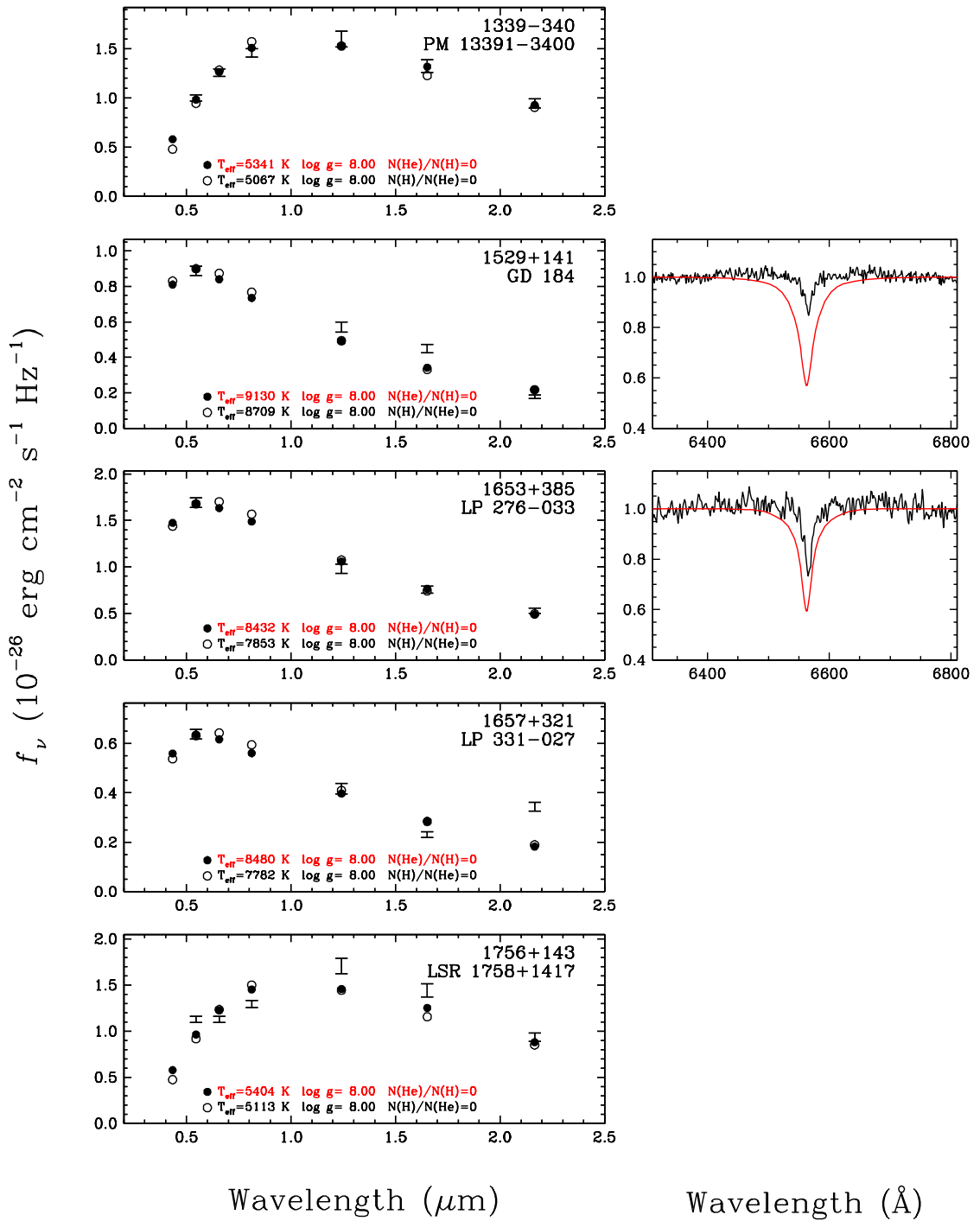


FIGURE 2.10 – (e) Fits to the energy distributions - continued.

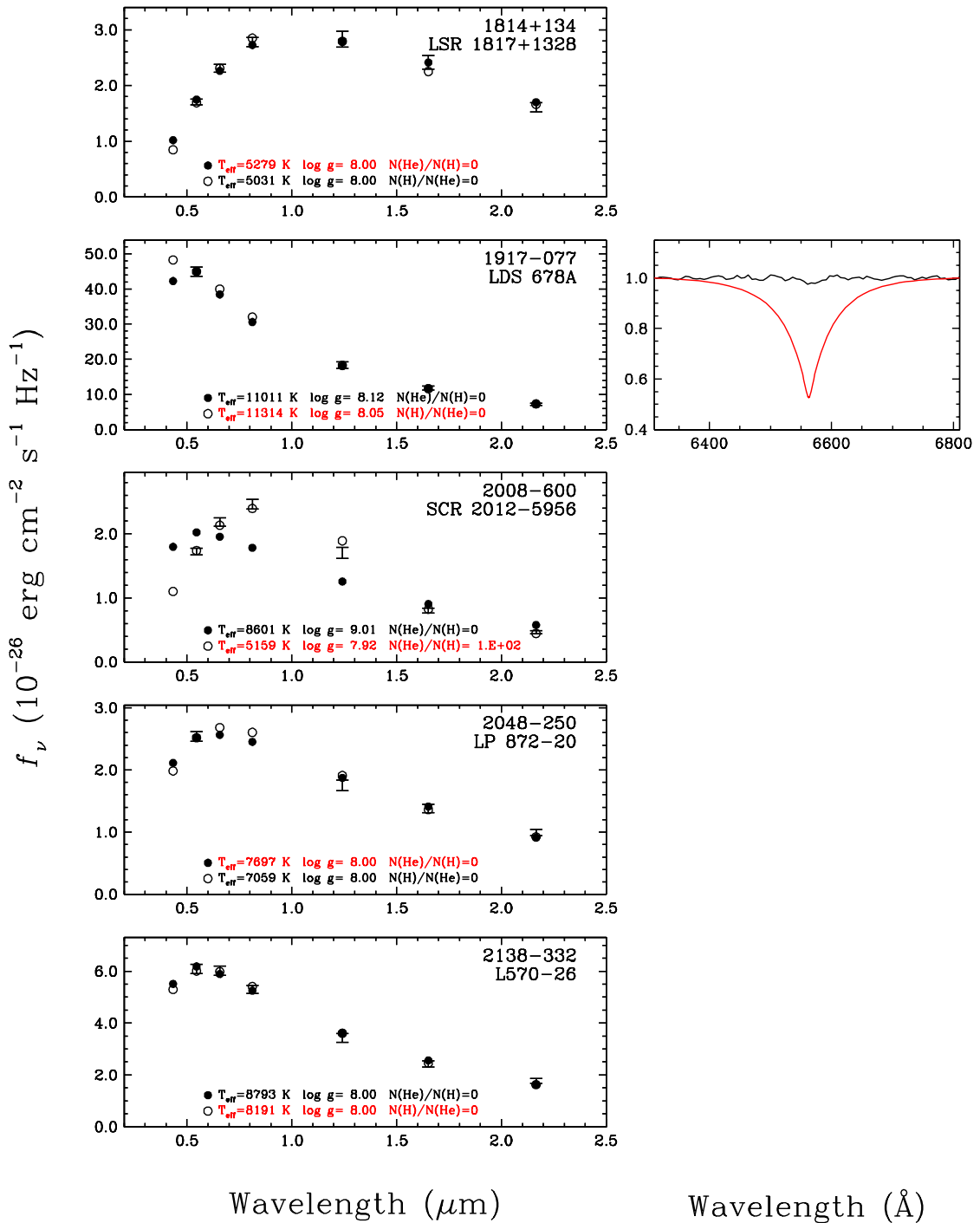


FIGURE 2.10 – (f) Fits to the energy distributions - continued.

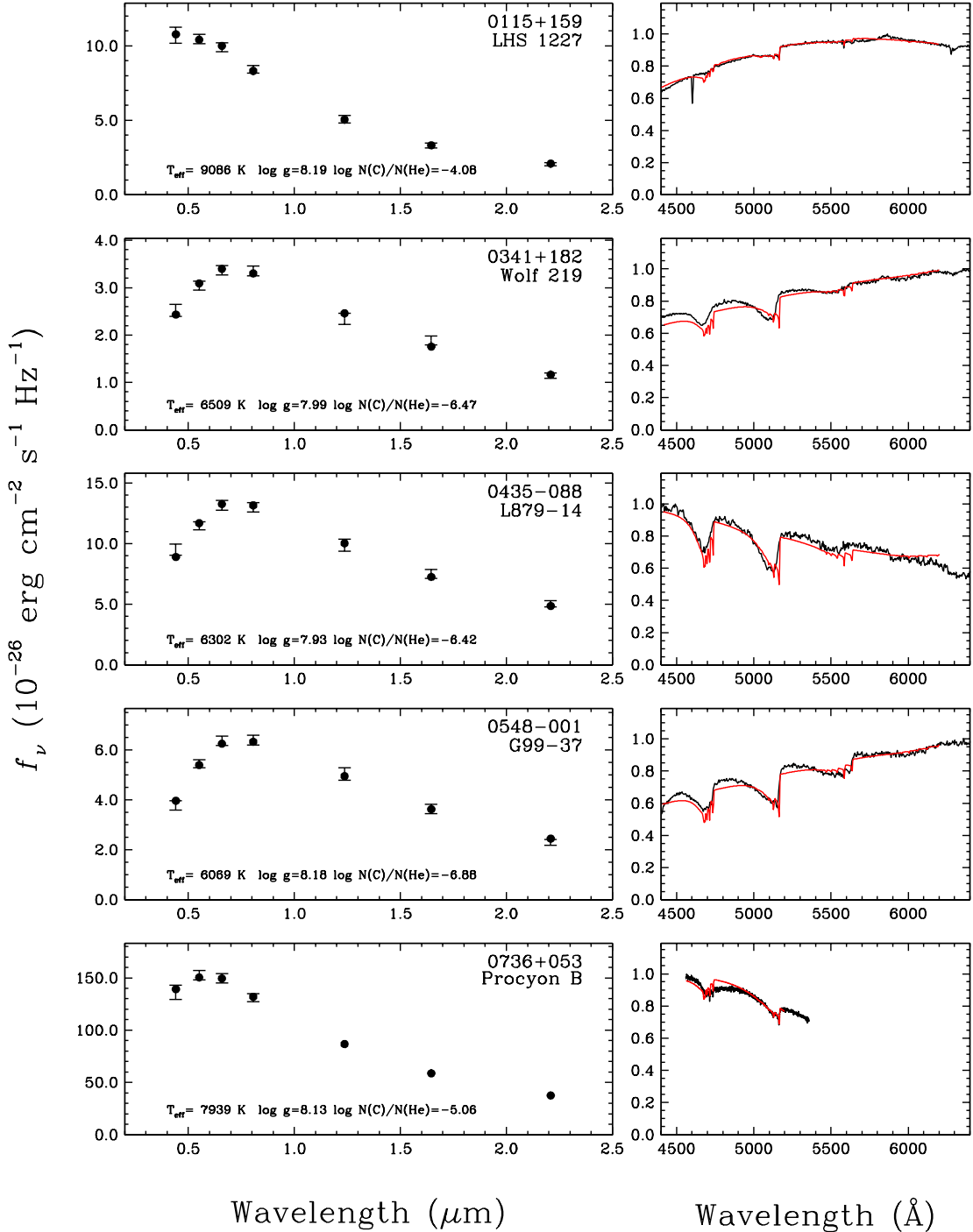


FIGURE 2.11 – (a) Fits to the energy distributions of DQ stars. Here and in the following figures, the $BVRI$ and JHK photometric observations are represented by error bars, while the filled circles correspond to our best fit with the atmospheric parameters and carbon abundances given in each panel. In the right panels are shown the observed spectra (relative flux) together with the predicted model fit (in red).

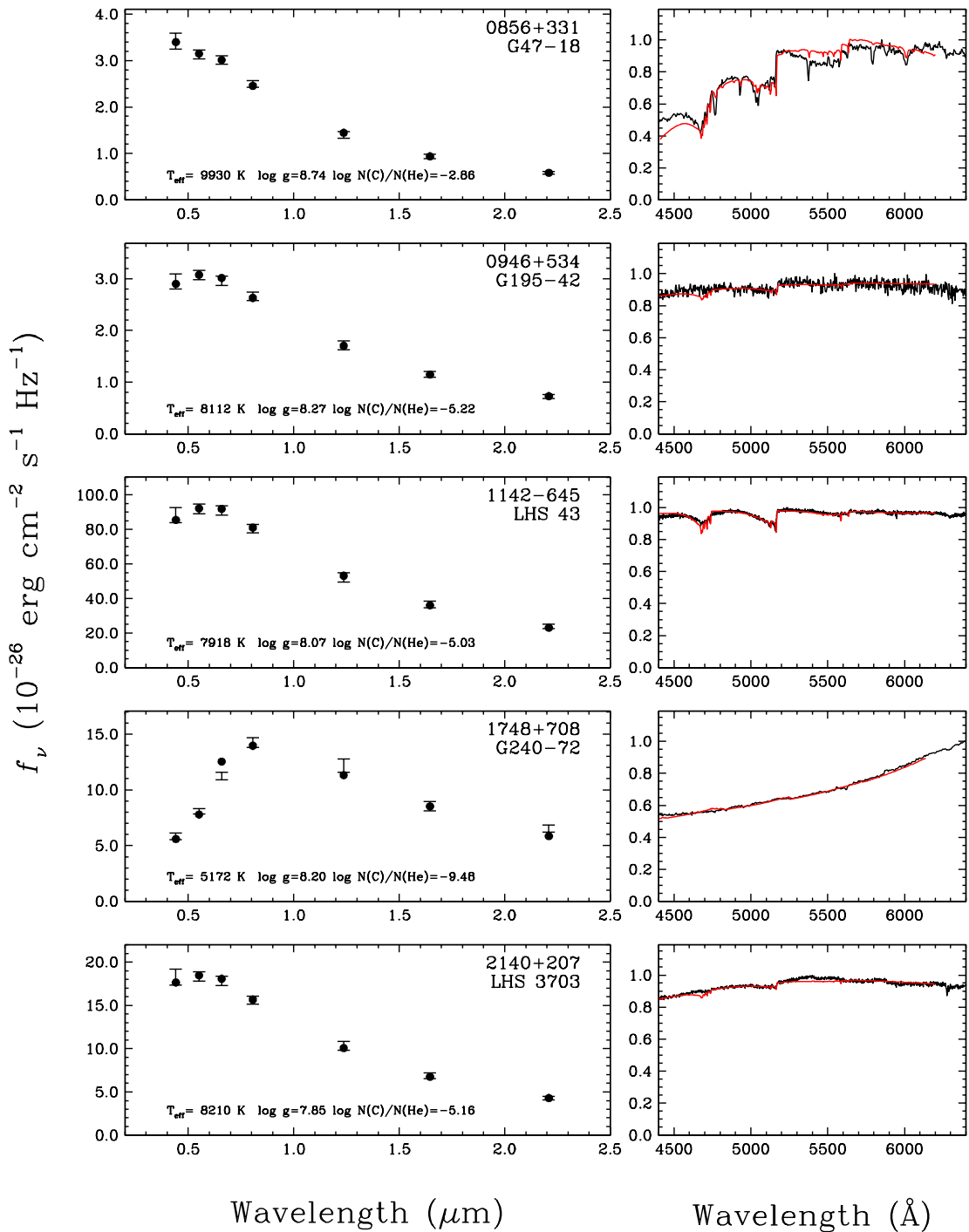


FIGURE 2.11 – (b) Fits to the energy distributions of DQ stars - continued.

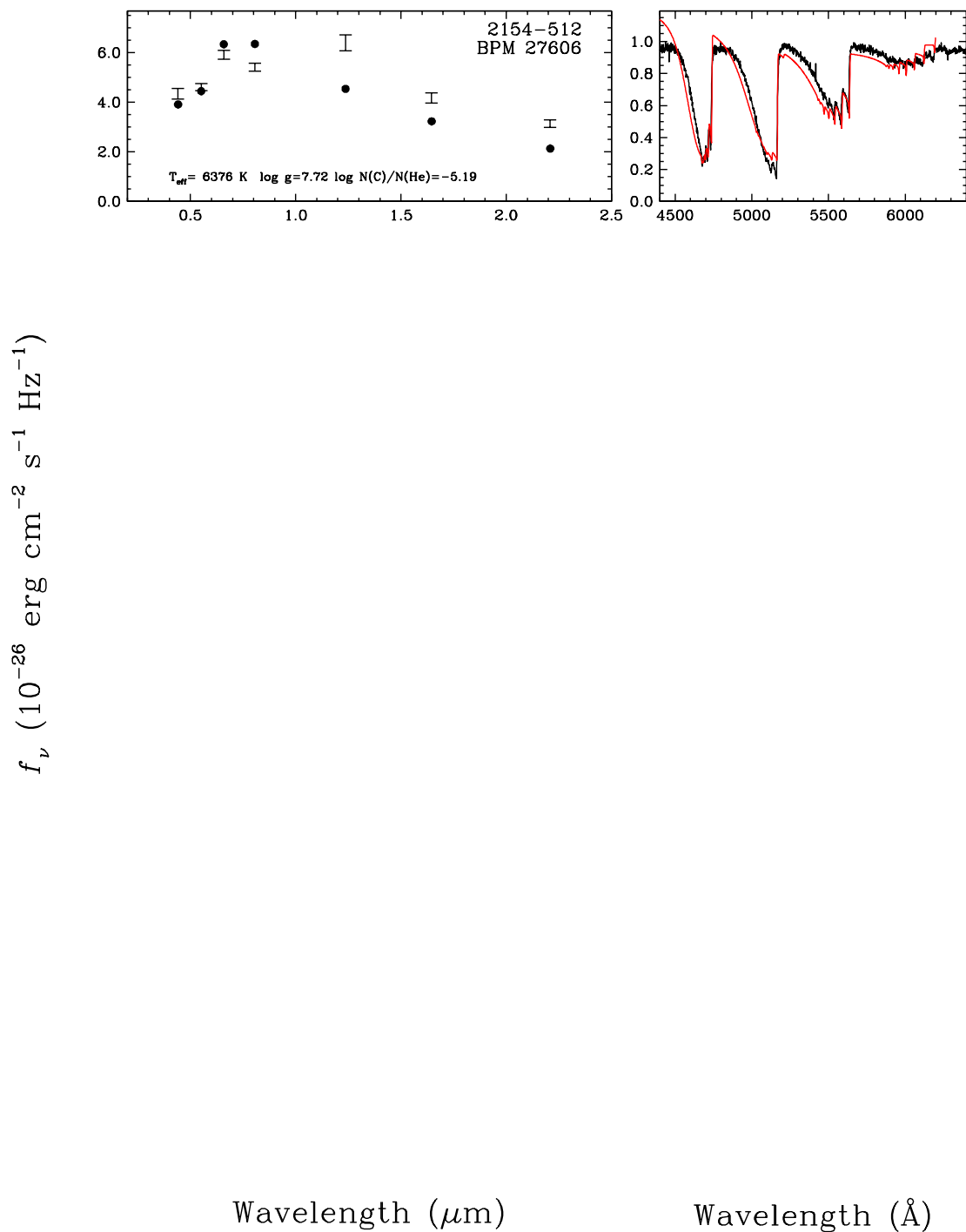


FIGURE 2.11 – (c) Fits to the energy distributions of DQ stars - continued.

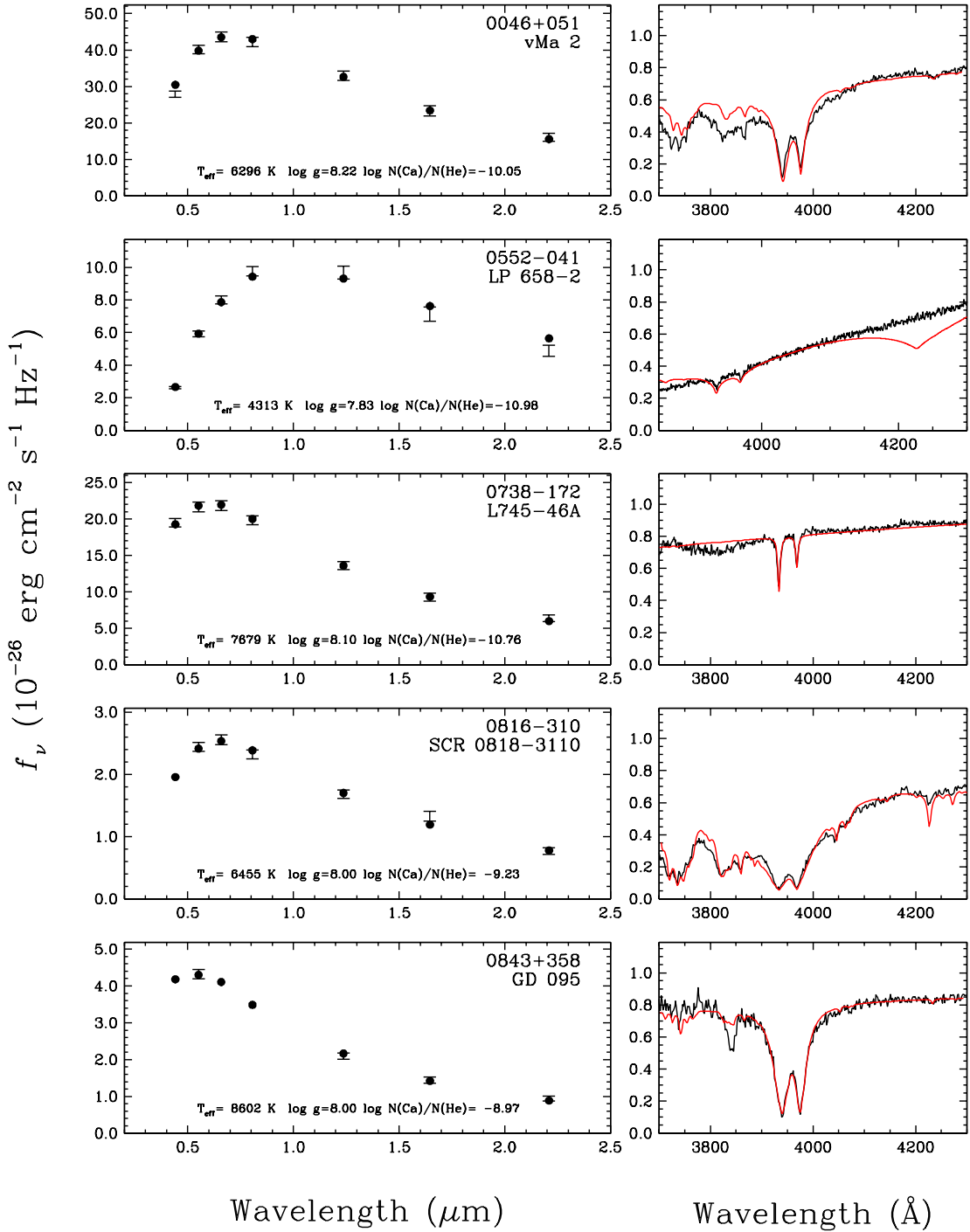


FIGURE 2.12 – (a) Fits to the energy distributions of DZ stars. Here and in the following figures, the $BVRI$ and JHK photometric observations are represented by error bars, while the filled circles correspond to our best fit with the atmospheric parameters and calcium abundances given in each panel. In the right panels are shown the observed spectra (relative flux) together with the predicted model fit (in red).

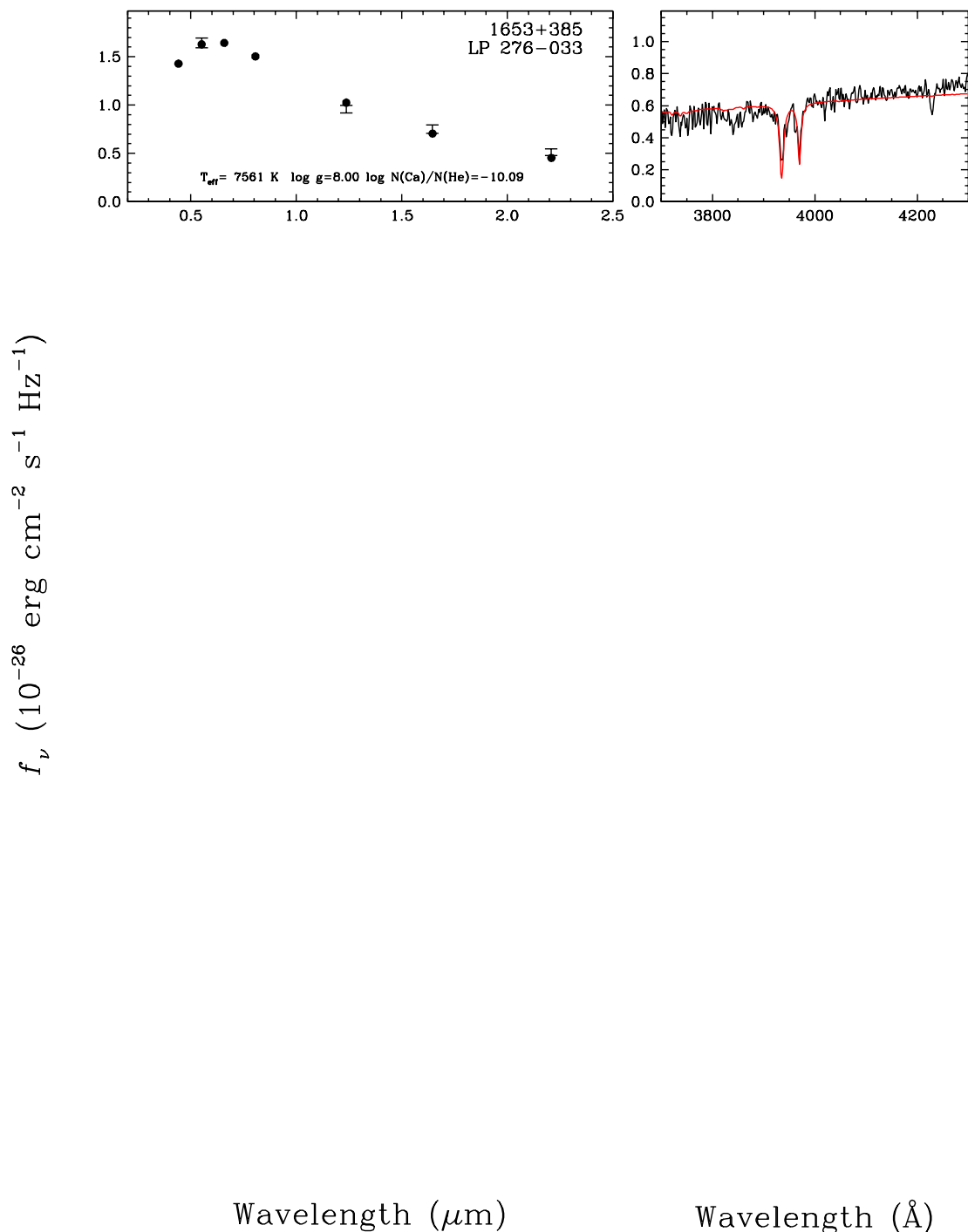


FIGURE 2.12 – (b) Fits to the energy distributions of DZ stars - continued.

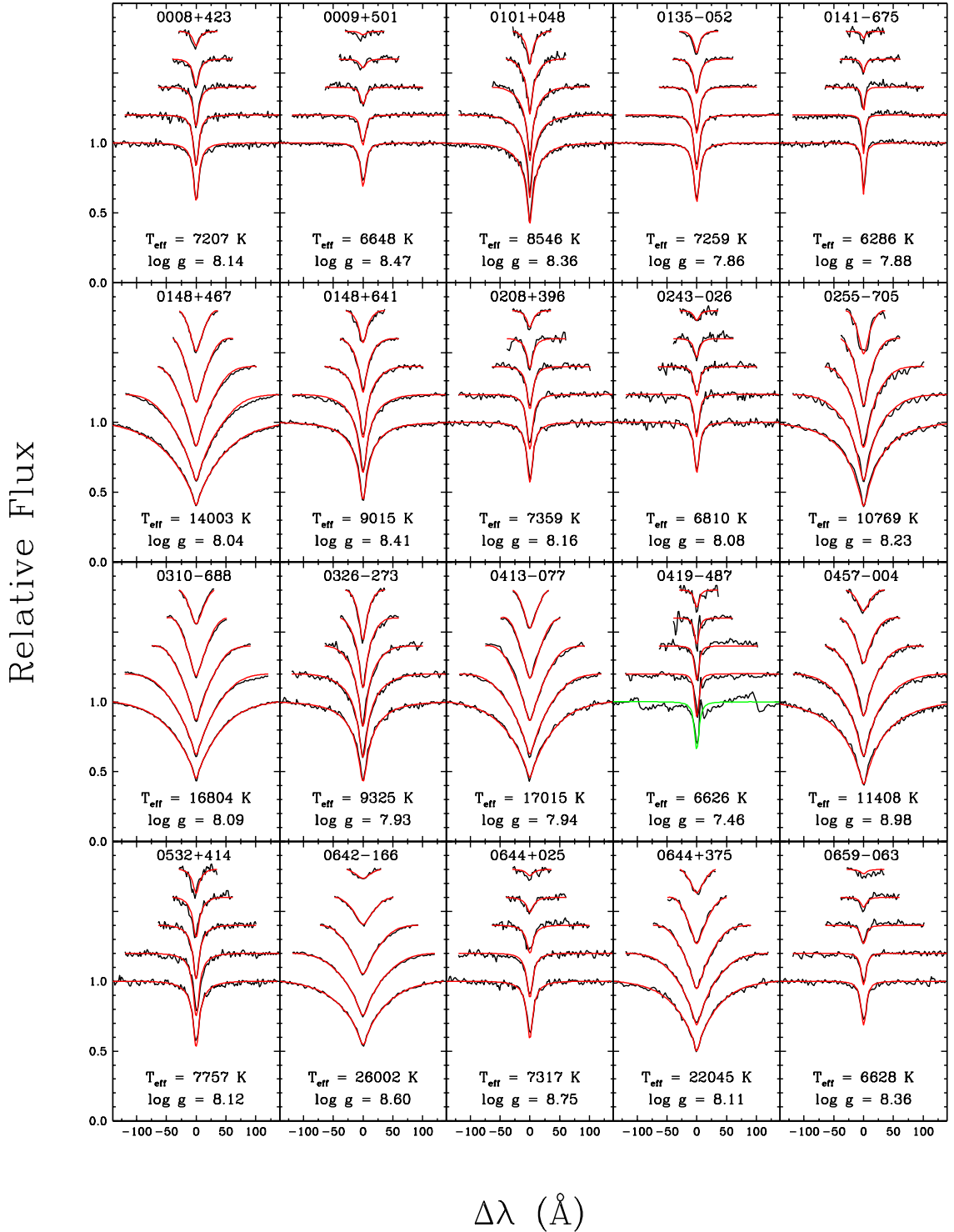


FIGURE 2.13 – (a) Fits to the optical spectra of the DA stars in the local sample. The lines range from H β (bottom) to H8 (top), each offset vertically by a factor of 0.2. Theoretical line profiles shown in green are not used in the fitting procedure.

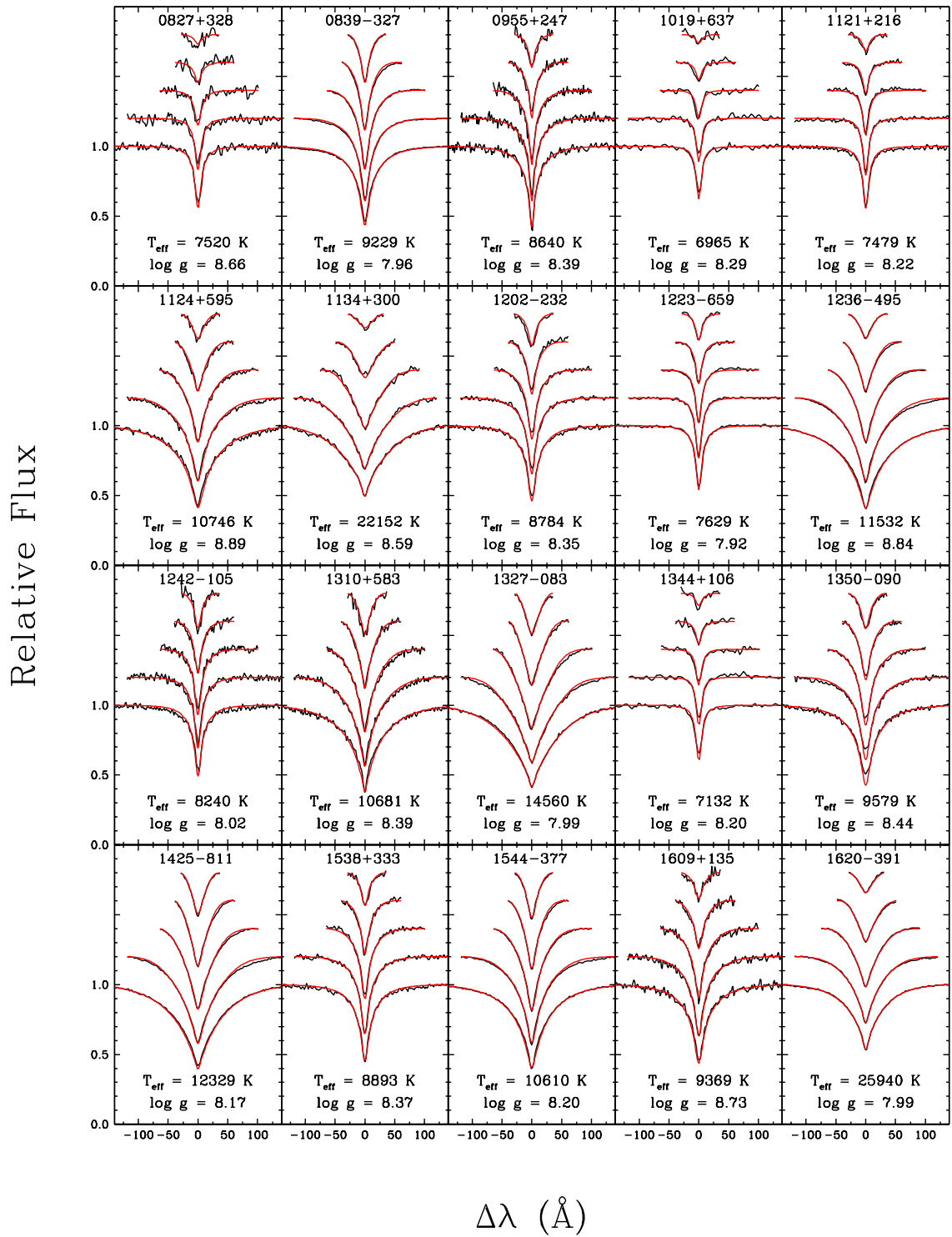


FIGURE 2.13 – (b) Fits to the optical spectra - continued.

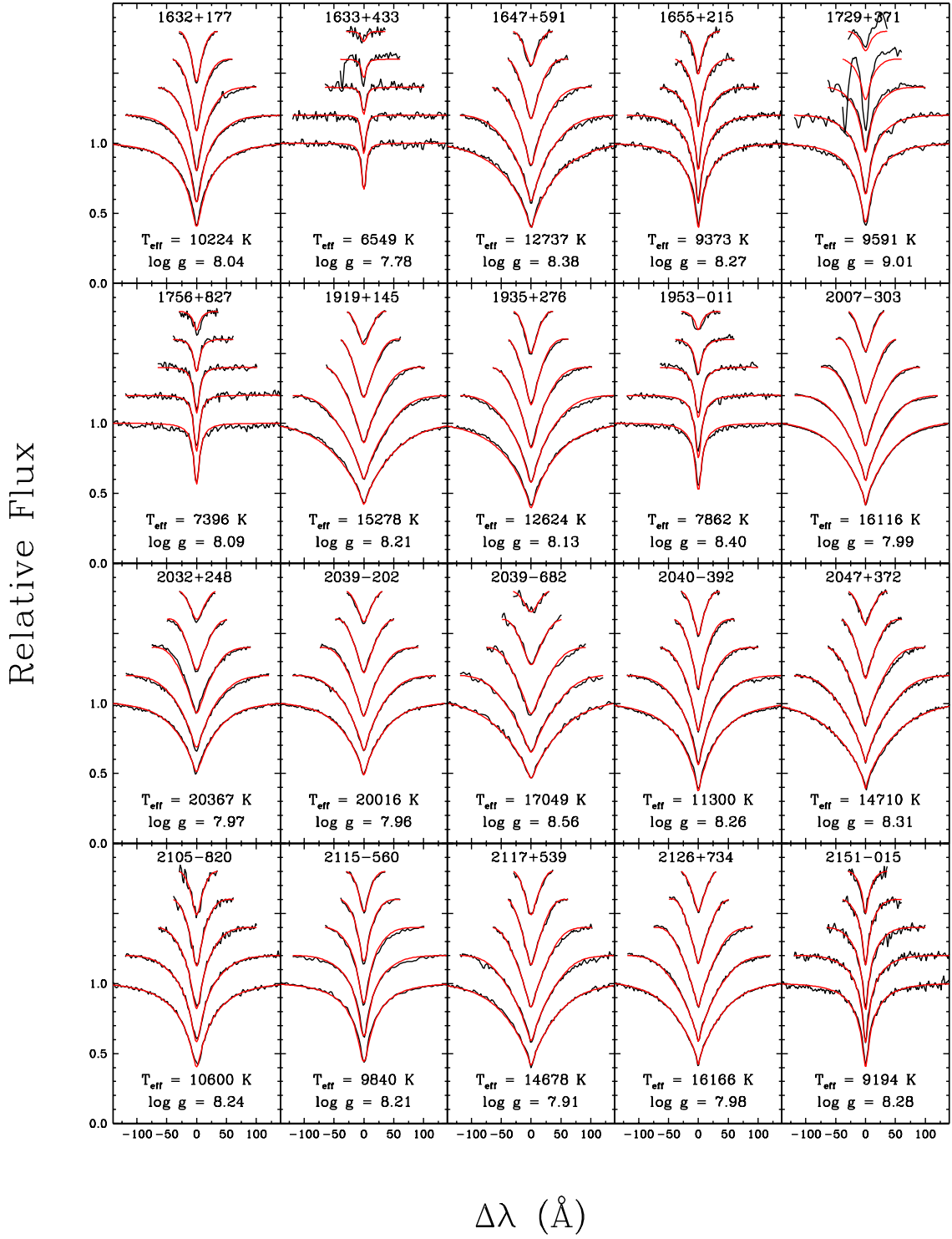


FIGURE 2.13 – (c) Fits to the optical spectra - continued.

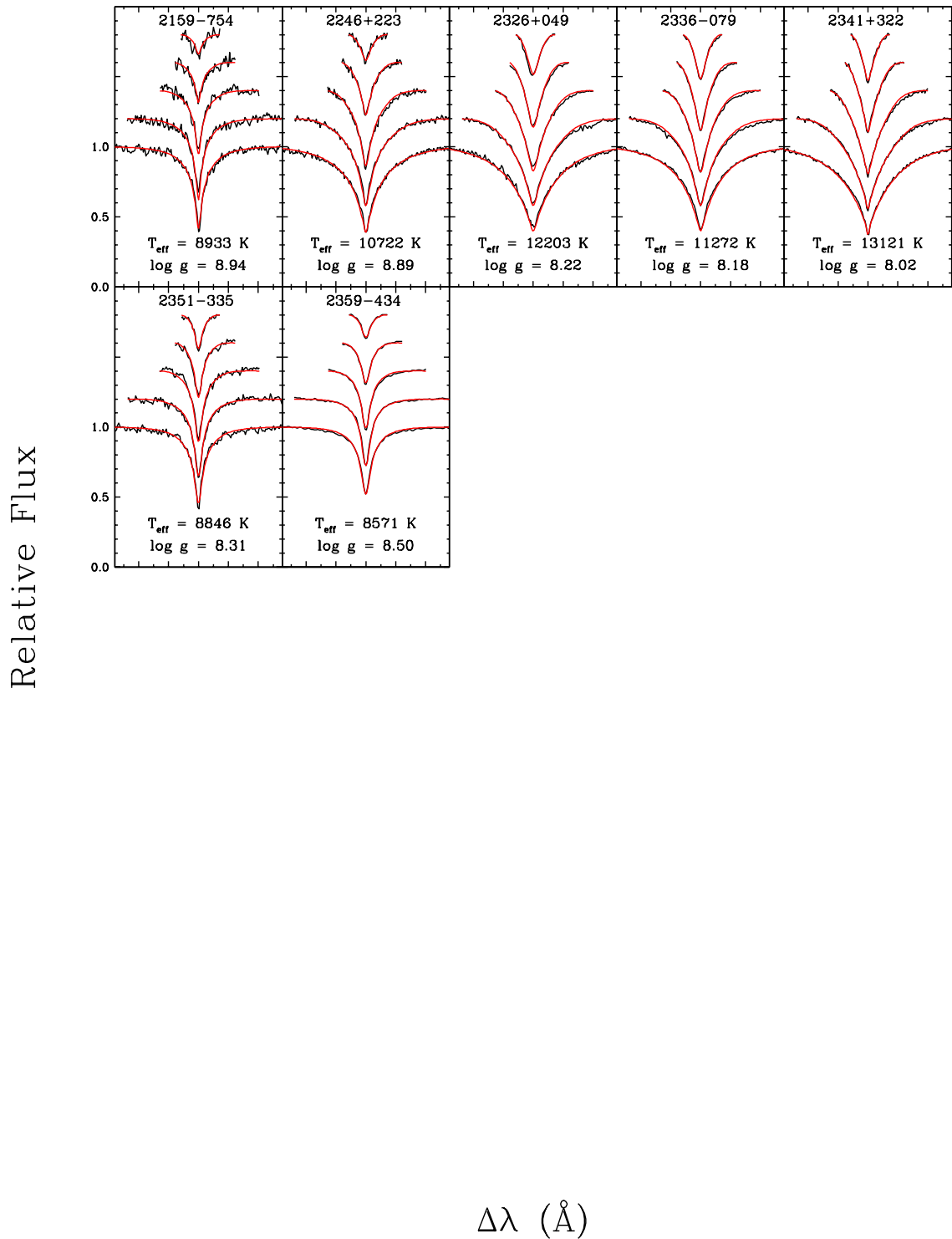


FIGURE 2.13 – (d) Fits to the optical spectra - continued.

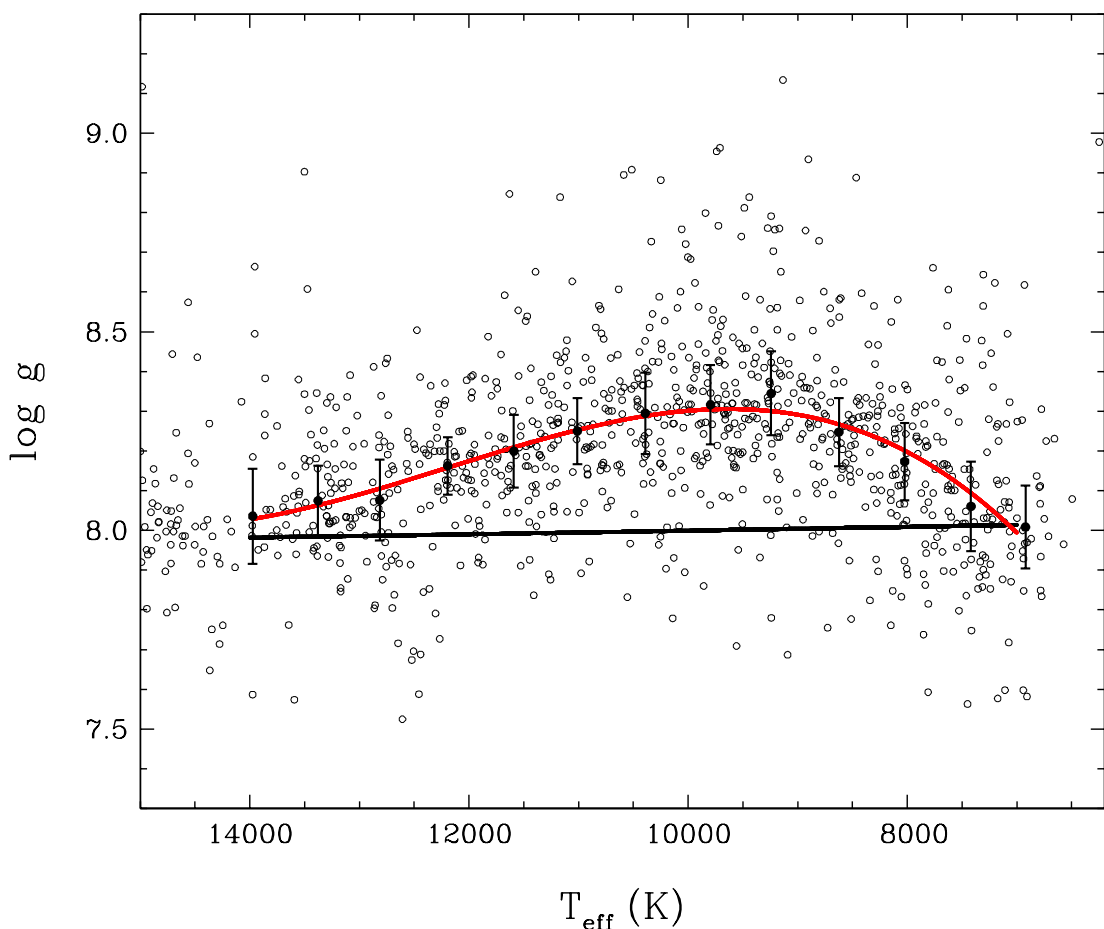


FIGURE 2.14 – Polynomial fit (red curve) through the cool ($T_{\text{eff}} < 13,000$ K) DA white dwarfs found in the SDSS (small dots) using temperature bins of 500 K (see text). The open circles and error bars represent, respectively, the median $\log g$ values and corresponding standard deviations in each bin. The black line shows the evolutionary track for a median mass of $0.61 M_{\odot}$.

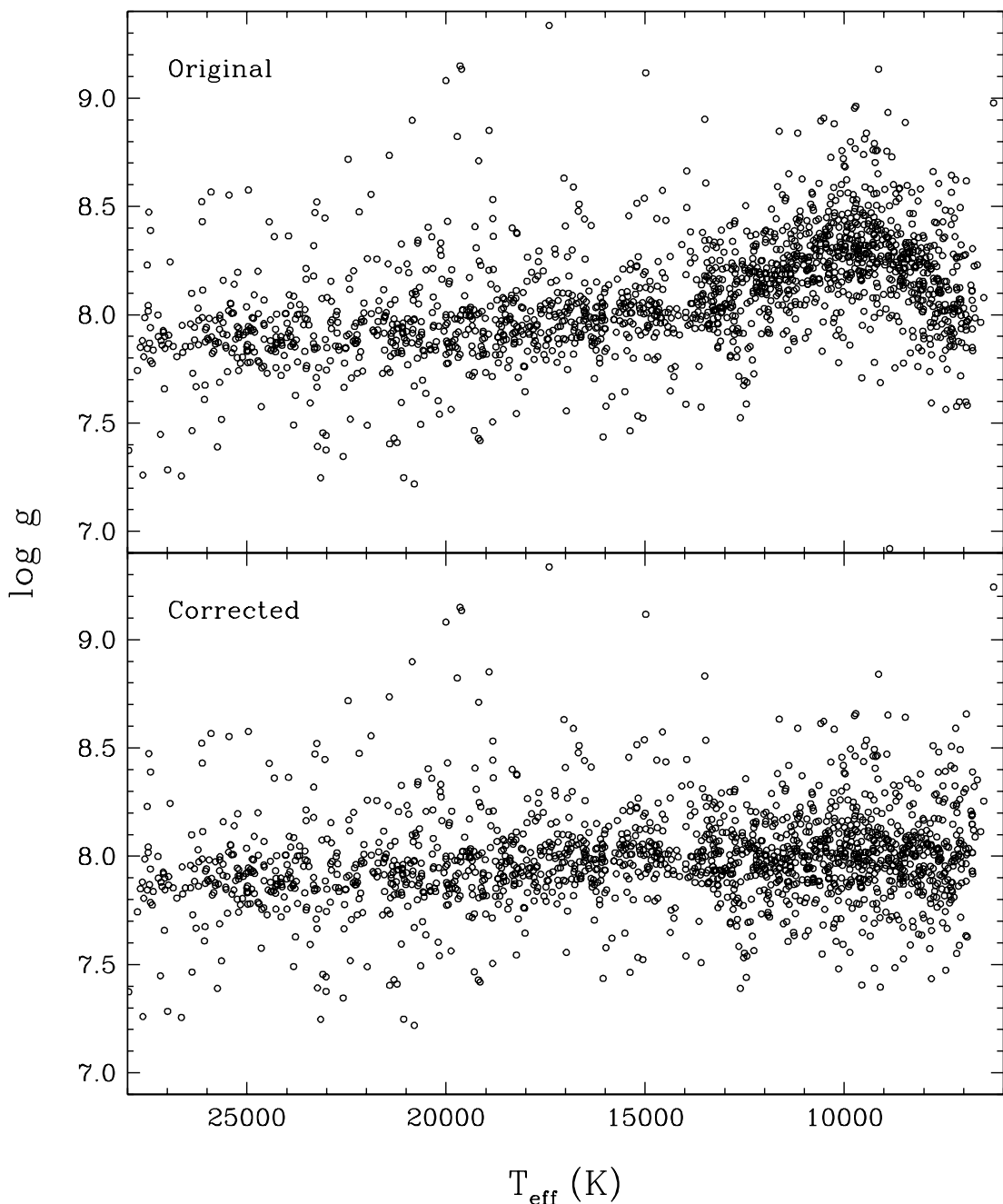


FIGURE 2.15 – Atmospheric parameters for the DA stars in the SDSS before (top panel) and after (bottom panel) the $\log g$ correction is applied.

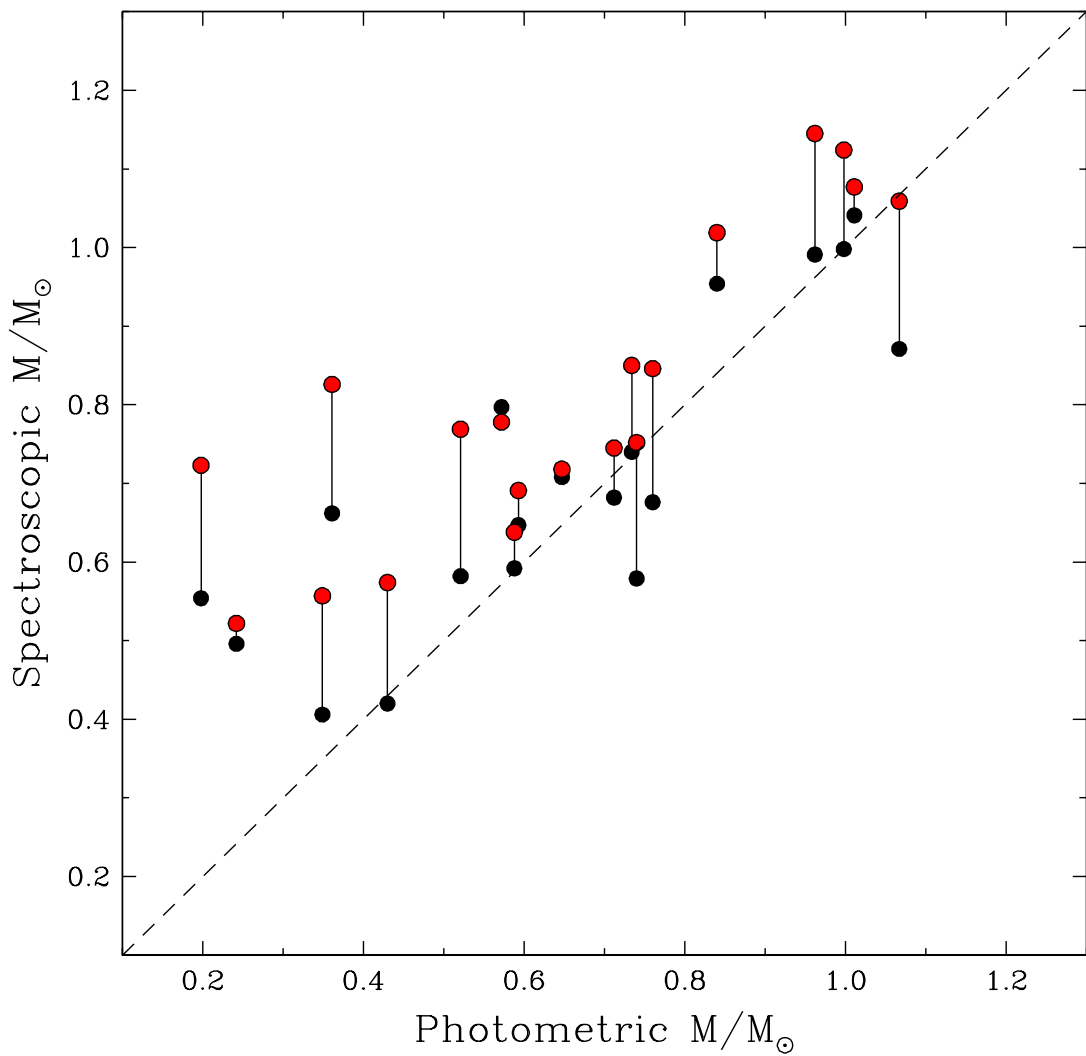


FIGURE 2.16 – Comparison of spectroscopic masses (uncorrected values in red, corrected values in black) with photometric masses for cool ($T_{\text{eff}} < 13,000$ K) DA white dwarfs.

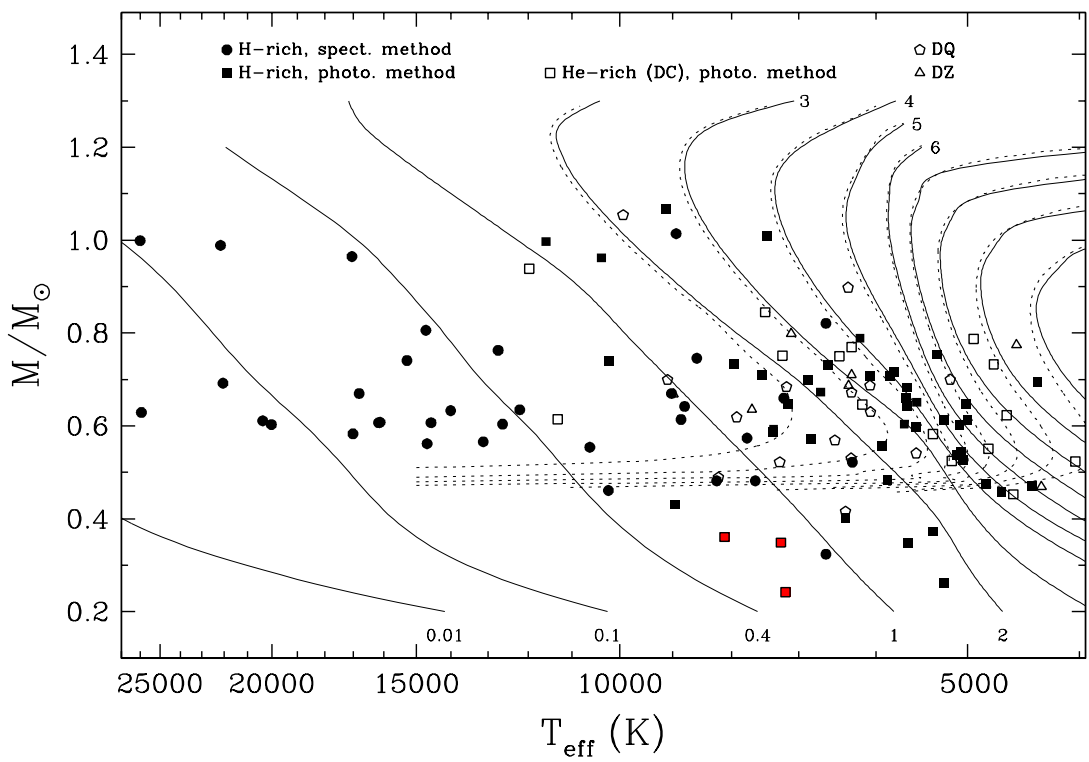


FIGURE 2.17 – Masses of all stars in the local sample ($D < 20$ pc) as a function of effective temperature. Filled and open symbols represent hydrogen- and helium-rich atmospheric compositions, respectively. Filled circles represent DA stars for which the spectroscopic method has been used. Different open symbols are used to represent DC, DQ, or DZ stars, as given in the legend. Also shown are theoretical isochrones labeled in Gyr; solid lines correspond to white dwarf cooling ages only, while the dotted lines also include the main sequence lifetime. Known unresolved double degenerate binaries are shown in red.

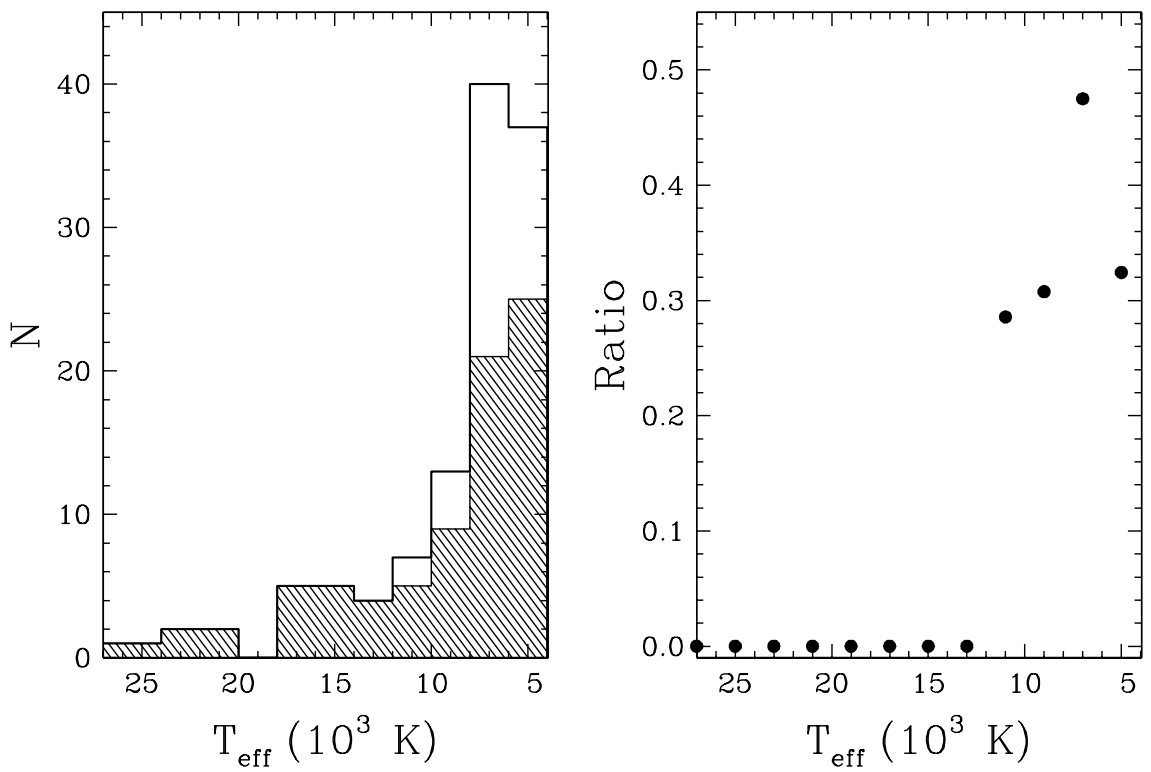


FIGURE 2.18 – Left panel: histogram of the total number of white dwarfs (solid-line) and hydrogen-atmosphere white dwarf (hatched) as a function of effective temperature. Right panel: ratio of helium-atmosphere white dwarfs to the total number of stars as a function of effective temperature.

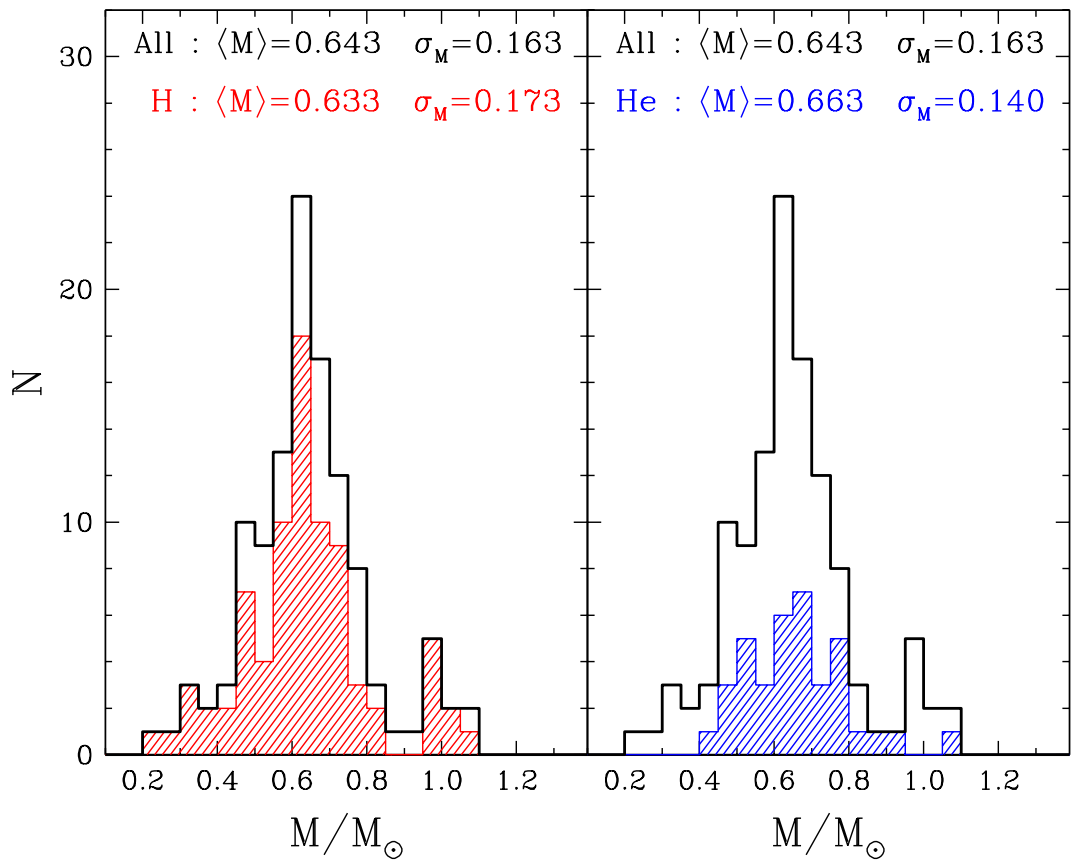


FIGURE 2.19 – Mass distribution for the 116 white dwarf stars in the local sample. The individual contributions of the hydrogen- (red) and helium-atmosphere (blue) white dwarfs are shown in the left and right panels, respectively. Mean values and standard deviations of the three distributions are indicated in the figure.

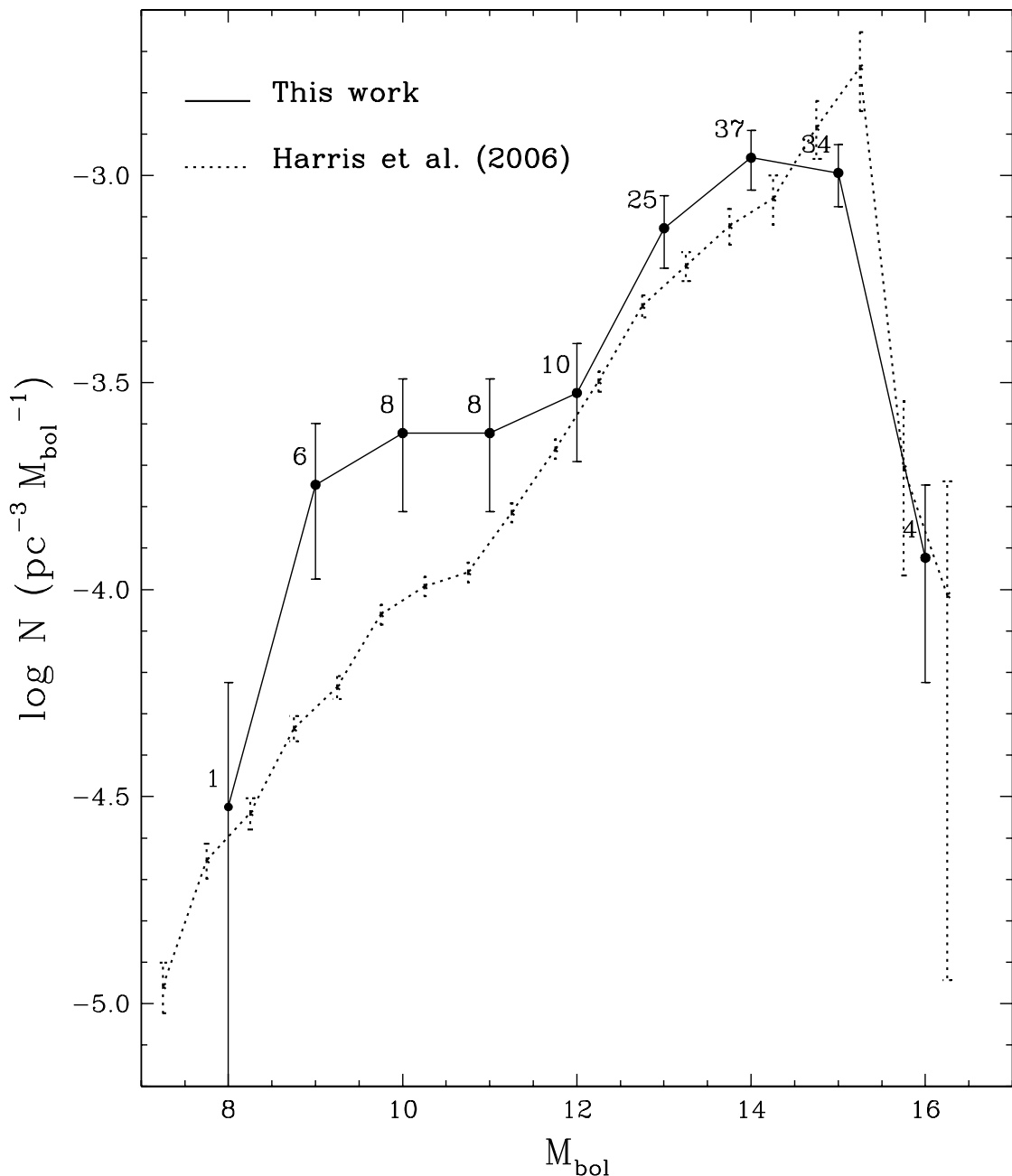


FIGURE 2.20 – Luminosity function for our complete sample of nearby white dwarfs as a function of M_{bol} (solid line), compared to the luminosity function obtained by Harris et al. (2006) for white dwarfs in the SDSS (dotted line). For the local sample, the number of stars in each magnitude bin is also given.

Chapitre 3

Conclusion

Une analyse complète de l'échantillon d'étoiles naines blanches situées à moins de 20 pc du Soleil a été présentée. Des données photométriques et/ou spectroscopiques ont été obtenues pour l'ensemble de l'échantillon initialement composé de 164 candidates. S'en est suivi une analyse homogène de tous les objets à l'aide des techniques photométriques et spectroscopiques, basées sur des modèles d'atmosphère de naines blanches et de calibrations photométriques les plus récents à notre disposition. En se basant sur les déterminations spectroscopiques et photométriques de distances, il a été possible de définir précisément l'échantillon local de naines blanches se situant à moins de 20 pc.

À partir de là, il a été possible d'étudier l'échantillon local sous tous les angles. La distribution de masse des étoiles en fonction de la température effective a permis de mettre à jour quelques points intéressants. L'absence totale de naines blanches ayant une atmosphère riche en hélium au-delà de $T_{\text{eff}} \sim 13,000$ K est révélatrice d'un ou plusieurs processus physiques qui transformeraient la composition à la surface des naines blanches lorsque ces dernières refroidissent lors de leur évolution. On a aussi pu constater que différents chemins évolutifs ont dû être invoqués afin d'expliquer la présence de naines blanches ayant des masses inférieures à $M \sim 0.48 M_{\odot}$, ainsi que la déficience d'étoiles massives en dessous de $T_{\text{eff}} \sim 7000$ K par rapport à ce que l'on peut observer à plus haute température, ou encore l'absence de naines blanches de faible masse plus chaudes que $T_{\text{eff}} \sim 7000$ K. On a par la suite exposé les distributions de masse pour la population totale ainsi que les contributions individuelles des

étoiles ayant une atmosphère riche en hydrogène et riche en hélium. La masse moyenne de l'échantillon local est de $\langle M \rangle = 0.643 M_{\odot}$, avec des valeurs correspondantes de $\langle M \rangle = 0.633 M_{\odot}$ pour les étoiles riches en hydrogène, et de $\langle M \rangle = 0.663 M_{\odot}$ pour celles riches en hélium. La comparaison entre la fonction luminosité obtenue pour le grand échantillon de naines blanches provenant du SDSS et celle dérivée à partir de notre échantillon nous a permis de valider l'hypothèse que l'échantillon local est statistiquement représentatif. En supposant un échantillon entièrement connu jusqu'à 13 pc, la détermination directe de la densité spatiale et de la densité de masse a permis d'estimer la complétion de l'échantillon local à 80 %.

L'objectif final demeure, malgré notre étude, l'obtention et l'analyse d'un plus grand échantillon *complet*, statistiquement représentatif, afin de pouvoir caractériser de façon plus précise la population des naines blanches à l'échelle de la Galaxie. Nous avons vu la principale limite de l'échantillon local à 20 pc, soit le faible nombre d'objets. À de nombreuses reprises, par exemple pour la détermination de la partie chaude de la fonction luminosité, il a été difficile, voire impossible, d'extraire de l'information pertinente. Il est donc nécessaire, après analyse complète de notre échantillon, de concentrer les efforts sur la construction d'un échantillon complet plus important. Des ajouts significatifs pour la recherche de naines blanches dans le voisinage solaire pourraient être réalisés grâce au relevé à moins de 40 pc entrepris par Limoges et al. (2010), basé sur le catalogue LSPM qui détecte les étoiles ayant un mouvement propre plus grands que $15''$ année $^{-1}$. Une analyse d'un échantillon de naines blanches plus volumineux pourrait se révéler hautement instructif, et venir alimenter les différents hypothèses proposées dans le cadre de cette étude.

Bibliographie

- Farihi, J., Becklin, E. E., & Zuckerman, B. 2005, ApJS, 161, 394
- Holberg, J. B., Oswalt, T., & Sion, E. 2002, The Astrophysical Journal, 571, 512
- Holberg, J. B., Sion, E. M., Oswalt, T., McCook, G. P., Foran, S., & Subasavage, J. P. 2008, AJ, 135, 1225
- Kawka, A. & Vennes, S. 2006, ApJ, 643, 402
- Kawka, A., Vennes, S., & Thorstensen, J. R. 2004, AJ, 127, 1702
- Liebert, J., Bergeron, P., & Holberg, J. B. 2005, The Astrophysical Journal Supplement Series, 156, 47
- Limoges, M. & Bergeron, P. 2010, The Astrophysical Journal, 714, 1037
- Limoges, M., Bergeron, P., & Lépine, S. 2010, in American Institute of Physics Conference Series, Vol. 1273, American Institute of Physics Conference Series, ed. K. Werner & T. Rauch, 193–196
- Salim, S. & Gould, A. 2003, The Astrophysical Journal, 582, 1011
- Sion, E. M., Holberg, J. B., Oswalt, T. D., McCook, G. P., & Wasatonic, R. 2009, AJ, 138, 1681
- Subasavage, J. P., Henry, T. J., Bergeron, P., Dufour, P., & Hambly, N. C. 2008, AJ, 136, 899
- Subasavage, J. P., Henry, T. J., Bergeron, P., Dufour, P., Hambly, N. C., & Beaulieu, T. D. 2007, AJ, 134, 252

Vennes, S. & Kawka, A. 2003, ApJ, 586, L95